



Application of Micro-Rotors to Induce Crystal Nucleation: Challenges, Takeaways, and Future Prospects

PhD Thesis

D. Maciver
Chemical and Process Engineering Department
University of Strathclyde, Glasgow

November 5, 2024

This thesis is the result of the author's original research. It has been composed by the author and has not been previously submitted for examination which has led to the award of a degree.

The copyright of this thesis belongs to the author under the terms of the United Kingdom Copyright Acts as qualified by University of Strathclyde Regulation 3.50. Due acknowledgement must always be made of the use of any material contained in, or derived from, this thesis.

Abstract

Contents

Abstract	ii
List of Figures	vi
List of Tables	xvi
Preface/Acknowledgements	xviii
1 Introduction	2
1.1 Nucleation	3
1.1.1 Primary & Secondary nucleation	3
1.2 Nucleation Theories	5
1.2.1 Classical Nucleation Theory (CNT)	5
1.2.2 Two Step Nucleation	7
1.2.3 Non-classical Nucleation	8
1.3 Crystallisation methods	8
1.3.1 Cooling Crystallisation	8
1.3.2 Evaporative Crystallisation	9
1.3.3 Anti-solvent Crystallisation	10
1.4 Optical Tweezers	10
1.4.1 Background	10
1.4.2 Literature related to laser induced nucleation	11
1.4.3 Optical Torque and rotation	14
1.5 Shear induced Nucleation	17

Contents

1.6	Significance of Thesis	18
1.7	Overview	19
2	Theory and methods	20
2.1	Electromagnetism and optical tweezing	20
2.2	Lornez-Mie Theory	23
2.2.1	Ray-Optics Regime	25
2.2.2	Rayleigh Scattering	26
2.3	Scattering methods	27
2.3.1	T-matrix Method	27
2.3.2	Discrete Dipole Approximation	28
2.4	Langevin Equation	29
2.4.1	Finite Difference	32
2.5	Calibration Techniques	34
2.5.1	Potential Well Analysis	34
2.5.2	Equipartition method	35
2.5.3	Mean Square Displacement	36
2.5.4	Power Spectrum Density (PSD)	38
2.6	Simulation of spherical aggregates	41
2.6.1	Simulation reference frame	44
2.7	Simulated Quadrant Photodiode	45
3	Effects of localised shearing on crystal growth and nucleation	49
3.1	Optical Tweezer Equipment	50
3.1.1	Position detection methods	51
3.1.2	Fourier Optics and 4f correlators	54
3.2	Synthesis of Birefringent Micro spheres	55
3.2.1	Liquid Crystal Rotors	57
3.3	Rotation of birefringent micro spheres	58
3.3.1	Estimation of fluid flow around a rotating particle in bulk fluid .	60
3.4	Rotating spheres in Supersaturated solution	63

Contents

3.5	Nucleation with a Stationary and Moving Beam	67
3.5.1	Stationary beam	68
3.5.2	Moving Beam	70
3.5.3	Direct trapping of Glycine clusters	73
3.5.4	Influence of a moving beam front on seed crystals	74
3.6	Summary of Moving Beam Phenomena	75
3.7	Conclusion	76
4	Complex Langevin dynamics of spherical dimers	80
4.0.1	Simulation Parameters	81
4.1	Positional and Orientational dependence of Trapping forces	82
4.1.1	Non-trivial equilibrium configurations	88
4.2	Continuous rotational motion due to second-order scattering	89
4.2.1	Polarisation Dependency on Dimer trajectory	90
4.2.2	Comparison of optical torques for Sphere and Dimers	92
4.2.3	Rotational frequency as a function of size ratio and orientation .	93
4.2.4	Gyroscopic Precession using asymmetric dimers	96
4.3	Characterisation of asymmetric dimers via PSD analysis	98
4.4	Conclusions	101
5	Detection and Characterisation of rotational spherical aggregate rotational dynamics	102
5.1	Monitoring Stochastic rotational motion using static light scattering . .	104
5.1.1	Coordinate System	104
5.1.2	Dimer	104
5.1.3	Scattering and Detection	104
5.2	Interpretation of scattering data into orientation estimates	107
5.2.1	Calculation of error	112
5.2.2	Brownian Simulation	113
5.2.3	Testing the Neural Network	114
5.2.4	Accounting for sources of error in light scattering measurements	116

Contents

5.3	QPD Simulations	121
5.3.1	Incident beam	121
5.3.2	Scattered and Total Fields	123
5.4	Rotations and Asymmetric particles	126
5.5	Power Spectra of single sphere vs spherical aggregates	127
5.6	Conclusion	128
6	Closing Remarks	130
A	Appendix	131
A.1	Estimation of fluid shear rates via galvano mirror	131
A.2	Approximation of Area growth rate	133
	Bibliography	134

List of Figures

1.1	Secondary Nucleation mechanisms, classified by Agrawal and Paterson [9]	4
1.2	Free energy diagram of a newly formed nucleus according to the Classical Nucleation Theory. The total free energy (blue) is due to the competition between the volume free energy gain (green) and the interfacial free energy cost (orange). Dotted lines are for a higher supersaturation than the solid lines, the interfacial energy cost is independent of supersaturation.	6
1.3	Typical Concentration vs Temperature plot with the solubility curve (black) and metastable zone (red). 3 different cooling curves are shown as well: a high rate of cooling (orange) shows the mixture quickly dropping below the solubility curve resulting in no new nuclei forming. A low rate of cooling (green) shows the mixture exceeding the metastable zone, where now nucleation occurs spontaneously and cannot be controlled without further cooling. A typical cooling rate (blue) shows how a typical cooling crystalliser will operate, sitting in the middle of the other two curves.	9
2.1	Example of a sphere's ($r = 1 \mu m$) force-displacement curve while moving along the x-axis, where $x = 0$ is the centre of the beam. The harmonic regime is highlighted by the black linear fit.	22

List of Figures

2.2	Example trajectory created using Finite Differences method for a $2\mu m$ diameter sphere. Trap stiffness's were estimated using ott at $\kappa_x = \kappa_y = -100 \text{ pN}/\mu m$ and $\kappa_z = -25 \text{ pN}/\mu m$. The particle's motion can be localised around the shaded ellipsoid.	33
2.3	Example mean squared displacement using (2.45), for a $1\mu m$ sphere trapped by an optical potential well. The dotted line represents the upper limit of the sphere's displacement due to the optical trap.	37
2.4	Example PSD fitted using (2.48), power spectra is collected from an optically trapped silica sphere suspended in water. The difference in magnitude is due to the asymmetry of the quadrant photo diode having a stronger signal response in the direction of the polarisation vector. Using a conversion factor (see (2.50)) will adjust the power spectra to better describe the trap shape.	40
2.5	Ray scattering render of both the laboratory frame and particle frame for a dimer and a Gaussian beam. The origin of the laboratory frame is defined as the focus of the trapping beam, with the positive z -axis being aligned with the direction of beam propagation. The particle frame is centred on the dimer's centre of mass with the primary axis U_z being aligned with the centres of the two spheres. Black line is scaled to represent $1 \mu m$	44

List of Figures

2.6 Total Field incident on the quadrant photo diode for a several different displacements. Top Left: $2\mu m$ diameter silica sphere placed at the focus of a beam. Top Right: silica sphere is now displaced by $1\mu m$ along the x-axis. Bottom Right: silica sphere is now displaced along the y-axis. Bottom Left: silica sphere is now displaced by $0.707\mu m$ along the x and y axis. The trapping beam is a TEM_{00} Gaussian, polarised along the along the x-axis. S_x , S_y , and S_z are shown to the right of each graph, Q_1 , Q_2 , Q_3 , and Q_4 are shown above each graph.	47
2.7 Comparison between QPD response signal versus work conducted by Rohrbach, single sphere ($r = 150 nm$, $n = 1.57$) is scanned by a $1064 nm$ laser and the QPD signal recorded. Solid lines represent the signal produced by QPD using <i>ott</i> and points represent the signal response collected from [100].	48
3.1 Optical tweezer set up used for the majority of the PhD. The focal lengths of f_1 , f_2 , f_3 , & f_4 are $-20 mm$, $60 mm$, $150 mm$, & $200 mm$ respectively [M = mirrors, DM = dichroic mirrors, f = focal lenses]. Diagram not drawn to scale.	52
3.2 Comparison between QPD and Lateral effect photodiodes. The four quadrants of a QPD (left) experience different photocurrents based on the total intensity of light incident on each section (labelled A, B, C, D). Whereas a Lateral effect sensor (right) uses the resistive properties of the photodiode surface to vary the create different photocurrents passing through the anodes A, B, C, and D.	53
3.3 Signal generator galvano mirror controller, channel 1 controls the x-axis mirror, while channel 2 controls the y-axis mirror. Both channels can be manipulated independently.	54
3.4 (a) Sample Vaterite sphere suspended in water and trapped by circular polarised trap. (b) Collected power spectrum from rotating Vaterite, peaks in the power spectrum appear at integer multiples of the rotational frequency ($f_{rot} \approx 49.8 Hz$)	56

List of Figures

3.5	Liquid crystal undergoing rotation due to the circularly polarised trap.	58
3.6	Example of QPD signal being converted from the time domain to the frequency domain. (left) Raw signal collected from the QPD over the 1st second of its trajectory showing a periodic spacing with a period of $1/f_{rot}$. (right) Power spectrum of the QPD signal, the y-axis is a linear scale to demonstrate the clear peaks in the power spectra. The rotational frequency is the first instance of a peak forming, and after that the peaks appear in integer multiples of f_{rot}	61
3.7	(Top) Fluid flow radiating out from the surface of a rotating Vaterite sphere. (Bottom) Shear rates computed using Eq.3.4, optimal shear rate is of $3000s^{-1}$ is indicated by the dotted line. Vaterite radii and rotation frequencies are shown, the laser power was kept constant at 450 mW. Reported rotation rates, and their corresponding fluid flow and shear rates, for Vaterite are also plotted alongside lab results. Results from [57], [58] are included as well.	62
3.8	Diagram demonstrating how fluid shear rate varies radially from a rotating sphere (rotation rate = f_{rot}). (a) the shear rate exceeds the optimal shear rate ($\dot{\gamma}_{opt}$) and suppresses the nucleation rate. (b) shear rate is close to the optimal amount, enhancing the nucleation rate. (c) shear rate is far below the optimal amount and the nucleation rate is comparable to the bulk fluid.	64
3.9	Diagram of optical trapping set up for rotating birefringent particles in a supersaturated solution. Left: side view of the trapping set up showing the location of the trap focus at the edge of the droplet of a supersaturated solution. The approximate contact angle (calculated by [111]) is used to provide a scale of how close a trapped particle could be located. Right: top down view of the glycine droplet with a trapped birefringent particle shown close to edge of the trap. As the particle rotates the drag force from the surrounding fluid generates a flow field around itself (see Eq. 3.3).	65

List of Figures

3.10 Laser induced nucleation at the edge of a droplet of supersaturated glycine solution. (b) shows the first instance of a crystal nucleus, growing quickly through (c)-(e) until after 6.665 s the crystal begins to escape the trap.	69
3.11 Frames from a longer video depicting the growth of a nucleus using a moving beam. Beam power is kept at 700 mW and the supersaturation was estimated at $S=0.86$. Initially the crystal shape is amorphous (a) but eventually reaches a more regular shape (b). This crystal is still influenced by the optical trap as even when not directly irradiated by the laser the crystal rotates between (c) and (d). When the laser is focused on a corner the crystal growth is localised to that region, resulting in an elongated section forming between frames (e) and (f).	71
3.12 Interesting crystal growth on the surface of an existing crystal. Initially the crystal surface seems flat (a) but eventually a different crystal structure grows out off of the surface (b).	72
3.13 Frames from a longer video demonstrating the trapping of a glycine droplet. Solution is undersaturated glycine and water ($S = 0.86$), with the laser power set at 750 mW. (a) shows a trapped droplet (outlined in black) being brought into contact with a larger droplet. (b) upon contact a nucleus can be seen between the two droplets. The growth is rather slow with the crystal having no clear defined morphology through (c) and (d). Between frames (e) and (f) the larger droplet finally joins the main crystal.	78
3.14 Frames from a seed crystal being irradiated by a scanning laser. The laser path is shown below in red. Initially the crystal edge is nearly perpendicular to the laser path. Over the course of nearly twenty minutes the crystal around the laser has dissolved leaving a concave indent.	79

List of Figures

3.15 Diagram outlining how a moving beam assists in the growth of a crystal nucleus. (a) a crystal nucleus is partially trapped by a moving beam with solute droplets close to its surface. (b) droplets close to the laser focus can be drawn in by gradient forces and moved towards the crystal surface. (c) the laser brings in material that is then deposited on the surface of the crystal. (d) eventually the crystal area either fully surrounds the laser focus or the solution surrounding the laser is depleted of solute material.	79
4.1 Plots of force vs displacement of the centre of mass of the dimer (μm) for the case of a dimer of size ratio 2. (a) is the case where the dimer is in its' 'standard' orientation, where the dimer is trapped at $z = 1.71 \mu\text{m}$. (b) is the case where the dimer is in its' 'inverted' orientation, the dimer is trapped at two positions: $z = 1.20 \mu\text{m}$ & $z = -1.63 \mu\text{m}$. On the left are renders to visualise the dimer orientation are shown below each plot. The black lines on each force-curve is a linear fit with the slope being reported as the trap stiffness in the legend.	84
4.2 Plots of force vs displacement of the dimer's centre of mass spheres, where a positive force indicates the dimer is directed right on the x-axis, and vice versa for a negative force. The same simulation parameters are used here as in fig 4.1(a) and (c). The blue curve representing the force response for a dimer in its standard orientation, orange being the inverted case, and green the same case but placed below the focus.	85
4.3 Equilibrium positions of optically trapped dimers with varying size ratio, dashed lines represent unstable traps whereas solid lines are for stable equilibrium positions. (a) shows that dimers while in their 'standard' orientation will always have a single equilibrium position. (b) shows that when the same dimer is in its' 'inverted' orientation can be trapped in two axial positions, one below the focus and one above the focus.	87

List of Figures

4.4	Map of $z - \theta$ phase space using a dimer of size ratio 2 with a laser power of 500 mW ($\theta = 0^\circ$ is the 'standard' orientation and $\theta = 180^\circ$ is the 'inverted' orientation). The stable configurations are indicated by the larger circles and the starting conditions are colour coded to match the stable point they end up in. Right hand render shows a dimer in its off-axis configuration.	89
4.5	Rotation frequency vs component phase difference for differently sized dimers. The solid lines represent the rotation rate experienced while the dimer is in its standard orientation, whereas the solid points are for the case where the orientation is inverted. Laser power = 100 mW.	91
4.6	Figure reused from [125]. (a) shows how the momentum density of a Gaussian beam is twisted while using circularly polarised light. The top row (figures (b)-(d)) shows a 7 sphere cluster trapped in a circularly polarised beam. Due to the clusters asymmetric susceptibility to polarization the cluster rotates in the $x - y$ plane. Whereas the bottom row (figures (e) - (g)) show the similar results for a single sphere. In this instance the sphere does not rotate but instead orbits the beam axis. In both instances the motion is proportional to the degree of polarisation (see figures (d) and (g)) but for the single sphere this motion is only revealed when using (4.2) & (4.3). Reused with permission from author	93
4.7	Optical torque experienced by a dimer ($a_I/a_{II} = 10$) and a single isotropic sphere. Both were rotated in the $x - z$ plane and the angle between U_z and the beam axis gives the polar angle. The solid lines denote the torque experienced by the dimer whereas the dashed lines represent the torque experienced by the sphere.	94

List of Figures

4.8	Rotation rate plotted against dimer size ratio while trapped in a circularly polarised beam; a positive rotation rate indicates clockwise rotation, whereas a negative rotation rate indicates counter-clockwise rotation. The red line is for the case of a dimer in its 'standard' orientation. The blue line is for the case when the dimer is in its 'inverted' orientation while trapped above the focus of the beam. And lastly the green line is for the case when the dimer is in its 'inverted' orientation, but when it is trapped below the focus of the beam.	95
4.9	3 second trajectory of a dimer ($a_I/a_{II} = 2$) trapped in an off axis orientation with a circularly polarised beam ($P = 100 \text{ mW}$). The far left column depicts the dimer's centre of mass position with time; middle two columns are the x , y , and z components of the vectors u_x and u_y ; last column depicts the components of the vector u_z which defines the dimer's orientation.	97
4.10	Recorded power spectra fitted to eq. 2.49, scattered points represents the blocked data ($n_b = 100$). Corner frequency for the Lorentzian curves are reported in the legend.	99
5.1	Intensity distribution (as defined by (5.3)) from a symmetric dimer when irradiated by the probe beam propagating in the $k\hat{z}$ direction (viewed in the z-y plane). Axis are given in dimensionless units of $k\hat{z}$ and $k\hat{y}$	106
5.2	Normalised difference between the central pixel intensity $I(\theta, \phi)$ and the average pixel intensity over the surface of the optical fibre $\langle I \rangle$ as a function of distance. 4 different optical detectors were tested (spherical coordinates are given in the legend). While the choice of coordinates is arbitrary they all demonstrate the same exponential decay. Dashed lines indicate the difference after $20\mu\text{m}$ from the trap focus, in most practical cases getting an optical fibre any closer would disrupt the trap stability.	107
5.3	(a)Example dimer in orientation \hat{s} , (b) 30 Reference orientations represented by vectors pointing from [0,0,0] to each point	108

List of Figures

5.4 (a) Distribution of orientation vectors and (b) their respective scattering signals. Points are coloured according to their distance from the centre of each cluster (red points centred around [0.00, 0.00, 1.00], blue points centred at [0.71, 0.00, 0.71])	110
5.5 Simulation results of: (a) the dimer's orientation vector with time, (b) the dimer's [x,y,z] position with time.	113
5.6 Model's estimation of dimer orientation over the simulation time, assuming uniform prior $p(\hat{\mathbf{n}}_\alpha)$, broken up into x, y, and z components for clarity. Blue line denotes the best result we can achieve (the reference orientation $\hat{\mathbf{n}}_{best}$ that is closest to the actual orientation), orange line denotes the result provided by eq 5.6: where the blue line is not visible, the model's prediction agrees with $\hat{\mathbf{n}}_{best}$. Dotted black line is the instantaneous orientation $\hat{\mathbf{s}}$	115
5.7 Estimation of dimer orientation with $p(\hat{\mathbf{n}}_\alpha)$ defined by Eq (5.12). Blue line denotes the best result we can achieve, orange line denotes the result provided by eq 5.6. Dotted black line is the instantaneous orientation $\hat{\mathbf{s}}$ (see Section ??).	117
5.8 Model estimates of orientation when neural net has been trained on dimer of size ratio: (a) 1:2 [$\langle D_{KL} \rangle = 0.519$], (b) 1:2.05 [$\langle D_{KL} \rangle = 3.706$], (c) 1:1.95 [$\langle D_{KL} \rangle = 3.705$] ($n_{refs} = 30$)	118
5.9 Model estimates of orientation when neural net has been trained on dimer of size ratio: (a) 1:2 [$\langle D_{KL} \rangle = 0.593$], (b) 1:2.05 [$\langle D_{KL} \rangle = 5.659$], (c) 1:1.95 [$\langle D_{KL} \rangle = 3.279$], ($n_{refs} = 126$)	118
5.10 Model prediction for signal error of (a) 1% [$\langle D_{KL} \rangle = 0.962$], (b) 15% [$\langle D_{KL} \rangle = 13.654$], and (c) 25% [$\langle D_{KL} \rangle = 13.017$].	120
5.11 Model prediction for signal error of (a) 1% [$\langle D_{KL} \rangle = 1.447$], (b) 15% [$\langle D_{KL} \rangle = 4.670$], and (c) 25% [$\langle D_{KL} \rangle = 7.911$], time averaged over 1 ms	120

List of Figures

List of Tables

3.1	Results from rotating Vaterite within supersaturated solution of H_2O and Glycine. Solubility concentration for Glycine at 16° was $C^* = 0.2016g/g$	66
4.1	QPD fitting for single sphere	99
4.2	QPD fitting for symmetric dimer	100

Preface/Acknowledgements

I would like to acknowledge...

Chapter 0. Preface/Acknowledgements

Chapter 1

Introduction

Crystallisation is one of the oldest forms of phase separation used by humanity[1], put simply, it is the formation and growth of a new structured phase within a disordered bulk phase. This has applications in a number of industries such as pharmaceuticals [2], food production [3], and electronics [4]. Where the extraction of dilute materials can help improve product quality while keeping production costs low. The industrialisation of crystallisation has allowed engineers to reliably and efficiently induce the crystal formation within a bulk phase. However, while on a large scale crystallisation is seemingly an understood physical process, just a small amount of investigation into the literature reveals that at a micro scale there is yet to be unifying theory that can accurately explain the process of crystallisation [5]. Crystallisation can be subdivided into two steps: Nucleation and Crystal growth. The latter focusing on how an already stable crystal grows and how it takes on its final shape. Whereas the former is more concerned with the first initial moments of a crystals formation within a bulk phase.

In this chapter we will outline our current understanding of nucleation, why there is a gap in the literature, and why there is still a need for local control of nucleation events. Furthermore, we will also highlight recent developments involving the use of optical tweezers (and other laser based methods) in order to develop our understanding of nucleation. Lastly we highlight the connection between optical tweezer's ability to probe fluid viscosity via rotational motion, and the known link between nucleation and fluid flow, to propose a novel potential method of creating localised nucleation events.

1.1 Nucleation

Nucleation is an example of a binary phase separation, where a dilute phase is miscible in a bulk phase, more often called the solute and solvent respectively. Because of thermodynamics, the two can only remain in equilibrium while below a specific concentration (C_{eq}) - below which the chemical potential μ for a miscible solution is greater than the potential required to separate the two phases. Once C_{eq} is exceeded there is a chemical potential difference driving the solution to separate the two phases. Since different combinations of solute and solvent will have different equilibrium concentrations, researchers often instead measure the ratio between the solute and solvent by using 'supersaturation' [6]:

$$S(T) = \frac{C_{sol}}{C_{eq}(T)} \quad (1.1)$$

Where C_{sol} is just the solute concentration, and $C_{eq}(T)$ is the equilibrium concentration at temperature T . While the solution remains supersaturated there is a chemical potential driving the solute to coalesce and separate from the solution as an ordered solid, the first formation of the crystal is referred to as the nucleus and understanding its formation has been the focus of researchers for decades now. Typically, for an industrial crystallisation process the working principle is based on controlling and manipulating the supersaturation of the system.

1.1.1 Primary & Secondary nucleation

From an industrial perspective, the nucleation process can be broadly categorised into either primary or secondary nucleation. The former describes the formation of an initial nucleus within the bulk phase, absent of any external stimuli. Primary nucleation is therefore considered stochastic as there is no reliable means of predicting where a nucleus may form, or how long it will take. The only reliable indicator being that higher supersaturations will result in faster nucleation rates. At a small scale one can estimate the nucleation rate by making repeated measurements of sample solutions and seeing how many have nucleated after a given time, giving us a Poisson probability

Chapter 1. Introduction

distribution.

$$P(t) = 1 - \exp[-JV(t - t_g)] = \frac{M^*(t)}{M} \quad (1.2)$$

Where J is the nucleation rate, t_g is the 'growth time', V is the volume of the individual samples, and $M^*(t)$ & M are the number of nucleated samples and the total number of samples used respectively. While this is useful for studying the effects of different parameters at a small scale, for industrial applications there are too many external factors for primary nucleation to be measured accurately.

Secondary nucleation is the result of a initial seed crystal inducing further nucleation within the bulk solution [7]. The seed crystals is often specially prepared ahead of time and added to a supersaturate solution. Due to interactions with the surrounding fluid and the container walls it is possible for the seed crystals to act as a surface for further nucleation [8]. Control of secondary nucleation events are crucial for ensuring reliable industrial crystalliser performance. Fig. 1.1 depicts an attempt of classifying every possible mechanism that could lead to secondary nucleation.

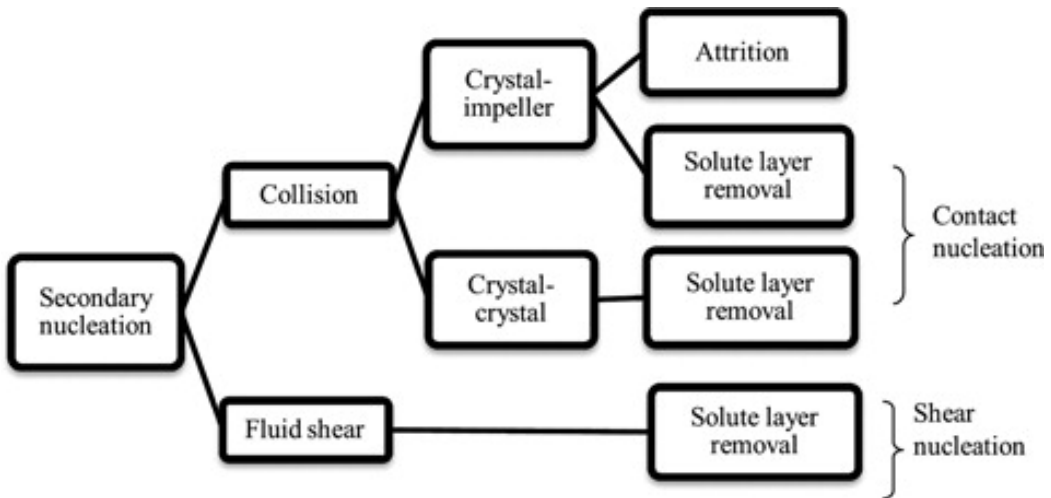


Figure 1.1: Secondary Nucleation mechanisms, classified by Agrawal and Paterson [9]

This is not a universal classification system, there are a variety of opinions on how best to characterise different phenomena. It is heavily dependent on the theory used to describe nucleation events, this is accurate for both secondary and primary nucleation.

1.2 Nucleation Theories

Several potential theories have been proposed to explain how nucleation occurs at a microscopic scale. In doing so we could potentially predict the expected yield of a given crystalliser based on the initial conditions of the solution. Outlined below are some of the most popular theories currently used to describe nucleation.

1.2.1 Classical Nucleation Theory (CNT)

Sometimes referred to as 'Gibbs Nucleation Theory' the original theory was first formed from the works of Volmer and Weber, and Frenkel [10], [11]. While initially it was more focused on describing droplet formation in condensing vapours it was extrapolated to describe crystallisation. The central premise of classical theory is that nucleation occurs stochastically due to collisions between individual solute molecules, ions, or atoms. At the same time the bulk phase is resistant to the formation of a new phase. The competition between these random collisions and the bulk solution can be used to predict the probability of a newly formed nucleus.

Consider a supersaturated solution, after some time enough individual sub units collide, forming a nucleus of volume $4\pi r^3/3$. The newly formed phase has a lower chemical potential than the surrounding solution, reducing the free energy of the system. Simultaneously, the formation of a new interface is resisted by the bulk phase due to surface tension. The net free energy of the system for a nucleus of radius r is given as [12]:

$$\Delta G = \frac{-4\pi r^3}{3v} k_B T \ln(S) + 4\pi r^2 \sigma_{inf} \quad (1.3)$$

Where S is the supersaturation from eq. (1.1) v is the approximate volume of an individual molecule, k_B is the Boltzmann constant, and σ_{inf} is the interfacial tension of the bulk solution. This assumes that the nucleus will have a spherical morphology so that the surface tension σ_{inf} is a scalar value. Looking at (1.3) suggests that there must be some critical size r where the free energy gain from the nucleus exceeds the surface tension of the surrounding fluid. This is reflected in fig. 1.2 where we plot the

Chapter 1. Introduction

free energy of the system against nucleus size. This reveals a critical size above which the gain in free energy exceeds the interfacial tension. Furthermore fig. 1.2 shows how increasing the supersaturation of the system reduces said barrier.

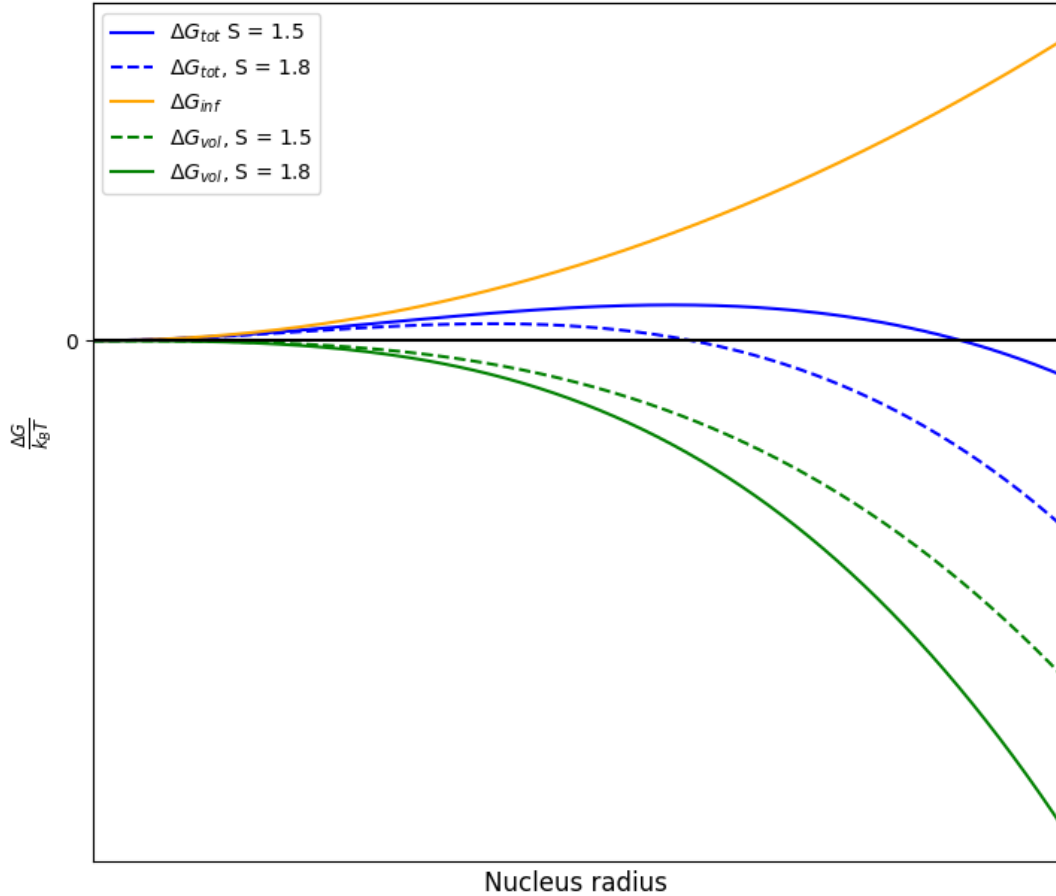


Figure 1.2: Free energy diagram of a newly formed nucleus according to the Classical Nucleation Theory. The total free energy (blue) is due to the competition between the volume free energy gain (green) and the interfacial free energy cost (orange). Dotted lines are for a higher supersaturation than the solid lines, the interfacial energy cost is independent of supersaturation.

The maximum value of ΔG_{tot} is the free energy barrier that any newly formed nucleus needs to overcome in order to stabilise. The nucleation rate (the volume of new crystalline material formed per unit time), is therefore commonly defined as being

dependent on the energy barrier ΔG^* :

$$J = A \exp \left[-\frac{\Delta G^*}{k_B T} \right] \quad (1.4)$$

Where A is a pre-factor that can be fine tuned to the exact demands of the system, the free energy barrier can be found by finding the stationary point of ΔG_{tot} .

CNT is often regarded as a good description of the macro system, its obvious that for all crystallization systems there is an inherent energy barrier that dictates the nucleation rate. Where it falters is in its predictive ability, both in estimating nucleation rates [13], [14], and in the structure of newly formed nuclei [15], [16]. Recent studies suggest classical nucleation is merely one of many possible pathways that can be taken to produce a structured crystalline phase. Prompting the development of alternative theories to better describe the nucleation process.

1.2.2 Two Step Nucleation

The two step nucleation theory is an extension to the CNT that suggests that prior to nucleation, the solute will cluster together. This has been shown via colloid simulations using protein molecules that have significant short range interactions [17], [18]. These interactions allow for the formation of a liquid-liquid metastable phase from which a new solid phase could form [12], [19]. Several papers later reported the presence of stable liquid-like clusters that formed prior to nucleation [17], [20], [21]. The formation of these clusters can be understood by Oswald's rule; which says that any crystallising system does not immediately take the path to the lowest possible energy state but instead first transitions to the state with the smallest free energy barrier [22]. Further phase transitions can still occur but this pathway minimises the overall free energy cost. Initially it was suspected that the formation of the dense liquid phase was a result of stochastic density fluctuations in the system. However, simulations suggest that the local bond order is a stronger driving force than the local density [23]. Studies into two step nucleation in Glycine solutions have noted that the solutions need to be aged before the presence of clusters was detected [24]. This suggests that there exist further

Chapter 1. Introduction

barriers to the formation of clusters in some systems, this has lead to instead calling this phenomena as Multi-step Nucleation.

1.2.3 Non-classical Nucleation

The current research into two step nucleation (or now more commonly referred to as multi-step nucleation theory) is developing a robust framework to describe what nucleation pathway will occur given the initial conditions. Reviews of all currently documented nucleation pathways highlighted the need for the development of *in situ* techniques that can induce nucleation locally but can also reliably identify the nucleation pathway across a broad range of experimental conditions [5], [12].

1.3 Crystallisation methods

1.3.1 Cooling Crystallisation

For some binary mixtures the supersaturation is heavily dependent on the solution temperature, therefore a simple method of producing crystals is by cooling the mixture to induce crystal formation. At ambient temperatures the solute concentration is too high to be fully incorporated into the solution ($S \gg 1$), after heating however the solute is fully dissolved into the solution ($S < 1$). Now as the mixture is allowed to cool to room temperature the supersaturation will increase until crystal formation begins, the rate of cooling drastically influences the size and number of crystals produced.

If dT/dt is high then the final product will consist of large crystal and be low in number, as the nucleation rate is directly related to the supersaturation only a handful of nuclei can form before the remaining solute grows onto the surface. If dT/dt is low then the final product will consist of smaller crystals and be far more numerous, as the supersaturation is so large that the new nuclei are forming continuously. Between these two extremes, one can define a meta-stable zone, a region in the temperature-concentration phase space where both nucleation and crystal growth can be reliably controlled. The lower limit being given by the solubility curve of the binary mixture, and the upper limit being defined by the point where crystals begin to spontaneously

nucleate within the solution.

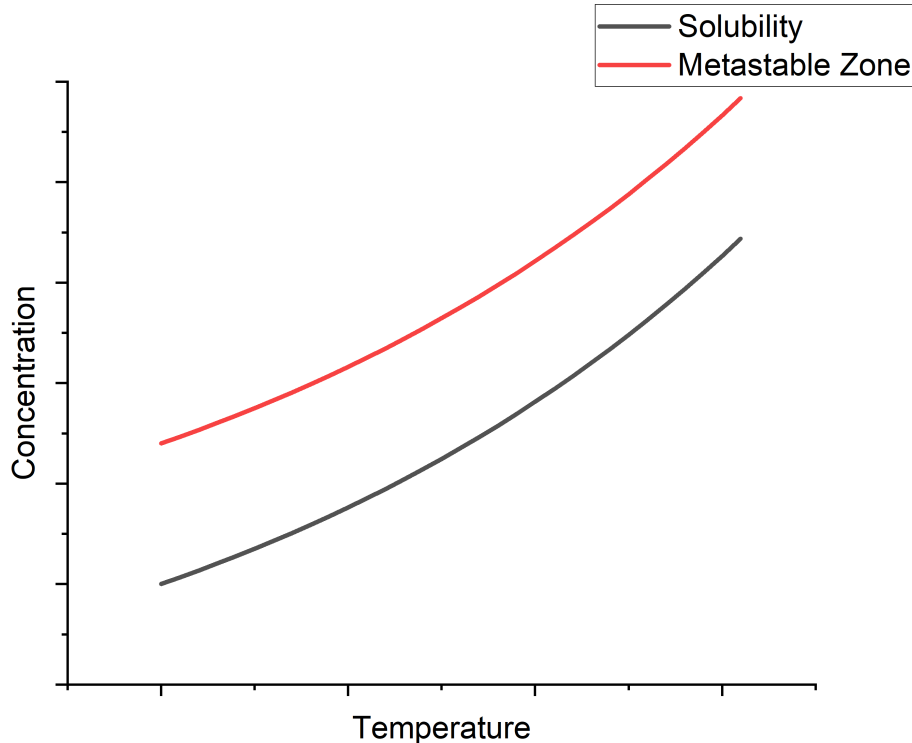


Figure 1.3: Typical Concentration vs Temperature plot with the solubility curve (black) and metastable zone (red). 3 different cooling curves are shown as well: a high rate of cooling (orange) shows the mixture quickly dropping below the solubility curve resulting in no new nuclei forming. A low rate of cooling (green) shows the mixture exceeding the metastable zone, where now nucleation occurs spontaneously and cannot be controlled without further cooling. A typical cooling rate (blue) shows how a typical cooling crystalliser will operate, sitting in the middle of the other two curves.

The viability of cooling crystallisation is dependent on the meta-stable zone width, too narrow and the process is difficult to control, too wide and the crystal growth rate may be insufficient for the desired outcome.

1.3.2 Evaporative Crystallisation

In situations where control of the final product size or shape is not the main focus, often the cheapest method of producing a crystalline product is simply to allow the solvent

Chapter 1. Introduction

evaporate and separate from the solute. Depending on the total volume of solvent to evaporate this process can take on time scale of several days to complete. This is often used for the formation of seed crystals when larger seed crystals are required [25], [26].

1.3.3 Anti-solvent Crystallisation

Anti-solvent crystallisation is a more involved separation method, by adding a new solvent that is miscible with the old solvent but is immiscible with the solute, the solute's effective solubility is decreased. As such, the solution becomes supersaturated. This has the trade off in that the overall mass ratio between the solvent and solute is now lower. Careful measurement of the anti-solvent is required in order to ensure that the decrease in solubility is not out matched by the decrease in mass ratio. Anti-solvent crystallisation is not as common due to the fact that not all solutions will have an ideal anti-solvent candidate.

1.4 Optical Tweezers

1.4.1 Background

Optical tweezing has been a field of applied optics ever since the 1980s when Ashkin [27] first showed that focused light was capable of trapping micron sized particles due to light exerting 'radiation pressure'. The working principle was that a light source such as a laser could trap small objects within a 2D plane, as long as the light source had an approximately Gaussian profile (colloquially called a Gaussian beam). Soon after, Ashkin showed that the introduction of a microscope objective would allow one to focus the light source to a diffraction limited point that would stably trap small objects within a confined volume [28]. This allowed Ashkin and others to study individual biological cells as the overall force was on the order of $10^{-12} N$ while being non-invasive to the internal structure. Later it would be used to probe microscopic properties such as the formation of colloidal aggregates [29] to the drag forces exerted by a pure vacuum [30], [31]. Due to the predictable behaviour of light, optical tweezers have become essential for measuring and exerting precise forces on the magnitude of pico-newtons allowing

one to probe the material properties of the smallest materials.

1.4.2 Literature related to laser induced nucleation

From as early as 1996 it has been known that laser irradiation using a Gaussian beam is a viable method of inducing nucleation within a supersaturated solution [32]. The first reported case was notable as it used a $1.064\ \mu m$ laser, the glycine solutions would appear transparent to such a laser which would suggest there was no photo-chemical reaction. Later studies into this phenomena found that the laser polarisation can influence the polymorph produced. With circularly polarised light producing α -glycine and linearly polarised light forming γ -glycine [33]. Future research has found nucleation can be induced by 1 of 3 routes.

1.4.2.1 Non-Photochemical Laser Induced Nucleation

Non-photochemical laser induced nucleation (NPLIN) involves irradiating a solution with a pulsed laser [32]–[34]. The laser itself does not have to be heavily focused, instead irradiating a large region of the solution all at once. The choice of laser is of particular importance; with nucleation probability changing depending on the wavelength. A study of KCl solutions found that for lower intensities it was found that nucleation was favoured for lower wavelengths but above a peak intensity of $5\text{MW}/cm^2$ the wavelength independence disappeared [35]. Measurements of the intensity prior and after irradiation confirmed this wavelength dependence was not due to any photo-chemical interactions [35].

Additionally, the choice of solute will effect the setup, not only because some solute's are unaffected, but also because there is a minimum laser threshold before nucleation is observed [33]. Several papers have debated the exact mechanism that induces NPLIN [33], [36]. A suggested theory to this is an optical Kerr effect: For anisotropically charged solute molecules the electric field can reorient them to match the propagation direction [33]. If enough molecules are co-aligned the free energy barrier is reduced to allow for ambient nucleation [36]. An alternative theory is the dielectric polarisation effect, in conditions that are unfavourable to cluster formation the polarising effect can

stabilise the clusters [37]. As the cluster concentration rises so does the likelihood of nucleation [14].

Both theories are similar to one another but where the optical Kerr theory is limited to anisotropic solute molecules, the direct polarisation theory is more flexible. Regardless both theories struggle to explain why the phenomena is not observed in all nucleation systems [38], such as acetamide which is similar to urea which does nucleate when irradiated [39]. One of the benefits of NPLIN is that since the pulses are relatively low in their intensity they can be fired off quickly in succession, allowing for continuous crystallisation set ups. Overall, the NPLIN phenomena needs further research to properly describe its effects. The mean pulse intensity needs to be kept relatively low (on the order of $0.1 - 0.01\text{GW}/\text{cm}^2$), as high intensity pulses lead to a completely different nucleation mechanism.

1.4.2.2 High Intensity Laser Induced Nucleation

High intensity laser induced nucleation (HILIN), where the pulse intensity is on the order of several PW/cm^2 is far simpler a mechanism to explain in comparison to NPLIN. The production of nuclei can be wholly associated to a cavitation process within the target solution, where the laser focus results in thermo- cavitation and the subsequent pressure wave leads to a nucleation event around the focus of the laser [40]–[42].

What remains in question is both how the physical properties (size, polymorph, etc) are influenced by the cavitation process, and how the pressure change triggers nucleation. The former has already been investigated; by adjusting the focal position Ikeda *et al* could control the polymorph of indomethacin [43], this is not a universal method however, as it has also been shown that laser power can influence the crystal polymorph [44]. The latter is a tricky task to address due to the fact that these cavitation bubbles form and collapse in less than $100\ \mu\text{s}$. Using fluorescence dyed proteins, researchers were able to observe a sudden spike in fluorescence just as the cavitation bubble began to collapse, they suggested that due to the collapse of the cavitation bubble the protein clusters are brought together at the lasers focal point. However, while the fluorescence imaging indicates a local concentration increase it is difficult to quan-

Chapter 1. Introduction

tify this change depending on the size of the bubble [38]. It has been suggested that in theory any solution can undergo HILIN [38], but proving such a theory requires a clear understanding of the phenomena both before and after cavitation occurs. Current research aims to combine experimental research with computer simulations to develop a universal theory, with the hope that this could also be related to NPLIN.

1.4.2.3 Trapping Induced Nucleation

Lastly, there is trapping induced nucleation, this is where optical tweezers come into play. Due to the radiation pressure created by the focused beam, it is possible to manipulate the solute, this was demonstrated with amino acids such as glycine [45]. Whether or not a crystal forms is due to the location of the laser focus. When focusing on the cover slip, supersaturated solutions of glycine and D_2O were shown to create a dense liquid droplet of glycine and water [46], [47]. The dipole moment of the glycine molecules is too small to be influenced by the optical trap, as such it would suggest that larger aggregates are being manipulated. Applying DLS analysis to the dense liquid region showed that it was populated by clusters that would consolidate together upon being focused by the optical trap [48]. Molecular simulations of glycine solutions showed that these clusters are unstable when using pure glycine below the saturation point suggesting that the clusters are formed due to glycine reaction products [49]. When the optical trap is moved from the cover slip to the air-solution interface, nucleation would occur before a dense liquid region could form [46]. Repeated experiments where the laser is focused on the air-solution interface have lead to a variety of different nucleation events. In some instances the nucleation occurs spontaneously after a short period of time [46]. Whereas allowing a solution to age results in the formation of amorphous precursors that when irradiated will nucleate immediately [24]. The precursors are only seen when the solution is irradiated by an optical tweezer and the growth rate can be controlled somewhat by varying the laser power [24]. The reason why nucleation is only seen at the air-solution interface is due to the limited molecular mobility close to the interface. Often tweezing experiments will use a hydrophilic coating to minimise the height of the solution droplet and further limit the molecular mobility [47], [48].

Walton and Wynne discussed a plausible model for how the tweezer focus could result in a nucleation event. Put simply, when the laser is focused at the solution the radiation pressure draws in solute material, creating a concentrated region of solute. This also creates a depleted region around the focus and raises the local temperature. When the laser is turned off the depleted region around the focus quickly cools back to the ambient temperature. This sudden cooling allows for nucleation to occur just outside the focus.

Laser induced nucleation has the potential to be a viable method for *in-situ* studying of nucleation events. Using high numerical aperture lens one can localise the nucleation event to a specific region of the solution. The current issue is that the mechanism behind laser induced nucleation is not fully understood, as such it is rather difficult to modify the laser for different solution parameters. Instead it may be more effective to manipulate the solution using trapped particles. One way would to generate an optical torque on a trapped particle and therefore shear the surrounding fluid, a method that is already in common use for micro-rheological studies [50], [51]

1.4.3 Optical Torque and rotation

It has long been known that electromagnetic fields can transfer linear and angular momentum [52]; more accurately the field is said to have both orbital and spin momentum. Though there is some debate on how to decompose the total momentum into these two components [53], [54], for this project we do not need to calculate the exact quantities and will instead look at the broader effects of both components. Orbital angular momentum arises from the shape of the wavefront of the particular field in question; for simple Gaussian beams the wavefronts are uniform and equally spaced resulting in the typical radiation pressure that Ashkin and co demonstrated [28]. However, higher order modes of a Gaussian beam (for example: Laguerre-Gaussian modes) have non-uniform wave fronts meaning the orbital momentum has both angular and linear components; depending on the relative size of the target particle one can induce rotation, or orbiting [53], [55].

Spin angular momentum (SAM) is attributed to the spin density of the field, early

Chapter 1. Introduction

research has shown that the spin density is non-zero for any beam despite the fact that the total SAM transferred to a medium is 0 [54], [56]. This has sparked debate if SAM is even a physical quantity as it does not aid in the transport of energy directly [56] and so cannot be directly observed in some cases despite being non-zero. This paradox is resolved by representing the wave as an array of spin momentum loops that cancel one-another out when the medium is homogeneous. Spacial inhomogeneities cause these spin loops to no longer be equal, resulting in non-zero spin density, anisotropic mediums (such as birefringent crystal lattices) experience a transfer of spin angular momentum, imparting an optical torque.

Birefringence is a material property often seen in crystalline materials, where the crystal lattice has a different structure dependent on its orientation. Since light is composed of waves that propagate in orthogonally to one another, a birefringent material will refract light differently depending on the light's polarisation. Therefore it can be said that the material has two separate refractive indices. For circularly polarised light this inhomogeneity results in a high degree of SAM being transferred to the target object [57], [58]. The greater the difference between the two refractive indices the greater the angular momentum transfer.

The ability to transfer angular momentum has been exploited to rotate microspheres as fast as 1000 Hz while suspended in a bulk medium [58] as well as a means of measuring the local temperature and shear response of said medium [59], [60]. Calculating the optical torque applied to a birefringent material is given via:

$$\begin{aligned}\tau_{opt} = & -\frac{\epsilon}{2\omega_{laser}} E_0^2 \sin(kd(\Delta n)) \cos 2\theta \sin 2\phi \\ & + \frac{\epsilon}{2\omega_{laser}} E_0^2 (1 - \cos(kd(\Delta n)) \sin 2\phi)\end{aligned}\tag{1.5}$$

Where Δn is the difference between the two refractive indices, θ is the angle between the particle's long axis and the polarisation vector of the local EM field, and ϕ is the phase shift in the EM field. The first term represents the 'orientational' torque which aligns the long axis of the particle with the electric field, when aligned $\theta = 0$ meaning the entire term is negligible for particle's with a stable orientation. The second term is

Chapter 1. Introduction

due purely to the polarisation of the laser, for circularly polarised light $\phi = \pi/4$ thus maximising the torque transferred to the target particle. Eq. (1.5) is only applicable for particles with a known birefringence, but there are other mechanisms that result in optical torque.

A common example is shape induced birefringence. If a particle has an anisotropic shape, it is more susceptible to being polarised along its longer axis than its shorter axis. Consider, for example, an ellipsoid elongated along one of its primary axis' ($r_z > r_x = r_y$). In a plane polarised beam such a particle will align with the polarisation vector. Therefore, the particle will rotate as angular momentum is transferred along its long axis. One common feature, regardless of shape, is that a particle with shape birefringence will rotate when it lies perpendicular to the direction of propagation. This is seen most evidently with spherical dimers [30], [61] but even for elliptical particles rotational motion is only detected when their long axis is not aligned with the direction of propagation [62], [63].

Often the optical torque experienced is far greater than similar spherical particles that are birefringent [53]. Currently spherical dimers are being rotated in vacuums to measure quantum forces and torques [30], [61]. There are some alternative cases where particles are rotated while not being aligned in the plane of the polarisation. However in these cases their shape is often specifically engineered to scatter light in such a way that the net momentum change always occurs in one direction regardless of the laser polarisation [64].

Other examples of optical torque is when an anisotropic particle is aligned with the beam's direction of propagation (in which case $\theta = \pi/2$ and the first term disappears). This is analogous to an optically trapped sphere, where alongside a restoring force the particle also experiences a restoring torque. This seemingly random rotational motion is referred to as libration [53], often in typical suspension trapping situations (where the particle is suspended in a fluid) the rotational motion is washed out by the translational motion. As such, many experiments elect to trap in low pressure environments to precisely measure the optical torque being exerted by the optical trap [30]. This has lead experiments to try and achieve '0 kelvin' motion, where by trapping

Chapter 1. Introduction

a silica dimer they were able to restrict its motion using 3 optical traps simultaneously. Despite this, they found that the dimer's rotational motion about its long axis could not be controlled leading to the undesired rotational modes [65].

The detection and measurement of optical torque is still a field of intense research, not only does it have potential to understand quantum fluctuations in a particle's motion but also allows for the creation of more effective micro-rotors. The latter being especially pertinent for understanding the behaviour of fluids experiencing localised shearing.

1.5 Shear induced Nucleation

It has long been known that fluid shear rate plays a role in influencing nucleation; however, the exact relationship between shear rate and nucleation rate has only been recently understood for specific solutions. Theoretical research into shear induced nucleation suggests that there should be a slight increase in the nucleation rate at low shear rates, reaching a maximum increase in nucleation rate, and then at higher shear rates the nucleation rate begins to drop off.

This has been shown theoretically for both simple colloidal [66]–[68] and ice crystal formation [69]; however, no experimental work into these systems has been conducted to confirm these theories. There is some experimental evidence for this phenomena in simple salt and protein solutions - though the authors emphasise that mechanical agitation cannot be ruled out - there has not been a exhaustive study into the shearing effects apart from in glycine solutions. In [67] it was found that a shear rate of around 3000 s^{-1} was the maximum shear rate that would yield the highest nucleation rate. Using the theoretical model established in [66], [70] which modifies the CNT to account for the effects of a nucleus undergoing shearing, accounting for the fact that a nucleus' growth is undergoing competition between flow-mediated molecular transport and the strain applied by the flow field which inhibits the growth of the nucleus. There central conclusion (from both the theoretical and experimental results) is that there is an optimal shear rate in which the nucleation rate is maximised.

However, a question that arises from this result, if there is a optimal shear rate

in which molecular transport is maximised and strain is minimised, then surely there should also be a shear rate in which the molecular transport and strain are equal - allowing one to suspend a nucleus at a constant radius. In this scenario, the molecular transport would prevent the nucleus from dissolving, but the strain would prevent the nucleus from growing. This however would require one to be able to apply a continuous shear rate to a targeted nucleus with high precision, there is also no model for an individual nucleus in a continuous fluid field.

1.6 Significance of Thesis

As I have hoped to make clear in the above introduction, the current state of nucleation theory is rather cumbersome at a micro-level. Models such as CNT and multi-step nucleation are not sufficient for describing the myriad of potential pathways nucleation can go down. As suggested by some review articles, the best way to address this is by developing *in-situ* methods that can study the pre nucleation phase in greater detail [5]. Furthermore, the ability to localise nucleation allows for better characterisation of the kinetics of crystal growth. Laser induced nucleation stands to be an ideal method to study nucleation, as the laser output can be concentrated to a small area [38]. This fine control over the local fluid would allow for individual nucleation events to be characterised as a factor of the local fluid properties. One challenge lies in the fact that it's clear that the local fluid properties have a direct influence on the likelihood of laser induced nucleation from occurring [24], [38], [39], [47].

A way around this would be to try and induce the local fluid without directly relying on the electromagnetic field. Optical tweezers can reliably do so already by applying an optical torque to a trapped particle in order to induce fluid flow [50], [51]. It's already well documented that shearing will enhance nucleation events at a macro-level [67]. Micro-rheological studies using optical tweezing have been more interested in probing the local viscosity rather than try and use it as a means of shearing the fluid to induce crystal growth.

1.7 Overview

Overall the aim of the PhD is to study viability of using micro-rotors to generate localised fluid flow around the beam focus. The results are reported in chapter 3, this is then followed by experimental work where we use a galvano- mirror to move the beam and hence generate shear flow. While overall unsuccessful the addition of a moving beam focus showed that the growth of a nucleus can be localised around the trap focus. This presents a new insights for controlling and studying the growth of a newly formed nucleus by precise movement of the trapping focus.

The latter chapters cover computer simulations into the behaviour of microscopic spherical dimers in an optical trap. Prior research into dimers using back focal plane interferometry has mostly considered their trapping behaviour to be similar to a single sphere but with a difference in trapping strength. Computer simulations reveal a host of new behaviours dependent on the dimer's size, orientation, proximity to the trapping focus, and even the polarisation of the trapping beam. The latter in particular suggests that multi-spherical particles can act as sophisticated micro-rotors.

However, this raises its own host of experimental challenges, namely how do we characterise the behaviour of an arbitrary particle. Relying on current characterisation techniques is not possible as they are predicated on the trapping object to behave like an isolated sphere. Two novel methods of measuring rotational motion are discussed in chapter 5; firstly via a novel detection fibre method that allows for instantaneous measurements of the orientational behaviour of optically trapped ellipsoids/dimers; and secondly we create a simulative quadrant photo diode that replicates laboratory results, utilising linear regression techniques we measure the change in orientation in order to measure the optical torque applied to a non-birefringent particle.

Chapter 2

Theory and methods

The two key areas of this project cover two widely different fields; crystallisation theory, which is covered in the previous introduction section, and tweezing theory. The following chapter summarises the working principles behind optical tweezing, the differences in scattering theories, and the broader theoretical calculations used throughout the rest of the Thesis.

2.1 Electromagnetism and optical tweezing

Proper understanding of optical tweezing requires an understanding of how the trapped particle interacts with the trapping laser. From an electromagnetism perspective the laser creates a spatially and temporally coherent electric field that scatters light off of a trapped particle. The laws governing electric and magnetic fields are summarised most succinctly via the Maxwell equations. The differential forms of which are given below [71]:

$$\nabla \cdot \mathbf{E} = \frac{\rho_v}{\epsilon_0} \quad (2.1)$$

$$\nabla \cdot \mathbf{B} = 0 \quad (2.2)$$

$$\nabla \times \mathbf{E} = \frac{\partial \mathbf{B}}{\partial t} \quad (2.3)$$

$$\nabla \times \mathbf{B} = \mathbf{j} + \frac{\partial \mathbf{E}}{\partial t} \quad (2.4)$$

Chapter 2. Theory and methods

where ρ_v is the free charge density, \mathbf{j}_0 is the charge current, and ϵ_0 is the permittivity of free space.

These four equations describe how the electric and magnetic fields behave and relate to one another at a microscopic level. Any discussion of optical trapping is underpinned by the fact that in all cases the Maxwell equations must be satisfied at the macroscopic level, where one must account for the medium's interactions with the EM field. Macroscopic forms of the Maxwell equations are given below [71]:

$$\nabla \cdot \mathbf{D} = \rho_f \quad (2.5)$$

$$\nabla \cdot \mathbf{B} = 0 \quad (2.6)$$

$$\nabla \times \mathbf{E} = \frac{\partial \mathbf{B}}{\partial t} \quad (2.7)$$

$$\nabla \times \mathbf{H} = \mathbf{J}_f + \frac{\partial \mathbf{D}}{\partial t} \quad (2.8)$$

Where ρ_f and \mathbf{J}_f are the charge density and current caused by the presence of free charges in the medium, and \mathbf{D} and \mathbf{H} are the displacement and magnetising fields respectively. The latter two are defined by:

$$\mathbf{D} = \epsilon_0 \mathbf{E} + \mathbf{P} \quad (2.9)$$

$$\mathbf{H} = \frac{1}{\mu_0} \mathbf{B} - \mathbf{M} \quad (2.10)$$

Where \mathbf{P} is the polarization field and \mathbf{M} is the magnetisation field, these fields arise due to the bound charges throughout the medium interacting with the EM field.

The force exerted by an optical tweezer can be subdivided into the gradient and scattering components, for most modelling research this is how the force fields are reported. The gradient force is a conservative force brought about by the polarisation of dielectric materials which is directed towards the point of maximum intensity (for a simple Gaussian beam this would be at it's focal point) [72]. Typically, optical tweezers will utilise a higher numerical aperture lens in order to increase the intensity, thus allowing for stronger gradient forces at the trade off of decreased trapping depth.

The scattering force arises from the scattered field of the trapping beam pushing the

Chapter 2. Theory and methods

target object away from the focal point. While some trapping arrangements can induce transverse scattering forces for simple spheres the scattering force is only significant in the direction of propagation [73] The equilibrium position is found when the gradient force far cancels out the the scattering force, and the thermal energy of the particle.

2.1.0.1 Harmonic Traps

When a sphere is located at the centre of a laser the gradient force will try to recentre the sphere if it is displaced. If the restoring force is proportional to the sphere's displacement this is referred to as a harmonic trap. The ratio of the restoring force to the displacement is called the trap stiffness (denoted by κ), and is an important characteristic of the trap. Fig. 2.1 demonstrates an example case of the force-displacement curve for a simple sphere in an optical trap. Laser power and numerical aperture are omitted as the exact shape is not of importance, only the linear region about the origin.

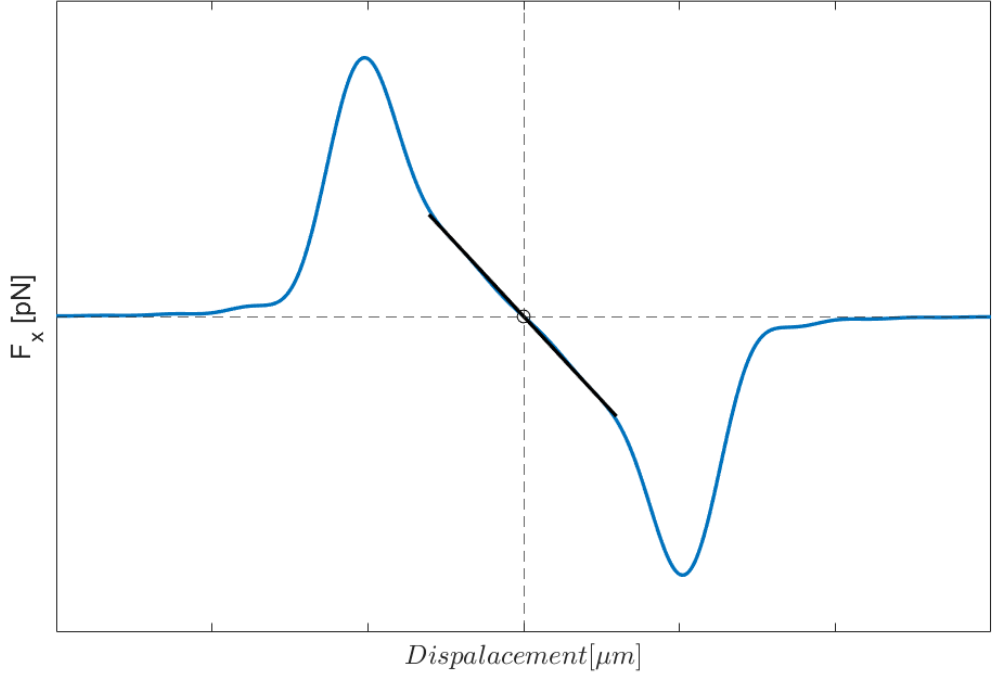


Figure 2.1: Example of a sphere's ($r = 1 \mu m$) force-displacement curve while moving along the x-axis, where $x = 0$ is the centre of the beam. The harmonic regime is highlighted by the black linear fit.

The strength of the optical trap is directly proportional to both the laser power and the contrast in refractive indices between the medium and the particle. Fully describing and calculating the optical forces is dependent on the ratio between the particle size (a) and the trapping wavelength (λ). The scattering theory for computing the optical force is dependent on this ratio.

2.2 Lorenz-Mie Theory

The Lorenz-Mie theory provides an exact solution to the Maxwell equations for the scattering caused by an isotropic sphere. This theory describes the scattered wave given off by a dielectric sphere when incident by a plane wave as a summation of partial spherical waves. For any spherical wave the vector fields must solve the Helmholtz wave equation given by:

$$\nabla^2 \mathbf{E} + k^2 \mathbf{E} = 0 \quad (2.11)$$

Where k is the wave number of the electromagnetic radiation ($k = 2\pi/\lambda$). This combined with the constraints of Maxwell's equations leaves very few exact solutions apart from spherical or planar waves. For a laser of arbitrary shape the electric field can be described as a summation of partial spherical waves multiplied by an expansion coefficient. Depending on the beam in question the expansion coefficients can be tailored to match the desired beam shape. For a Gaussian beam interacting with a particle of volume V , the incident, internal, and scattered fields are given as [74]:

$$\mathbf{E}_{\text{inc}}(\mathbf{r}) = E_0 \sum_n^{\infty} \sum_{m=-n}^n \left[a_{nm} \mathbf{M}_{nm}^{(1)}(\mathbf{r}) + b_{nm} \mathbf{N}_{nm}^{(1)}(\mathbf{r}) \right] \quad (2.12)$$

$$\mathbf{E}_{\text{int}}(\mathbf{r}) = E_0 \sum_n^{\infty} \sum_{m=-n}^n \left[d_{nm} \mathbf{N}_{nm}^{(1)}(\mathbf{r}) + c_{nm} \mathbf{M}_{nm}^{(1)}(\mathbf{r}) \right] \quad (2.13)$$

$$\mathbf{E}_{\text{scat}}(\mathbf{r}) = E_0 \sum_n^{\infty} \sum_{m=-n}^n \left[p_{nm} \mathbf{N}_{nm}^{(3)}(\mathbf{r}) + q_{nm} \mathbf{M}_{nm}^{(3)}(\mathbf{r}) \right] \quad (2.14)$$

where a_{nm} , b_{nm} , c_{nm} , d_{nm} , p_{nm} , and q_{nm} are the expansion coefficients of each of

Chapter 2. Theory and methods

the fields, and \mathbf{M}_{nm} and \mathbf{N}_{nm} are the magnetic and electric vector spherical harmonics respectively. The superscripts denote whether the field is inward [(1)] or outward propagating [(3)]. By linearity of Maxwell's equations, it's possible to relate the expansion coefficients of the scattered field directly to those of the incident field. As such we can write the scattering coefficients in terms of their incident components and the target's 'T-matrix'.

$$\begin{pmatrix} q_{mn} \\ p_{mn} \end{pmatrix} = \mathbf{T} \begin{pmatrix} a_{mn} \\ b_{mn} \end{pmatrix} = \begin{pmatrix} T_{11} & T_{12} \\ T_{21} & T_{22} \end{pmatrix} \begin{pmatrix} a_{mn} \\ b_{mn} \end{pmatrix} \quad (2.15)$$

Where the matrix \mathbf{T} accounts for the targets shape, and refractive index. The T -matrix method can be easily applied to any solution of Maxwell's equations, for example Eq. (2.14) can be instead be rewritten as:

$$\mathbf{E}_{\text{scat}}(\mathbf{r}) = E_0 \sum_{n=1}^{\infty} \sum_{m=-n}^n \begin{pmatrix} T_{11} & T_{12} \\ T_{21} & T_{22} \end{pmatrix} \begin{pmatrix} a_{mn} \\ b_{mn} \end{pmatrix} \left(\mathbf{N}_{mn}^{(3)} \quad \mathbf{M}_{mn}^{(3)} \right) \quad (2.16)$$

In order to compute the optical force and torque applied to a given object one simply needs to know the momentum carried by the incident and scattered fields. So long as we know the expansion coefficients of the incident beam we can find the scattered beam coefficients via Eq. (2.15) to compute the force. This project utilises the results from Farsund [75] but in the form used by Crichton [76]. As an example the linear momentum carried by any beam can be computed via:

$$\begin{aligned} \langle P_{z, \text{in}} \rangle &= -\frac{1}{4\pi k^2} \sum_{n,m} \left(\frac{m}{n(n+1)} \Im[a_{nm} b_{nm}^*] \right. \\ &\quad + \frac{1}{n+1} \left[\frac{n(n+2)(n-m+1)(n+m+1)}{(2n+1)(2n+3)} \right]^{1/2} \\ &\quad \times \Im[b_{nm} b_{nm}^* + a_{nm} a_{n+1m}^*] \left. \right) \end{aligned} \quad (2.17)$$

Chapter 2. Theory and methods

And the linear momentum carried by the scattered beam is given by:

$$\begin{aligned}\langle P_{z, \text{out}} \rangle &= -\frac{1}{4\pi k^2} \sum_{n,m} \left(\frac{m}{n(n+1)} \Im[p_{nm} q_{nm}^*] \right. \\ &\quad + \frac{1}{n+1} \left[\frac{n(n+2)(n-m+1)(n+m+1)}{(2n+1)(2n+3)} \right]^{1/2} \\ &\quad \times \Im[q_{nm} q_{nm}^* + p_{nm} p_{n+1m}^*] \left. \right)\end{aligned}\quad (2.18)$$

Therefore the total force imparted to the trapped particle is thus:

$$\mathbf{F}_z = \frac{dP}{dt} = P_{z, \text{in}} - P_{z, \text{out}} \quad (2.19)$$

Where $a_{nm}, b_{nm}, p_{nm}, \& q_{nm}$ are the beam expansion coefficients used in (2.12) & (2.14). Similar expressions are shown in Sec. 2.6 for calculating the optical torque. Lorenz-Mie theory can be applied to describe the scattering from any particle regardless of size, though as the size of the target particle changes - relative to the wavelength of light - the theory describing the electromagnetic fields are better easier to approximate by alternative theories. When $a \gg \lambda$ the optical force is best described by the Ray-Optics model. In the opposite case the target particle is better approximated as a single electric dipole as described by the Rayleigh approximation.

2.2.1 Ray-Optics Regime

The Ray-Optics model is the simplest to understand, this theory models the electromagnetic field as a collection of individual 'rays' that propagate and are refracted according to Snell's Law. Based on the change in direction momentum is transferred to the target particle; with rays closest to the centre of the beam having greater intensity than those rays at the very edge of the beam. Consider a particle struck by two rays in a Gaussian beam, one coming close to the centre, and the other ray coming from the edge. As each ray is refracted by the target sphere a force is imparted onto it, the total force imparted is given by:

$$F_i = Q_i \frac{\Delta n P_i}{c} \quad (2.20)$$

Chapter 2. Theory and methods

where Q_i is the trapping efficiency, Δn is the difference in refractive indices between the solution and the target particle, and P_i is the power of the individual ray. The net force can be subdivided into its gradient and scattering components, where the latter directs the particle to the centre of the beam, and the former acts on the particle in the direction of beam propagation. For a beam with a Gaussian intensity distribution P_i will fall off as you move from the centre of the beam. The ray optics model is ideal when dealing with larger particles whose diameter far exceed the wavelength of light being scattered. While it can be useful in predicting the forces experienced by said particle's it does not fully capture the behaviour of light when considering interference between different rays.

2.2.2 Rayleigh Scattering

The Rayleigh approximation is for describing a particle when $a \ll \lambda$. The underlying theory is that a dielectric sphere can be treated as a dipole while in the presence of the electromagnetic field. In which case the scattering force is given simply by the scattering of the induced dipole, and the gradient force is due to the Lorentz force [77]. The gradient forces in the principle Cartesian axis are described by Harada et al [72] in MKS units as a restorative rectangular force field:

$$F_{grad,x} = -\hat{x} \frac{2\pi n_2 a^3}{c} \left(\frac{m^2 - 1}{m^2 + 2} \right) \frac{4\tilde{x}/w_0}{1 + (2\tilde{z})^2} \times I(r) \quad (2.21)$$

$$F_{grad,y} = -\hat{y} \frac{2\pi n_2 a^3}{c} \left(\frac{m^2 - 1}{m^2 + 2} \right) \frac{4\tilde{y}/w_0}{1 + (2\tilde{z})^2} \times I(r) \quad (2.22)$$

$$\begin{aligned} F_{grad,z} = & -\hat{z} \frac{2\pi n_2 a^3}{c} \left(\frac{m^2 - 1}{m^2 + 2} \right) \frac{4\tilde{z}/w_0}{1 + (2\tilde{z})^2} \times I(r) \\ & \times \left[1 - \frac{2(\tilde{x}^2 + \tilde{y}^2)}{1 + (2\tilde{z})^2} \right] \end{aligned} \quad (2.23)$$

where:

$$I(r) = \left(\frac{2P}{\pi w_0^2} \right) \frac{1}{1 + (2\tilde{z})^2} \exp \left[-\frac{2(\tilde{x}^2 + \tilde{y}^2)}{1 + (2\tilde{z})^2} \right] \quad (2.24)$$

Where m is the relative refractive index (n_1/n_2), n_2 is the particle's refractive index, w_0 is the beam waist, a is the radius of the particle, and $\tilde{x}, \tilde{y}, \tilde{z}$ are simply the x, y, z

Chapter 2. Theory and methods

coordinates but scaled by the beam radius. The scattering force however, is dependent on the effective scattering cross-sectional area.

$$F_{\text{scat}} = \hat{z} \left(\frac{n_2}{2} \right) C_{pr} I(r) \quad (2.25)$$

where:

$$C_{pr} = \frac{8}{3} \pi (ka)^4 a^2 \left(\frac{m^2 - 1}{m^2 + 2} \right)^2 \quad (2.26)$$

There is a clear difference between Eq. (2.21)- (2.24) and Eq. (2.19), namely that the Rayleigh regime is not concerned with the state of the scattered field. This is because if the particle is approximated by a point dipole we can ignore the momentum transfer calculation and simply compute the Lorenz force for a dipole in an electric field. While not important for optical force calculation higher complexity scattering problems can be simplified by subdividing the particle into discrete dipoles (see Sec 2.3), in which case the scattered field is now significant. As the target particle gets larger this assumption fails to accurately describe the trapping force [78]. For larger particles the optical force and scattering is better described via the Lorenz-Mie theory.

2.3 Scattering methods

There are several methods available to calculate the scattered field produced by a particle. While one can compute this by directly applying Lorenz-Mie theory, describing the interactions between focused beams and complicated shapes can be computationally slow and memory intensive. Several alternative scattering approaches have been developed that allow for faster computation times simplifying the scattering problem. While all of these methods will produce identical results the key difference is in how one represents the scatterer.

2.3.1 T-matrix Method

The *T*-matrix method was first developed by Peter Waterman with his research into acoustic wave scattering [79], this would later be extended to electromagnetic waves.

Chapter 2. Theory and methods

Sometimes referred to as the extended boundary condition method (ECBM), the method replaces the scatterer with a series of surface currents over the targets surface. These currents are chosen so that the electromagnetic field outside is identical to the original problem [80]. By expanding the harmonic functions one can derive the individual elements of \mathbf{T} until a desired accuracy is achieved. One can either use the ECBM to compute the scattering for a fixed particle orientation and position. Or they can evaluate the scattering for any particle orientation by computing its T -matrix.

For this project we utilised an extension of the ECBM known as multi-sphere T -matrix method (*mstm*) developed by Mackowski [81]. Where Lorenz-Mie Theory centres the spherical harmonics expansion about the sphere's origin it often struggles to adjust the expansion to any arbitrary origin. *mstm* utilises an addition theorem to translate the individual spherical expansions from the centres of each individual sphere to a preset target origin. *mstm*'s primary function is to compute the averaged scattering from large spherical aggregates, but for our purposes it can be also utilised to compute T matrices for arbitrary shaped spherical aggregates.

The T -matrix method is exceptionally useful for computing the scattering from any arbitrary spherical aggregate. However, the T -matrix method by itself can be computationally taxing as the number of spheres increases [81]. While it is possible to solve for the full electromagnetic field of each the entire cluster this is only applicable for a single orientation and can be even slower for large aggregates [82], [83]. The benefit of *mstm* is that the major scattering properties (scattering and extinction cross sections, scattering matrices, etc) can all be computed both for single orientations, or averaged over multiple orientations to determine the average scattering from the target particle.

2.3.2 Discrete Dipole Approximation

The discrete dipole approximation (DDA) is a general method that can be applied to the scattering from particles of arbitrary composition and geometry. Developed by Purcell and Pennypacker [84], the DDA method approximates the particle as being constructed of discrete dipoles. This is essentially an extension of the Rayleigh Regime, though in

Chapter 2. Theory and methods

order to compute the optical force one requires a full description of the electric field. Each dipole interacts with both the incident field and the scattered fields from every other dipole surrounding it. The resulting scattered field is identical to the scattered field produced by direct integration of Eq. (2.13) throughout the full particle volume [85]. The integral form for the total electric field inside a scatterer is given as [80]:

$$\mathbf{E}(\mathbf{r}) = \mathbf{E}_{inc}(r) + \sum_i^{N_d} \mathbf{E}_{scat,i} = \mathbf{E}_{inc}(r) + \int_{V/V_0} d^3r \bar{\mathbf{G}}(\mathbf{r}, \mathbf{r}') \chi(\mathbf{r}') \mathbf{E}(\mathbf{r}') \quad (2.27)$$

Where $\bar{\mathbf{G}}$ is the Greens dyadic function of free space, which defines the impulse response between two separate dipoles; and χ is the susceptibility of the medium, which describes the degree of polarisation of the medium in the presence of an electric field. One of the primary advantages of DDA over the T-matrix method is that the composition of the target can be changed freely. When comparing different computational scattering methods, the ECBM was found to be better suited for simulating the scattering of symmetric targets as the ECBM can use the target's symmetry to speed up calculations [80]. But when dealing with inhomogeneous media DDA is more efficient compared to ECBM.

The DDA method can be used to derive the target's T -matrix. After generating the far field expansion of the electric field (Eq. (2.27)), the vector spherical expansion far field (Eq. (2.14)) can be matched to it. Solving for the expansion coefficients p_{nm} , and q_{nm} allows one to construct the T -matrix of the target.

2.4 Langevin Equation

Describing any microscopic motion requires an understanding of a molecules diffusive behaviour, for the case of optical tweezers the most complete model of diffusion is the Langevin equation. Models such as the Fickian, and Einstein derivations are sufficient for macroscopic behaviours the Langevin equation better describes the microscopic characteristics of any diffusive behaviour.

The Fickian model describes the net flux of solute molecules into a finite volume

Chapter 2. Theory and methods

of fluid being proportional to the density gradient $\delta\rho(u, t)/\delta u$ [86]. It assumes that the solute molecules do not collide with one another or with molecules in the solution; overall, the Fickian model is used to describe how solute molecules disperse over long periods of time. It does not provide any insight into the forces acting on individual molecules, whereas the Langevin model captures the physical interactions between an individual molecule and the surrounding fluid over a wide range of time scales.

The Einstein model of diffusion expands upon the Fickian model by considering the collisions between individual molecules. If we consider a single particle suspended in a solution it will experience multiple collisions with other molecules [87] over a given time interval δt . The Einstein model allows us to consider how individual molecules behave while suspended in a surrounding fluid. Where it begins to falter is when we consider bringing δt to 0; in this scenario the molecule experiences not many but only individual collisions. The Einstein model does not consider the inertia of the molecule in question and so for very short time frames the model implies that the molecule's velocity changes instantly after each collision [87], [88]. Furthermore, the kinetic energy of each collision is not limited by the thermal energy of the system, meaning that using the Einstein model to predict a particle's trajectory to an finite degree of accuracy implies that the particle has infinite kinetic energy [88]. This failure to describe motion over smaller time frames is addressed in the Langevin model by accounting for the fluid drag of the system, where any sudden change in velocity must result in a proportionally opposed drag force [89].

The Langevin model of diffusion assumes that the net force on a particular particle is described fully by these individual collisions [89]. Unlike the Fickian model it provides a full description of the interactions between the target molecule and the surrounding fluid; while also being able to describe its motion over any time scale, unlike the Einstein model:

$$m \frac{dv}{dt} + \gamma_0 v + F(t) = W(t) \quad (2.28)$$

Where the first term accounts for inertial forces, the second term accounts for fric-

Chapter 2. Theory and methods

tion forces which counteract the particles current motion (γ_0 is the friction coefficient), and the final term accounts for the random Brownian force. The $F(t)$ is there for convention which accounts for any external forces acting on the particle. These three terms are equal to the random Brownian motion of the surrounding fluid. We can say that the noise term $W(t)$ has a normal distribution, being scaled by the thermal energy of the system, with a correlation function of:

$$W(t) = \sqrt{2k_B T \gamma_0} \eta(t) \quad (2.29)$$

$$\langle W_i(t) W_j(t') \rangle = 2k_B T \gamma_0 \delta(t - t') \quad (2.30)$$

The Langevin model can be extrapolated to describe the diffusive behaviour of an overall system, but for this project we can instead consider the behaviour of some particle with a diffusion tensor D suspended in a viscous fluid and spacially localised by an optical potential with trap strength κ . Assuming the only external force acting on our particle is the laser, the net force should be exactly equal to force of the stochastic collisions due to the fluids thermal energy. If we focus our analysis when the particle is stably trapped and assume that the trap is harmonic, we can model the trapping force as a Hookean spring ($F(t) \approx \kappa x(t)$). The full Langevin equation for an optically trapped particle is therefore given as:

$$m \frac{\delta^2 x(t)}{\delta t^2} + \gamma_0 \frac{\delta x(t)}{\delta t} + \kappa_x x(t) = \sqrt{2k_B T} \eta(t) \quad (2.31)$$

(2.31) provides an accurate description of strongly trapped particles. Despite this the analytical solution of the Langevin equation requires integration of the noise term making it difficult to simulate the trajectory of a given particle [90]. Instead, it is often far easier to solve the equation numerically and use the analytical solution to calibrate and extract information about the particle and fluid, and how the two interact with the optical trap.

2.4.1 Finite Difference

The Finite Difference approach involves discretizing the time and spatial elements in order to approximate the higher order terms. If we assume that $x(t)$ is differentiable to n (we can find its n^{th} derivative) then we can use the Taylor series expansion to get:

$$x(t + \Delta t) = x(t) + \frac{x'(t)}{1!} \Delta t + \frac{x^2(t)}{2!} \Delta t^2 + \dots + \frac{x^n(t)}{n!} \Delta t^n + R_n(x(t)) \quad (2.32)$$

Where $R_n(x(t))$ is the remainder term between the Taylor expansion to term n and the actual expression. If we limit our approach to the first derivative only, we find that for sufficiently small values of R_1 the velocity and acceleration can be approximated as:

$$x'(t) \approx \frac{x(t + \Delta t) - x(t)}{\Delta t} \quad (2.33)$$

$$x''(t) \approx \frac{x'(t + \Delta t) - x'(t)}{\Delta t} = \frac{x(t) - 2x(t + \Delta t) + x(t + 2\Delta t)}{\Delta t^2} \quad (2.34)$$

By reversing the time step (i.e. use $-\Delta t$) to approximate the velocity and acceleration based on the previous time steps, we can discretise the position by taking finitely small time steps (i.e. $x(t) = x_i$, $x(t - \Delta t) = x_{i-1}$). The same cannot be done for noise, as no information is known about $W(t)$ at any time. We can instead say that the velocity of a Brownian particle should approximate our noise as a random walk, where at each new time step, the position changes randomly within a given range. Constricting the variance to $\sqrt{2D}/\Delta t$ allows us to represent the noise using the finite-difference approach as:

$$m \frac{x_i - 2x_{i-1} + x_{i-2}}{\Delta t^2} = -\gamma \frac{x_i - x_{i-1}}{\Delta t} + \sqrt{2k_B T \gamma} \frac{w_i}{\sqrt{\Delta t}} \quad (2.35)$$

Where w_i is a random real number between -1 and 1, we can say that it is normally distributed around 0 for simulation purposes. We can rearrange this for x_i to approximate the Brownian motion of a particle (setting $x_0 = 0$), where the characteristic time is $\tau = m/\gamma$. Now in the case of an optical trap, the restoration time scale is given by $\tau_{OT} = \kappa_x/\gamma$ which for strongly trapped particles is far greater than the characteristic

Chapter 2. Theory and methods

time. Therefore for simulation purposes, we can neglect the particle's inertia which allows the motion of an optically trapped particle to be written as:

$$x_i = x_{i-1} - \tau_{OT} x_{i-1} \Delta t + \sqrt{2D\Delta t} w_i \quad (2.36)$$

This result can be generalised for a 3-dimensional description of an optically trapped particle, where each Cartesian direction has its own unique characteristic restoration time. We see from the result that trajectory is dependent on only a handful of factors, the trap stiffness κ_x , the fluid viscosity γ , and the thermal energy of the system $k_B T$ (with the latter two being related by Einstein's formulation of the diffusion coefficient $D = k_B T / \gamma$). Therefore, by calculating these parameters to a high degree of precision allows one to get a precise description of the forces experienced by a target particle, which in the past has been used for highly accurate force transduction [91], [92].

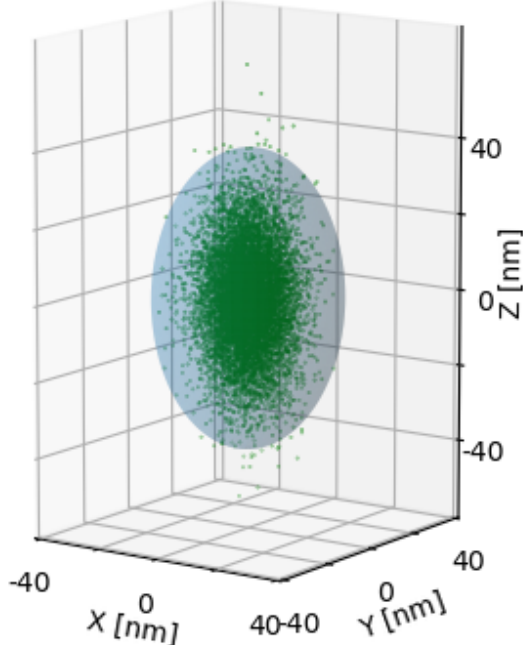


Figure 2.2: Example trajectory created using Finite Differences method for a $2\mu m$ diameter sphere. Trap stiffness's were estimated using *ott* at $\kappa_x = \kappa_y = -100 \text{ pN}/\mu m$ and $\kappa_z = -25 \text{ pN}/\mu m$. The particle's motion can be localised around the shaded ellipsoid.

2.5 Calibration Techniques

There are several approaches for calibrating and characterizing the optical trap, each approach has its drawbacks and benefits so each option should be chosen based on what elements want to be characterized. The basis for each of these methods stems from the analytical solution of the Langevin equation:

$$x(t) = x(0)e^{-t/\tau_{OT}} + \sqrt{2D} \int_0^t ds W_x(s) e^{-(t-s)/\tau_{OT}} \quad (2.37)$$

Positional data is often acquired in an experimental setting either using image analysis or photodiodes to infer the particles position relative to the beam focus. The former is often used in cases when precision is not a key concern, as often a standard CCD camera will have limited spacial and temporal resolution. The latter method often requires the use of a quadrant photo diode(QPD), the data provided by the QPD will often need to be converted to physical units to compute the force directly - see Eq. (2.50).

2.5.1 Potential Well Analysis

The Langevin equation for an optically trapped assumes that the trap acts similar to a Hookean spring that creates a potential well about its centre. Therefore a simple analysis method is to understand the height and width of said potential well.

Potential analysis is a useful technique for estimating the strength of an optical trap; this method assumes that the force acting on the particle is purely conservative, an accurate presupposition if we ignore the motion of the particle as it enters the trap. This is because the scattering force is far more significant far away from the potential well and is negligible if the trap strength is much greater than the thermal fluctuations. With this in mind we can write the probability of finding the particle at position x as:

$$\frac{\rho(x)}{\rho_0} = e^{-\frac{U(x)}{k_B T}} \quad (2.38)$$

which therefore means we can write the potential well as:

$$U(x) = -k_B T \ln \left(\frac{\rho(x)}{\rho_0} \right) \quad (2.39)$$

Now assuming our laser acts as a Gaussian beam we should be able to describe the probability distribution $\rho(x)$ centred at some equilibrium position x_0 :

$$\rho(x) = \sqrt{\frac{\kappa_x}{2\pi k_B T}} \exp \left(-\frac{\kappa_x}{2k_B T} (x - x_{eq})^2 \right) \quad (2.40)$$

By inserting (2.40) into (2.39) we can fit the potential well in order to determine the trap strength κ_x , and an estimation of the equilibrium position x_{eq} . This has some limitations in that the large fluctuations can throw off the fit meaning a longer acquisition time is necessary to properly fit the potential well, making it difficult to characterise weakly trapped particles who may not remain trapped for long. It also provides no information on the particle itself (i.e. the friction coefficient γ and diffusion coefficient D).

2.5.2 Equipartition method

The Equipartition method is by far the fastest and simplest means for estimating the trap strength but unlike Potential Analysis is limited strictly to harmonic potentials. This can be often not the case for highly focused beams, as the trap strength can vary due to polarisation differences. Simply put we can use the equipartition theorem to relate the potential well to the particle's thermal energy using (2.40):

$$\langle U(x) \rangle = \frac{1}{2} \kappa_x \langle (x - x_{eq})^2 \rangle = \int_{-\infty}^{\infty} \rho(x) (x - x_{eq})^2 \, dx = \frac{1}{2} k_B T \quad (2.41)$$

$$\implies \kappa_x = \frac{k_B T}{\langle (x - x_{eq})^2 \rangle} \quad (2.42)$$

By taking a time average over multiple trajectories to get $\langle x - x_{eq} \rangle$ we can get a fairly accurate estimation of the trap strength. Because of this requires a time average of the particle's displacement any large errors in the position measurement can have knock-on effects. Likewise with the potential analysis route, no information is gleaned

about the particle itself.

2.5.3 Mean Square Displacement

Mean square displacement (MSD) is a common means of describing the random motion of a given particle (or group of particles). This is useful information if say for example we want to understand reaction kinetics on the surface of a catalyst, if we know how far its likely to move from the surface we can tell if its likely to react when a catalytic site becomes available. As it pertains to colloids, consider a suspension of silica spheres immersed in a fluid undergoing Brownian motion (as described by the Langevin Equation) so that:

$$mx''(t) + \gamma x'(t) = \eta(t) \quad (2.43)$$

Where γ is the objects friction coefficient which for spheres is given as $\gamma = 6\pi\eta r$, and $\eta(t)$ is a random white noise variable that is directly related to the thermal energy of the surrounding fluid. If the motion is truly random then we should see an average displacement of 0 regardless of how long we measure for. If we wish to understand the effects of a given external factor (i.e. an electric field or localised heating), simply looking at displacement will reveal nothing of value as its difficult to differentiate between diffusive and a biased motion.

For each sphere we can record its position in the $x - y$ plane and measure its displacement from a set reference point; for example with an optical tweezer this could be the beam focus. We can measure the MSD by forming a 'window' between two points in time of the trajectory (i.e. t & $t + \tau$) and sliding this window along the entire trajectory length - to eliminate -ve displacements we take the square - we can then take the average of this series. Repeating over a range of time lags allows us to describe the MSD as a function of τ :

$$MSD(\tau) = \langle |x(t + \tau) - x(t)|^2 \rangle \quad (2.44)$$

If we use (2.37) for an optical tweezer we can expand out the squared term to get

Chapter 2. Theory and methods

an analytical expression for the MSD as a function of time lags:

$$MSD(\tau) = \langle |x(t + \tau)^2 - 2x(t + \tau)x(t) + x(t)^2| \rangle = \frac{2k_B T}{\kappa_x} \left[1 - e^{-\frac{\tau}{\tau_{OT}}} \right] \quad (2.45)$$

From this expression it's evident that the mean squared displacement increases with larger values of τ until it reaches a maximum value as shown below by the dotted line.

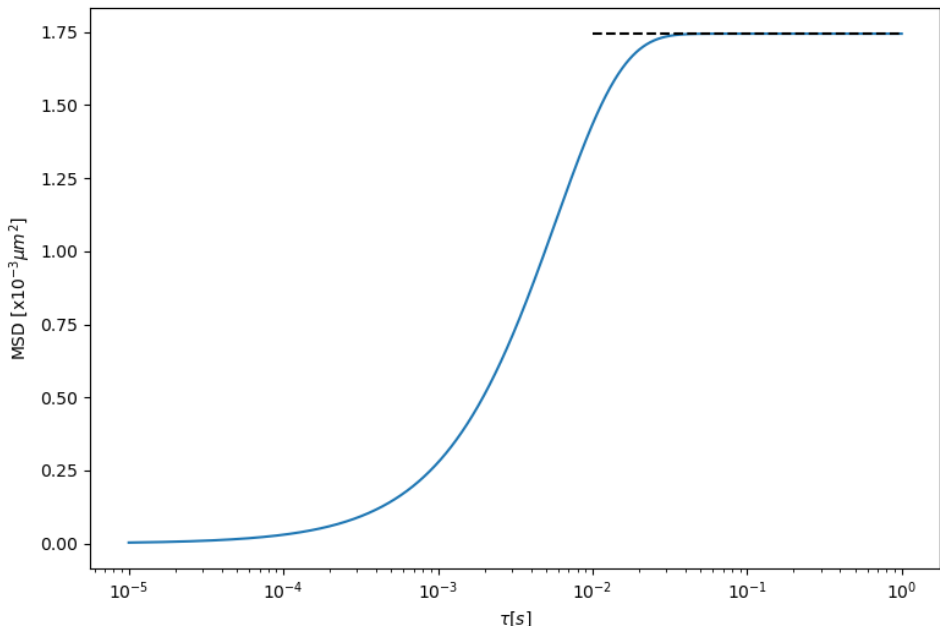


Figure 2.3: Example mean squared displacement using (2.45), for a $1\mu m$ sphere trapped by an optical potential well. The dotted line represents the upper limit of the sphere's displacement due to the optical trap.

The MSD plot can be subdivided into two regimes, when $\tau \gg \tau_{OT}$ the particle is experiencing the harmonic potential described by the equipartition theorem, and when $\tau \ll \tau_{OT}$ the particle is said to be freely diffusing within the trap focus. Of course for a freely diffusing object the MSD will never reach a plateau value, comparing MSD's for different particles provides a simple visual indicator of the difference in trapping strength. The MSD method is an already very versatile analytical tool for diffusive motion, however it is rather slow in computing time meaning it is only really beneficial

Chapter 2. Theory and methods

when a high degree of accuracy is required and shorter time resolutions are unavailable - such as using a quadrant photo diode instead or a high speed CCD.

2.5.3.1 Angular Mean Square Displacement (MSAD)

It is also possible to plot the angular MSD (MSAD) using simulative data, however using this to describe the torque acting on an asymmetric object is difficult due to fact there is no simple approximation of the rotational stiffness. Vigilante *et al* [93] derived the upper limit of a dimer's MSAD along its long axis by assuming it was strongly trapped and so had limited angular motion, there expression gives:

$$\lim_{\tau \rightarrow \infty} \langle (\Delta u_z)^2 \rangle = 2 \left[1 - \frac{1}{4\beta\kappa_r} \left(\frac{\exp(\beta\kappa_r) - 1}{\exp(\beta\kappa_r)F(\sqrt{\beta\kappa_r})} \right)^2 \right] \quad (2.46)$$

Where, u_z is the unit vector connecting the two spheres of the dimer, $\beta = 1/k_B T$, κ_r is the rotational stiffness of the trap, and F is Dawson's integral [94]. Vigilante's paper expressed that they couldn't compute $MSD(\tau)$ because they couldn't solve the Einstein-Smoluchowski equation which describes the diffusion constant for dielectric particles. This would require a full description of a particle's electrical mobility and charge distribution - the latter could be achieved via a discrete dipole approximation, the former would be dependent on both the particle's position and relative orientation to the electric field.

2.5.4 Power Spectrum Density (PSD)

The power spectral density (PSD) method is by far the most versatile method for observing the dynamics of any object within an optical trap, allowing for fast calibration times while also quickly filtering out typical noise sources. After recording a trajectory over some time t_{msr} , taking the Fourier transform of a particle's trajectory yields:

$$\hat{x}(f) = \frac{(2D)^{1/2}\hat{\eta}}{2\pi(f_c - if)} \quad (2.47)$$

where x can either be the physical position (relative to the trap focus) or a recorded signal from a position-detector, and $\hat{\eta}$ is the Fourier transform of the white noise (see

Chapter 2. Theory and methods

Eq. (2.54)). Where the values are exponentially distributed as opposed to being normally distributed in the time domain [91]. We can therefore ignore the white noise from our analysis by looking at the spectral density of $\hat{x}(f)$ that produces a Lorentzian curve:

$$S_x = \frac{\hat{x}^2}{t_{msr}} = \frac{D}{2\pi(f_c^2 + f^2)} \quad (2.48)$$

Eq. (2.48) can be fitted via a simplified geometric series $S_x = 1/(A + Bf_k^2)$ which allows us to compute both the diffusion coefficient (in arbitrary units) and the corner frequency f_c which is directly related to the trap strength via $f_c = \kappa_x/(2\pi\gamma)$. The Lorentzian shape implies that the trap is harmonic - but not symmetric - which assumes that the particle itself is an isotropic scatterer. Anisotropic scatterers can produce an Lorentzian curve if the angular component of the power spectra is insignificant. The magnitude of rotational motion (whether it is stochastic [65] or periodic [95]) will effect how drastically it departs from a typical Lorentzian curve.

Like with the analytical expression of the mean squared displacement we see two distinct regions, when $f \ll f_c$ the PSD reaches a plateau value that when converted to length units represents the maximum displacement the particle can move beyond the focus. When $f \gg f_c$ the PSD falls off exponentially which denotes the particle is freely diffusing within the beam focus.

The Lorentzian relationship is only valid for frequency terms up to the Nyquist frequency (half of our sampling rate), this is because we are only taking a finite sampling of the particle's trajectory meaning the signal is aliased. Berg and Sorensen provide a suitable modified Lorentzian to account for the aliasing effects [91]:

$$S_x = \frac{(\Delta x)^2 \Delta t}{1 + c^2 - 2c \cos 2\pi f_k \Delta t / N} \quad (2.49)$$

Where N is the total number of samples taken, Δx & c have no direct physical interpretation and are defined in [91]. Further modifications can be made to the power spectrum model but this is only useful when a high degree of accuracy is necessary. Typically power spectra are recorded using a Quadrant Photo Diode (QPD), which

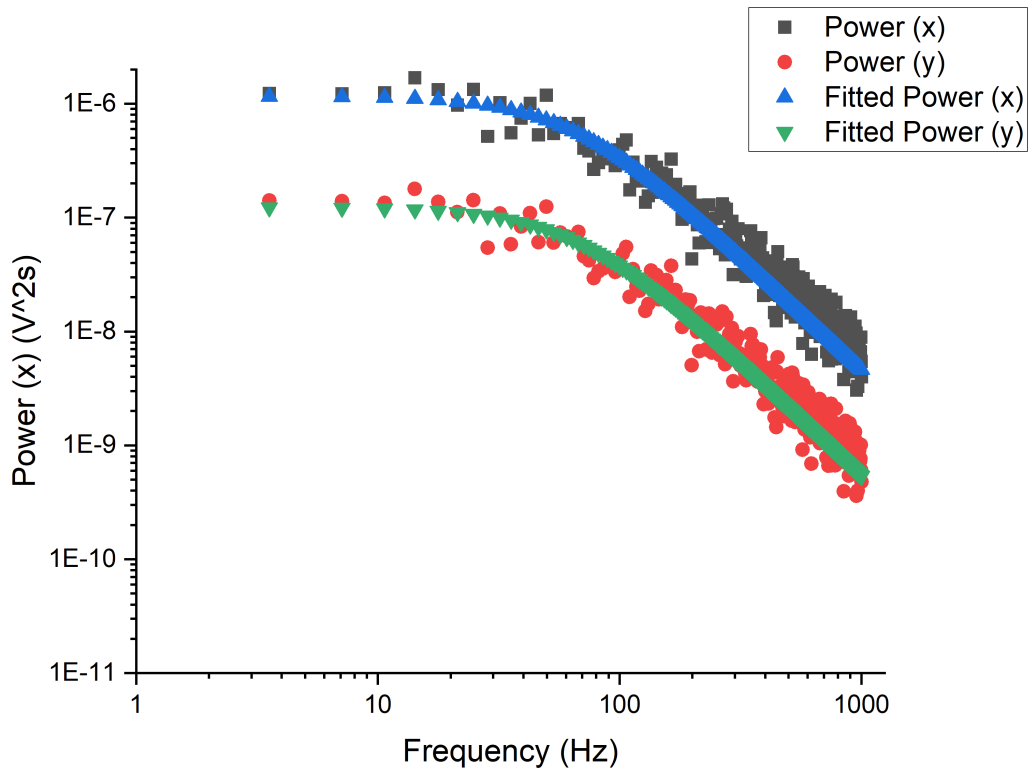


Figure 2.4: Example PSD fitted using (2.48), power spectra is collected from an optically trapped silica sphere suspended in water. The difference in magnitude is due to the asymmetry of the quadrant photo diode having a stronger signal response in the direction of the polarisation vector. Using a conversion factor (see (2.50)) will adjust the power spectra to better describe the trap shape.

records motion in voltage units, not in units of length. There are two main methods for converting to physical units: If multiple photodetectors are available then a differential interference contrast (DIC) system can be used to compute the linear relationship between the beads displacement and the photodiodes signal [73]. While this is useful when high force precision is necessary it also allows you to collect information about the particle's motion along a single direction, making it ideal for less focused beams. Alternatively, if the size distribution is very wide but each particle can be accurately sized, then a conversion factor can be approximated by comparing the fitted value of

the diffusion coefficient, and the reported value given by the Stokes-Einstein relation.

$$D_{SE} = \frac{k_B T}{\gamma_0} \Rightarrow \text{Conversion Factor } [m/V] = \sqrt{\frac{D_{SE}}{D_{fit}}} \quad (2.50)$$

With the latter method, the local fluid viscosity must be known to a high degree of accuracy, depending on the local heating effect this may be as trivial increase or it may be significant enough to drastically alter the characterisation. PSD analysis is often seen as the gold standard for calibration as it can be fine tuned to the point that optical forces can be computed on the order of $10^{-15} N$ [91], it captures all of the information acquired by other calibration techniques while filtering out noise and requiring a relatively small amount of data collected.

2.5.4.1 Power spectral analysis for rotating objects

The scattering from rotating objects can be partially characterised via the power spectrum density method. Typically papers reporting on the rotation rate of a trapped object will collect a power spectrum and look at the maximum frequency term to determine its rotation rate. However this often neglects any information on the trapping forces acting on particle and only looks at the torque applying around one of the particle's primary axis. There has only been one notable effort to fully characterise the full trapping dynamics on a rotating body, [95] developed a theoretical model that relates the power spectrum to both the rotational and translational motion simultaneously.

2.6 Simulation of spherical aggregates

Later chapters cover the dynamics of spherical aggregates and anisotropic scatterers, these subjects are particularly difficult to characterise using conventional calibration techniques [96], [97]. As an example consider a symmetric dimer as a paradigmatic aggregate; if we consider the Langevin equation for such a aggregate within an optical

Chapter 2. Theory and methods

trap we have:

$$\frac{d\vec{r}(t)}{dt} = \frac{\vec{\kappa}_x}{\gamma} \vec{r}(t) + \sqrt{2\vec{D}_x} \eta(t) \quad (2.51)$$

Where $x(t)$ is replaced with $\vec{r}(t)$ to signify that the translational motion is generalised to a 3 dimensional case. Here we omit the inertia term as the restoration time of the optical trap is far greater than the characteristic time of the particle ($\kappa/\gamma \gg m/\gamma$). Now, the dimer is undergoing random rotational motion in addition to its Brownian translational motion the first term on the right hand side is no longer purely a function of the dimer's position but also of its orientation. The rotational form of the Langevin equation for a dipole within an external potential is given as:

$$\frac{d\vec{u}(t)}{dt} = \frac{\mu}{\gamma_R} [\vec{u}(t) \times \vec{E}(t)] \times \vec{u}(t) + \sqrt{2\vec{D}_R} \lambda(t) \times \vec{u}(t) \quad (2.52)$$

Where $\vec{u}(t)$ is the unit vector aligned along the centres of the two spheres, μ is its dipole moment, and γ_R is the rotational friction coefficient which is given as $\gamma_R = 8\pi\eta r^3$ for a sphere, if the dimer is within a harmonic potential we can write the first term on the right hand side as $\frac{\vec{\kappa}_u}{\gamma} \times \vec{u}(t)$, where $\vec{\kappa}_u$ is the rotational stiffness vector. $\lambda(t)$ is the Brownian rotations from the surrounding fluid, like in the translational case the Brownian rotations are normally distributed and are also uncorrelated so that:

$$\langle \lambda(t)\lambda(t') \rangle = \delta_{ij}\delta(t-t') \quad (2.53)$$

For an asymmetric scatterer whose radius is comparable to that of the electric field's wavelength we now have a system of simultaneous equations:

$$\frac{d\vec{r}(t)}{dt} = \frac{\vec{\kappa}_x(\vec{u}(t))}{\gamma} \vec{r}(t) + \sqrt{2\vec{D}} \eta(t) \quad (2.54)$$

$$\frac{d\vec{u}(t)}{dt} = \frac{\vec{\kappa}_u(\vec{r}(t))}{\gamma_R} \times \vec{u}(t) + \sqrt{2\vec{D}_R} \lambda(t) \times \vec{u}(t) \quad (2.55)$$

Fortunately, we do not need to solve these directly as the latter two random variables can be easily approximated if the thermal energy of the system is known, and the

Chapter 2. Theory and methods

rate of change can be assumed as linear if we take a sufficiently small time step that $\Delta t \ll \kappa_x/\gamma$ & $\Delta t \ll \kappa_u/\gamma_R$. In doing so we now only need to compute the optical force and torque applied to the dimer.

Using a MATLAB package called *Optical Tweezer Toolbox* or *ott* [98] we can compute the beam shape coefficients (a_{nm} & b_{nm}) for any desired beam type. Using the results from [75] we can then compute both the optical force and torque using the beam coefficients and the scattering coefficients (q_{nm} & p_{nm}) which are found by calculating the dimer's T -matrix via *mstm* [81] and then using (2.15). The total force in along the z-direction and the total torque about the z-axis are provided:

$$\begin{aligned} \mathbf{F}_z = -\frac{1}{4\pi k^2} \sum_{n,m} \left(\frac{m}{n(n+1)} \Im[a_{nm}b_{nm}^* - p_{nm}q_{nm}^*] \right. \\ \left. + \frac{1}{n+1} \left[\frac{n(n+2)(n-m+1)(n+m+1)}{(2n+1)(2n+3)} \right]^{1/2} \right. \\ \times \Im[b_{nm}b_{nm}^* + a_{nm}a_{n+1m}^* - q_{nm}q_{nm}^* + p_{nm}p_{n+1m}^*] \end{aligned} \quad (2.56)$$

$$\begin{aligned} \mathbf{T}_z = -\frac{1}{8\pi k^3} \sum_{n,m} \left(\frac{m}{n(n+1)} [|a_{nm}|^2 + |b_{nm}|^2 - |p_{nm}|^2 - |q_{nm}|^2] \right. \\ \left. + \frac{2}{n+1} \left[\frac{n(n+2)(n-m+1)(n+m+1)}{(2n+1)(2n+3)} \right]^{1/2} \right. \\ \times \Re[b_{nm}a_{nm}^* + a_{nm}b_{n+1m}^* - p_{nm}q_{nm}^* + q_{nm}p_{n+1m}^*] \end{aligned} \quad (2.57)$$

where a_{nm} , b_{nm} , p_{nm} , and q_{nm} are the beam coefficients of the incident and scattered fields respectively. We can get the x and y force and torque components in a similar form by applying a simple rotation transformation. With the optical forces and torques computed all that remains is to compute the Brownian forces and torques which are constrained by the relation.

$$\langle q_i q_j \rangle = 2D_{ij}\Delta t \quad (2.58)$$

Vigilante et al compiled together a python package that combines both *ott* and *mstm* to simulate the behaviour of spherical aggregates within a predefined optical trap [93]. Now *ott* does have inbuilt T -matrix modules that can be used to model

the scattering from different shaped particles; however, for aggregates of spheres the resultant force is nonsensical (see Chapter 4 for further details). As such we rely on the *mstm* for simulating dimers.

2.6.1 Simulation reference frame

Throughout this project we use the work of Vigilante [93] to perform a systematic study of the dynamics demonstrated by asymmetric dimers in both plane and circularly polarised light. The simulations have two primary frames of reference that require explanation. Firstly, there is the laboratory frame which describes the coordinate system, we define the origin of our simulation as the focus of our trapping beam. While the choice in direction for the x and y axis are arbitrary the z axis is specifically chosen so that it is aligned with the direction of beam propagation.

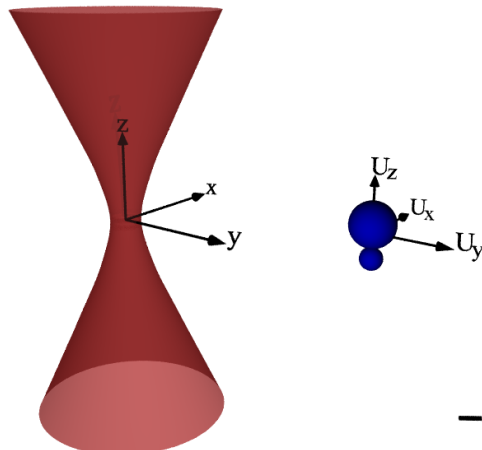


Figure 2.5: Ray scattering render of both the laboratory frame and particle frame for a dimer and a Gaussian beam. The origin of the laboratory frame is defined as the focus of the trapping beam, with the positive z -axis being aligned with the direction of beam propagation. The particle frame is centred on the dimer’s centre of mass with the primary axis U_z being aligned with the centres of the two spheres. Black line is scaled to represent $1 \mu m$.

Secondly there is the particle frame which describes the orientation state of the particle, orientations are reported as quaternions which can be readily transformed into rotation matrices. The matrix describes the direction of the particles 3 orientation

axis U_x , U_y , and U_z . The latter is oriented so that it is collinear with the centres of the two spheres; the direction of vector U_z is such that it goes from the centre of a_{II} to the centre of a_I . The origin of the 3 axis' is set on the particle's centre of mass, this is also used to define it's displacement from the origin of the laboratory frame. The diffusion tensor of the dimer is more complex than a sphere's as we must consider the rotational effects experienced by the dimer. We use the analytical solution of Nir & Acrivos [99], where they provided the solution coefficients depending on the dimer's size ratio (a_I/a_{II}). Rather than recalculate the coefficients for every possible configuration of dimer we use a spline fitting function to approximate the diffusion tensor.

2.7 Simulated Quadrant Photodiode

Beyond merely simulating the forces experienced by a spherical aggregate we also developed a simulative quadrant photo diode to replicate the results from a typical calibration test. This builds upon the work from [100] which applied Lorenz-Mie theory to replicate the response signal of a QPD being used in back focal-plane interferometry. Rather than be constrained to individual spheres we can now consider the expected response from any type of spherical aggregate.

In order to simulate a typical experimental set up with a QPD installed as a position detection system we need to evaluate the total magnitude of the electric field incident on the photo-diode surface. While trapping a micro-particle, the scattered and incident fields combine together and interfere with one another. These fields are collected by a condenser lens in the far field limit and are focused onto the QPD surface, the total intensity can be evaluated as:

$$I(x, y) = \epsilon_0 c \left| \begin{bmatrix} E_{i,x}(x, y) + E_{s,x}(x, y) \\ E_{i,y}(x, y) + E_{s,y}(x, y) \\ E_{i,z}(x, y) + E_{s,z}(x, y) \end{bmatrix} \right|^2 \times \text{step}(\theta_{NA} - \theta(x, y)) \quad (2.59)$$

The last term is simply a representative step term that defines the outer limit by which we evaluate the electric field, this is analogous to our condenser lens removing

Chapter 2. Theory and methods

noise from other light sources by only accepting light at a specific acceptance angle defined by its numerical aperture NA_c . Depending on the relative size of our particle we can adjust the acceptance angle, this has very little effect on the transverse signals, but for axial evaluations of a trapped particle the numerical aperture should be tuned so that the resultant response curve has negative slope in order to allow for axial position detection, the method for finding this angle θ_Θ is discussed in [101].

The incident beam is simple enough to define given our set up parameters, for the sake of simplicity we assume that our beam is a Laguerre-Gaussian beam of mode $[0.0, 0.0]$ (which is simply a pure Gaussian beam). *Ott* uses a point matching approach to approximate the beam shape coefficients of the incident field by fitting it to the far field estimate. From the QPD's perspective it is receiving light both from the incident and scattered beam simultaneously, as such both fields must be expressed using outgoing vector spherical harmonics.

$$E_{\text{inc}}(r) = E_0 \sum_n^{\infty} \sum_{m=-n}^n \left[a_{mn} \mathbf{M}_{nm}^{(2)}(\mathbf{r}) + b_{nm} \mathbf{N}_{nm}^{(2)}(\mathbf{r}) \right] \quad (2.60)$$

$$E_{\text{scat}}(r) = E_0 \sum_n^{\infty} \sum_{m=-n}^n \left[p_{nm} \mathbf{N}_{nm}^{(2)}(\mathbf{r}) + q_{nm} \mathbf{M}_{nm}^{(2)}(\mathbf{r}) \right] \quad (2.61)$$

Where the superscript (2) denotes an outgoing spherical harmonic function. In order to compute the scattering from the target particle *ott* uses the T -matrix method, this is not essential for a simple sphere but is essential for complex shaped particles such as dimers. The scattered and incident fields are then combined together in the far field to get $I(x, y)$, the quadrant and overall signals are calculated via:

$$Q_i = \sum_{n,m} I(x_{i,n}, y_{i,m}) \quad (2.62)$$

$$S_x = \frac{(Q_1 + Q_2) - (Q_3 + Q_4)}{\sum I_0(x, y)} \quad (2.63)$$

$$S_y = \frac{(Q_1 + Q_3) - (Q_2 + Q_4)}{\sum I_0(x, y)} \quad (2.64)$$

$$S_z = \frac{(Q_1 + Q_2 + Q_3 + Q_4)}{\sum I_0(x, y)} \quad (2.65)$$

Chapter 2. Theory and methods

Where the denominator is the total intensity on the QPD while there is no particle within the trap. The QPD sensitivity is dependent on both the polarisation of the incident beam and the displacement of the target sphere, this is shown in fig. 2.6.

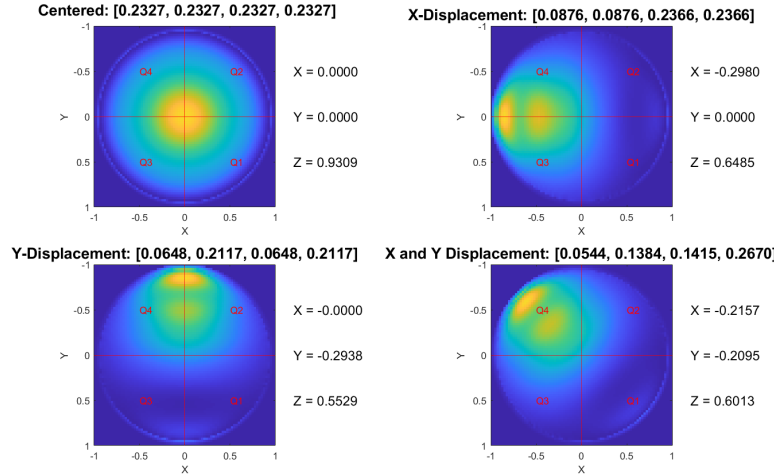


Figure 2.6: Total Field incident on the quadrant photo diode for several different displacements. Top Left: $2\mu\text{m}$ diameter silica sphere placed at the focus of a beam. Top Right: silica sphere is now displaced by $1\mu\text{m}$ along the x-axis. Bottom Right: silica sphere is now displaced along the y-axis. Bottom Left: silica sphere is now displaced by $0.707\mu\text{m}$ along the x and y axis. The trapping beam is a TEM_{00} Gaussian, polarised along the x-axis. S_x , S_y , and S_z are shown to the right of each graph, Q_1 , Q_2 , Q_3 , and Q_4 are shown above each graph.

While translational motion have no knock on effects to the QPD signal, rotational changes are between the incident and total fields. This results in rotational motion being biased in the QPD signal - even when collecting signals from isotropic scatterers. To remedy this an inverse rotation is applied to the total field.

To confirm that our method is producing accurate results, we ran a comparison between our simulative QPD and the results from [100]. Where a 300 nm diameter sphere is scanned across the path of a focused Gaussian beam ($\lambda = 1064\text{ nm}$, $NA = 1.2$), the sphere has a refractive index of 1.57 and is suspended in water ($n_{med} = 1.33$) and the condenser lens has its numerical aperture set to 0.5 ($\theta_{max} = 30^\circ$). Scanning across all three primary axis produced the following response curve:

The discrepancy between our simulated QPD and the results from Rohrbach can

Chapter 2. Theory and methods

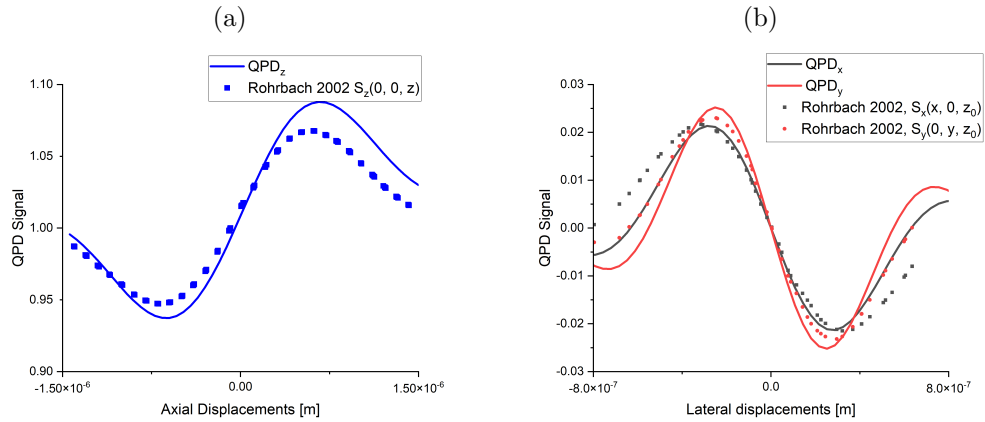


Figure 2.7: Comparison between QPD response signal versus work conducted by Rohrbach, single sphere ($r = 150$ nm, $n = 1.57$) is scanned by a 1064 nm laser and the QPD signal recorded. Solid lines represent the signal produced by QPD using *ott* and points represent the signal response collected [100].

be attributed to the fact that the position to signal error grows as you move further from trap focus. As the particle moves further from the trap focus the error in the attributed signal grows substantially [100]. In most optical trapping experiments we usually are calibrating a strong trap where the mean square displacement falls well within the linear regime shown in fig. 2.7. In which case the error between Rohrbach's model and our own is inconsequential for calibration purposes. With this any trajectory can be collected from the QPD by displacing and rotating the beam accordingly, later in chapters 4 and 5 we discuss the limits of accuracy that can be achieved using back focal plane interferometry to characterise non-spherical targets.

Chapter 3

Effects of localised shearing on crystal growth and nucleation

As outlined in Chapter 1, part of the projects aim is to investigate the possibility of using optical tweezing to induce nucleation by generating fluid flow within a supersaturated solution. The intent of which would be twofold: Firstly to have a repeatable means of inducing nucleation under different solution conditions. And secondly, to understand the influence of shearing on nucleation at a micro level as compared to results in bulk fluid.

It has been shown that for macro-scale systems, the likelihood of nucleation increases to a maximum value under increased shearing [66], [67]. Mura and Zaccione developed a theoretical framework to describe how a newly formed nucleus experiences two additional growth factors when placed in a moving fluid. Firstly, due to increased molecular transport of solute molecules the nucleation rate is enhanced in low to moderate fluid flows. But in addition, due to shear flow the crystal surface undergoes deformation which suppresses the nucleation rate undergoing faster fluid flow [66]. Experimental results with glycine solution support this theory; Debuyschere *et al* demonstrated that the nucleation rate of supersaturated glycine was enhanced up until $\dot{\gamma} \approx 3000 \text{ s}^{-1}$ [67]. After which the nucleation rate began to decrease but was still greater compared to the case where fluid flow was minimal.

Optical tweezers can been used to rotate a whole host of microscopic objects, with

the fastest reported results exceeding 1000 Hz in heavy water [58]. If such a micro-rotor was suspended in a supersaturated solution the fluid flow around it could be fast enough that the nucleation rate is locally enhanced. We focused on two primary candidates for rotation, Vaterite and 4-Heptyl-4-biphenylcarbonitrile (7CB). The former being a polymorph of calcium carbonate and the latter an example of nematic liquid crystals, both of which have been used repeatedly in previous micro-rotor research [57], [58], [102]. In addition, we also consider the application of using techniques beam steering to generate fluid flow by trapping silica micro-beads. In this instance the fluid flow is generated not due to the transfer of angular momentum, but due to shearing caused by a moving sphere through stagnant fluid.

To begin with, the discussion of the necessary optical equipment is covered, drawing attention to specialised components and techniques that are not standard in optical trapping set ups.

3.1 Optical Tweezer Equipment

In general, all optical tweezers require a laser driver, a focusing microscope objectives, a position controller, and position detector [103]. The laser used for this project was a 1064 nm near infrared laser - provided by CNI Lasers – that was focused by a Nikon 100x oil immersion lens. The choice of an oil immersion lens is important as the optical oil used prevents a loss of focus when used on a glass cover slip. Now, experimental work has shown that the trapping efficiency increases with beam diameter up until it exceeds $\frac{2}{3}D_{obj}$ [104] where D_{obj} is the diameter of the objective aperture. To expand the beam front we utilise a Galilean beam expansion arrangement (indicated by f_1 , and f_2 in Fig. 3.1) as recommended for high power laser applications. In our initial experiments the beam expansion provides a $4\times$ magnification. Whereas in later experiments we utilised a galvano-mirror the beam expansion is $3\times$ and then the 4f correlator (see 3.1.2) provides a further $1.25\times$ magnification (using f_3 and f_4) - the magnification is

given by.

$$\frac{D_2}{D_1} = \frac{f_2}{f_1} \quad (3.1)$$

It should be noted that the galvano-mirror requires the use of a Keplerian beam expansion arrangement which reduces the transmitted laser power due to localised heating of the air. Afterwards the laser is passed through a dichroic mirror that separates incoming infrared and visible light, this is to prevent the laser from damaging the CCD camera used for imaging the trapping plane. The laser is then focused to a diffraction limited spot by the objective. Utilizing a high numerical aperture objective enhances the gradient force at the focal point; the trade-off being that the for higher NA objectives the trapping depth is reduced due to spherical aberrations. While it is possible to increase the trapping depth [105] by adjusting the objective's tube length this approach is incompatible with our trapping arrangement. A 0.25 NA condenser objective refocuses the scattered laser light and also provide an aperture for an imaging LED to illuminate the focal plane. Samples are loaded onto a piezo driven table to that is inserted between the trapping and condensing objectives; the piezo drivers allow for sub-micron control of the beam focus position to a degree as small as a 10 nm. To detect and monitor the position of a trapped particle a quadrant photo diode (QPD) was utilised.

3.1.1 Position detection methods

In order to accurately capture the dynamics of a trapped particle, a position detection system is required. There are 3 possible methods of position detection: video-analysis, lateral-effect position sensing, and photodiodes.

Video analysis is ideally suited for multiple traps or situations where precision is not the top priority. Whereas lateral-effect and photodiode position detection are two examples of back-focal plane interferometry, where the interference pattern produced by the target particle is extrapolated to determine its position. In order for video analysis to match the accuracy of back-focal plane interferometry methods requires the

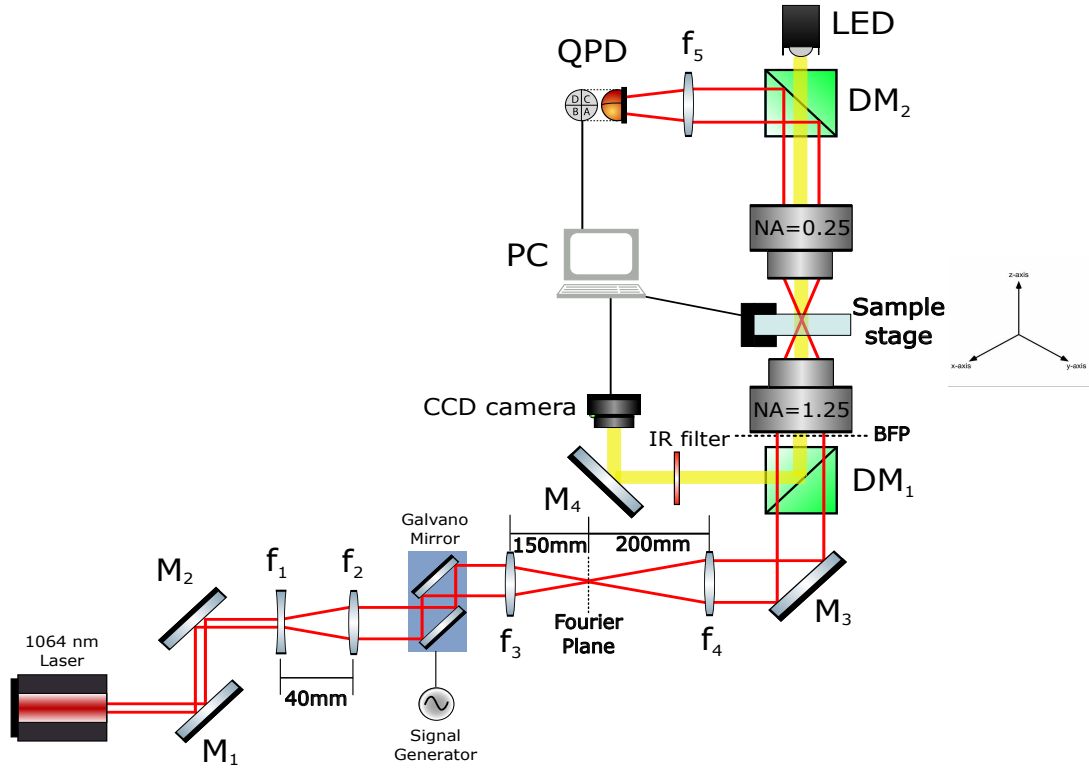


Figure 3.1: Optical tweezer set up used for the majority of the PhD. The focal lengths of f_1 , f_2 , f_3 , & f_4 are -20 mm , 60 mm , 150 mm , & 200 mm respectively [M = mirrors, DM = dichroic mirrors, f = focal lenses]. Diagram not drawn to scale.

camera's frame rate to exceed 1 kHz which can be difficult to achieve while maintaining a decent resolution [106]. In comparison off the shelf back-focal plane detectors can achieve temporal resolutions anywhere from $10 - 100\text{ kHz}$ [91].

A quadrant photo diode (QPD) is a frequently used position detection system for optical tweezers due to their high sampling rate, high degree of precision, and ease of set up. The QPD is constructed of four photo diodes assembled in a quadrant formation, when a particle is trapped the interference pattern produced is focused onto the QPD, with the maximum intensity mapping to the particle's centre of mass. By summing the voltages of the horizontal and vertical quadrants together the particle's centre of mass is tracked in the x-y plane. Axial displacement can be estimated by observing the change in the total voltage of the QPD. The outputted signal gives an indication of the particle's relative displacement from the beam focus, but in order to convert the signal

to distance units the trap needs to be calibrated (assuming a linear response curve).

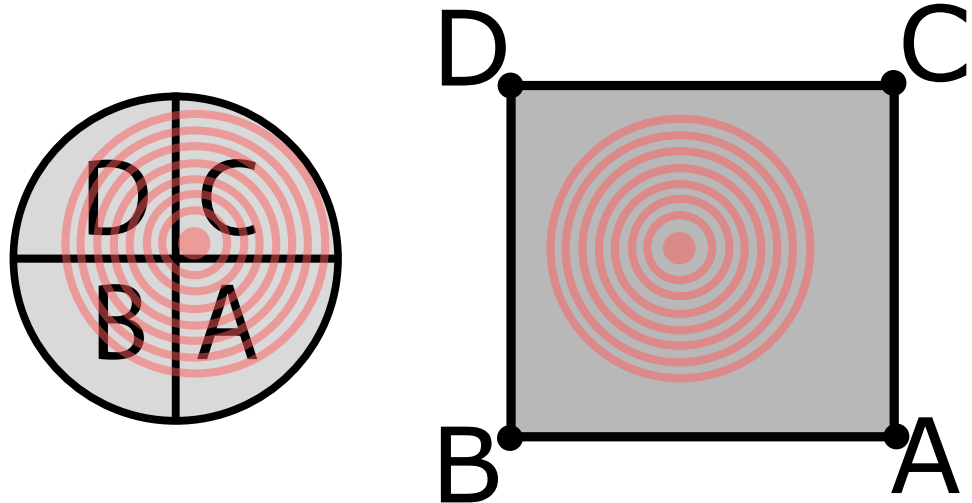


Figure 3.2: Comparison between QPD and Lateral effect photodiodes. The four quadrants of a QPD (left) experience different photocurrents based on the total intensity of light incident on each section (labelled A, B, C, D). Whereas a Lateral effect sensor (right) uses the resistive properties of the photodiode surface to vary the current passing through the anodes A, B, C, and D.

A lateral-effect sensor has a similar output but works using the entire sensor as a single cell analogous to the focal plane of the trapping beam. The four corners of the sensor act as anodes connected to a base plate cathode, as the beam moves across the surface of the detector each anode will experience a different photocurrent depending on how close the centre of the interference pattern is to each anode. The advantage of a lateral effect detector is that the linear regime is much larger than a QPD making it much better for monitoring the position of a trapped particle. However, Lateral-effect sensors are often limited in their spatial resolution due to high signal-to-noise ratios, requiring a high intensity of light on the sensor in order to get a clean signal. As a result, most optical force measurements are conducted using a QPD as opposed to a lateral-

effect sensor, as often the displacement is small enough that the signal-displacement curve can be considered linear.

3.1.2 Fourier Optics and 4f correlators

As shown in 3.1, after the Galvano mirror there are a pair of focal lenses (f_3 and f_4) that do not seem to serve a clear purpose. These are in fact crucial for the operation of the Galvano, the pair of them can be more accurately called a 4f correlator.

A 4f correlator is an example of Fourier optics in practice, understanding that a focused lens takes a Fourier transform of the light profile. Consider a laser with a circular Gaussian profile, if you were to place a detector there you would pick up the intensity as a function of its position within the beam. If however you focused the light into a single point (using a +ve focal lens) you are actually seeing a measurement of the phase of your laser with position, in which you would see a diffraction limited spot ($d = \lambda/2nsin(\theta)$), indicating that the laser is collimated. In imaging systems, a series of focal lenses can be used to filter out unwanted scattering from an image (or in an inverse case differentiate between different images), the placement of each lens is shown via fig. 3.3.

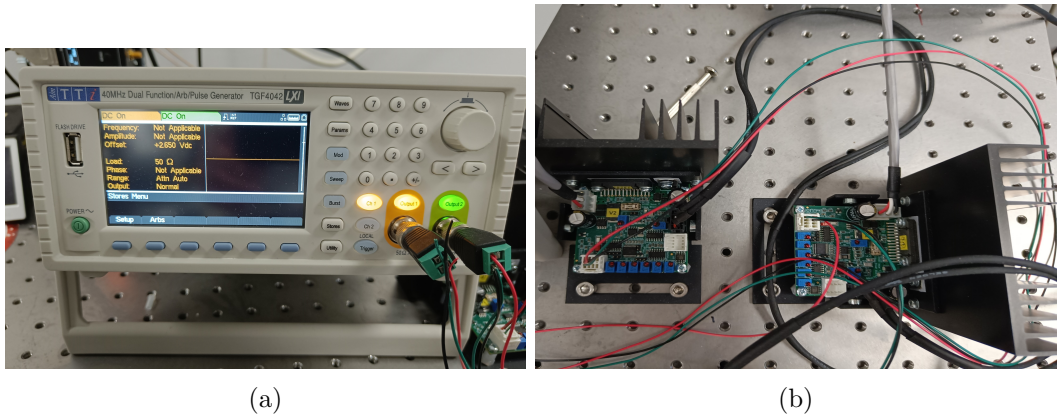


Figure 3.3: Signal generator galvano mirror controller, channel 1 controls the x-axis mirror, while channel 2 controls the y-axis mirror. Both channels can be manipulated independently.

For our applications a 4f correlator is utilised to ensure that the motion of the galvano-mirrors does not move the focal point of the laser, allowing for a stable trap

even while in motion. As shown in Fig. 3.1, after the galvano-mirror we have our two lenses - f_3 and f_4 - the former being installed 150 mm from the second mirror of the galvano, and the latter being installed 200 mm from the back focal plane of the trapping objective. The signal generator used was supplied by 'MCS Test Equipment Ltd', allowing for dual channel signal control. This allowed us to precisely control the alignment, amplitude, phase, and frequency of both mirrors making alignment much easier.

While in theory the frequency can be increased until the mechanical limit of the mirrors is reached ($\approx 1000\ Hz$), the practical upper limit is determined by the trap strength. For a silica sphere this is on the order of 300 Hz when suspended in water. Likewise while in theory the signal amplitude can be increased until the voltage limit of the motors is reached ($\approx 5.0V$) the geometry of the focal lenses limits the maximum amplitude to 0.5V as any greater will move the laser beyond the lens. For basic trapping calibration the galvano-mirrors were set to DC output, providing a fixed spot which operates like a typical optical trap.

3.2 Synthesis of Birefringent Micro spheres

There are several options for particles that can be rotated using optical tweezers [57], [102]. Over the course of the project two different micro spheres where investigated, Vaterite and liquid crystal droplets. Both can be readily synthesised in the lab and are will rotate at a variety of sizes (see 1.4.3).

Vaterite is a polymorph of calcium carbonate that is rarely seen in nature due to its low stability [107]. All three polymorphs are inherently birefringent meaning that they can be rotated using circularly polarised light. However unlike its other polymorphs of calcite and aragonite, when synthesised vaterite will typically form small spherical particles making them ideal for optical trapping and rotation. Synthesis of Vaterite micro spheres requires fine control of the crystal growth process in order to maintain polymorphic stability. Though for the purposes of optical rotation the exact polymorph is not as important as its morphology as all 3 polymorphs are inherently birefringent.

Vaterite samples where made by the first preparing equal amounts of $CaCl_2$ and

Na_2CO_3 at a concentration of $0.33M$, at the same time a vial of $0.33M$ $MgSO_4$ was prepared and set aside for later. First a small vial was filled with $1.5mL$ of $CaCl_2$ followed by $60\mu L$ and $90\mu L$ of $MgSO_4$ and $NaCO_3$ respectively, forming a seed solution. Next, a larger vial was filled with 5 mL , 1.5 mL , and 1 mL of $CaCl_2$, $MgSO_4$, and $NaCO_3$ respectively followed by the seed solution. After 10 minutes of slow but continuous mixing a few drops of Agepon was added to halt the reaction, the solution was filtered and washed 3 times with distilled water before being suspended in water.

When trapped in circularly polarised light, the anisotropic crystal lattice allows spin angular momentum to be transferred to the Vaterite particle, resulting in a rotation about the beam axis. Because the particle scatters light anisotropically the signal detected by the QPD shows periodic fluctuations [95]. In addition due to the change in polarisation there is also a periodic variation that appears at twice the rotational frequency [31]. Therefore, the resulting power spectrum is not a Lorentzian but now also displays peaks that appear at integer multiples of the particles rotational frequency.

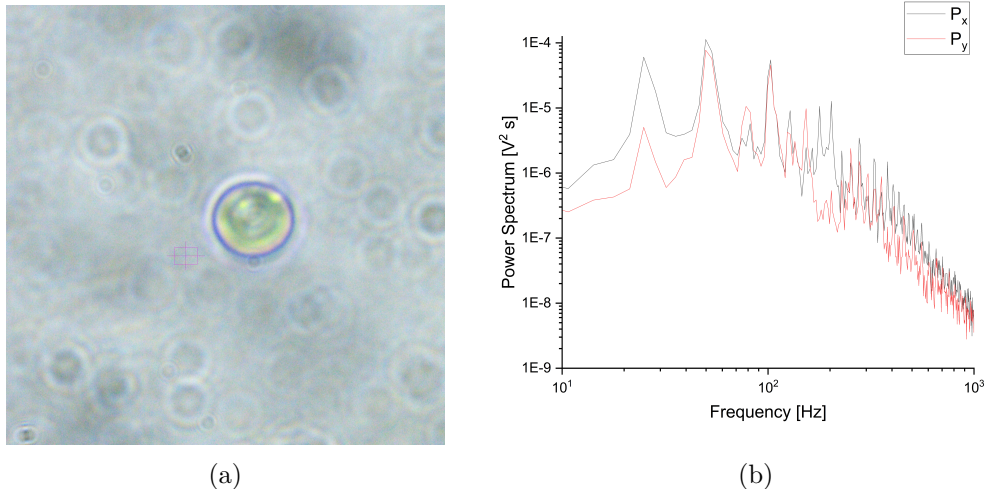


Figure 3.4: (a) Sample Vaterite sphere suspended in water and trapped by circular polarised trap. (b) Collected power spectrum from rotating Vaterite, peaks in the power spectrum appear at integer multiples of the rotational frequency ($f_{rot} \approx 49.8$ Hz)

As shown by Fig. 3.4(b) the power spectra produced still demonstrates a Lorentzian curve but modified with these periodic peaks, while the Lorentzian can be loosely fitted

to the end tail there exists no current model for describing the power spectra. The closest approximation to this was conducted by [95] where they describe the rotational motion of ellipsoidal polystyrene particles. The critical assumption being that the particle perfectly rotates in the $x - y$ plane. It has long been suspected that birefringent microspheres experience torques outside of the $x - y$ plane [108] making it very difficult to characterise the behaviour of rotating birefringent microspheres without a proper understanding of the full optical torque being applied to it.

3.2.1 Liquid Crystal Rotors

Liquid crystals are an intriguing example of materials with mixed phase properties. Unlike typical solutes such as Glycine, a liquid crystal can still maintain some degree of order between its individual molecules while in the liquid state. This is due to the fact that liquid crystals are constructed of ordered molecules that demonstrate a long range ordering. There are three main types of liquid crystal transition methods: Thermotropic crystals will transition to their liquid crystal phase when sufficiently heated. Lyotropic materials can undergo this transition due to changes in temperature and concentration. And lastly, Metallotropic materials - which are composed of both organic and inorganic molecules - change phase according to the ratio of organic to inorganic molecules present. Liquid crystal rotors are rather simple in their production, 4-Heptyl-4-biphenylcarbonitrile (7CB) was purchased from Sigma Aldrich and a small amount was added to a vial of distilled water. The solution was then heated in a water bath to 25° in order to transition the solid crystal into its liquid crystal state. The solution can then be loaded onto a sample cover slip and the individual droplets visualised. The molecules of 7CB will align with a strong electric field, and due to the spherical droplet geometry the droplets are inherently birefringent.

The liquid crystal droplets had a much faster rotation rate than comparable Vaterite spheres, due to their higher degree of birefringence and the fact that the droplets are far closer to perfect spheres making angular momentum transfer more efficient.

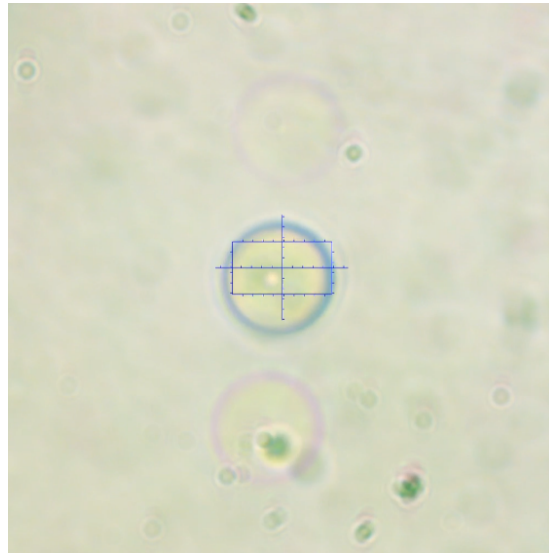


Figure 3.5: Liquid crystal undergoing rotation due to the circularly polarised trap.

3.3 Rotation of birefringent micro spheres

Optical tweezing has often been used for micro-rheology, by computing the exact forces being exerted on the trapped sphere, one can determine the local temperature/viscosity of the medium [59], [60]. When it comes to optical rotation, a rotating particle will experience a fluid drag torque that is proportional to its rotation rate, the maximum rotation rate is when the fluid drag is equal to the optical torque of the laser [60]. Optical rotors have been used to measure local temperature changes [59], or for understanding how fluid shear propagates through a medium [109]. Likewise, one can use a beam steering arrangement to probe the drag force of the fluid, by understanding the trap strength (calibrating using a low frequency signal) one can measure the drag force experienced by the local fluid [51]. I

For any discussion of fluid flow its important that we know the fluid regime which is given by the Reynolds number. For a sphere submersed in a moving fluid of velocity U this is given by:

$$Re = \frac{\rho U D}{\mu} \quad (3.2)$$

Where D is the sphere's diameter, and ρ and μ are the fluid's density and viscosity

respectively. In our case we do not have a fluid moving around a sphere but a sphere moving through the fluid at some velocity U , assuming a no-slip boundary condition we can model the fluid velocity profile based on the velocity of the particle. Assuming that for now the fluid properties are unaffected by the rotating particle we see that for an individual sphere the Reynolds number can only change due to increasing/decreasing the fluid velocity. The fluid velocity is directly proportional to the particles rotation rate for low Reynolds numbers [53]. Given the small size of the particles used ($1 - 10\mu m$ in diameter), and the relatively low rotation rates that are possible with an optical tweezer, for the case of our analysis the Reynolds number will not never be large enough to consider factors such as turbulence. There are two possible avenues for generating shear flow with a trapped particle; rotation of birefringent particles, and fluid flow induced by particle motion.

Rotating birefringent particles are the more common method for generating and measuring fluid flow in a solution. To see if we can even achieve the theoretical maximum shear rate, Vaterite spheres were synthesised (see Sec.3.2) submerged in water and trapped with the 1064 nm laser at set to 450 mW. The rotation frequency was determined using the QPD, and the particle sizes were computed by image analysis. With the particle size and rotation frequency, the tangential rotation speed is calculated via:

$$u(r) = \frac{\pi}{4} \frac{d^3}{r^2} \omega \quad (3.3)$$

Where d is the particle diameter, ω is the rotation frequency reported by the QPD, and r is the distance from the particle's centre. Using Eq.3.3 we calculated the fluid flow radiating outward from the centre of the sphere. The shear rate can then be computed as the partial derivative fluid flow (assuming shearing is generated purely by the flow field). This approach was used previously with liquid crystal rotors [102]:

$$\dot{\gamma}(r) = \left| \frac{\delta u(r)}{\delta r} \right| = \frac{\pi}{2} \frac{d^3}{r^3} \omega \quad (3.4)$$

One would expect that we set some reference distance where the fluid flow would be considered zero. However, at a microscopic level we are more concerned by the

fluid shear for an individual nucleation event. We are essentially computing what the shear rate would be for a small volume of fluid between two moving parallel plates. This is similar logic to Mura and Zaccone's work where they considered the shear on a subcritical nucleus in a flow field [66]. They go further in depth to discuss the impact of material transport, overall coming to the conclusion that increasing shear rate leads to an increase the nucleation rate up till some maximum.

3.3.1 Estimation of fluid flow around a rotating particle in bulk fluid

First we determined the upper rotation rate that could be achieved using both Vaterite and liquid crystal spheres. Vaterite samples were synthesised according to [50], [57] (see sec. 3.2), and then suspended in distilled water. A sample of $200 \mu L$ was pipetted and a single microsphere was captured via a circular polarised beam.

Due to Van der Waal's forces some of the microspheres were stuck together, fortunately individual sphere's were still present. Individual microspheres were trapped and their rotation rate was determined by looking at the peak frequency component of the collected power spectrum. Due to their anisotropic scattering the QPD signal will oscillate periodically. After taking the Fourier transform of the QPD signal the power spectrum has distinctive peaks at integer multiples of the rotational frequency. The largest peak is often twice the rotational frequency which is due to the polarization modulation of the scattered field, the first peak is due purely to the rotation of vaterite sphere [31]. An example of this behaviour is shown in fig. 3.6.

The accuracy of the rotational frequency is dependent on the sample rate of the QPD and the sample duration [91]. With higher sampling rates resulting in a wider frequency window (see Sec.??) and longer sampling durations resulting in more distinct rotational peaks. The default QPD sampling rate is $2^{17} Hz$ which is more than adequate for detecting even the slightest low frequency signals. And the default sampling duration was $3 s$ which for most cases gave us clear distinct peaks for even relatively low rotational frequencies. After trapping a vaterite microsphere the power spectrum was recorded and the rotation frequency was acquired. This was repeated several times for each sphere trapped, to confirm that the rotational frequency was constant and that

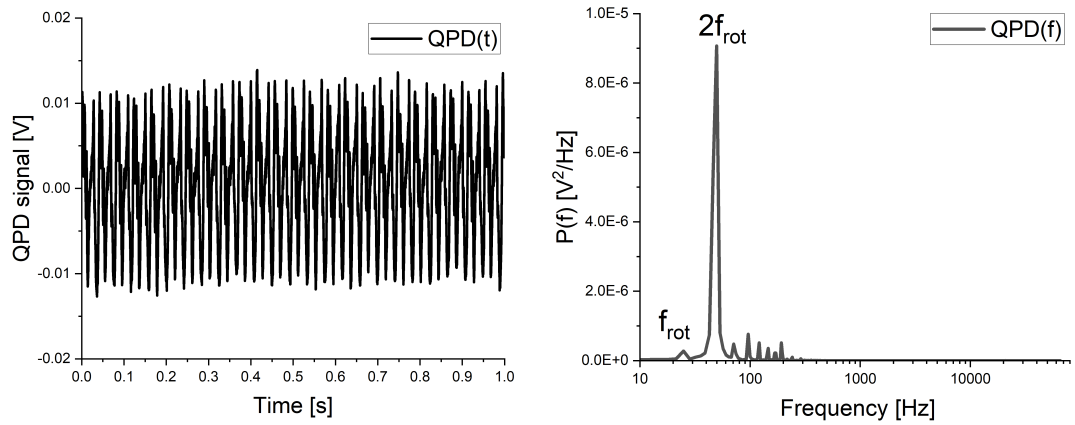


Figure 3.6: Example of QPD signal being converted from the time domain to the frequency domain. (left) Raw signal collected from the QPD over the 1st second of its trajectory showing a periodic spacing with a period of $1/f_{\text{rot}}$. (right) Power spectrum of the QPD signal, the y-axis is a linear scale to demonstrate the clear peaks in the power spectra. The rotational frequency is the first instance of a peak forming, and after that the peaks appear in integer multiples of f_{rot}

the sphere had reached its maximum rotation rate.

After computing the rotational frequency the radial fluid speed could be estimated using Eq. (3.3). From there we can estimate the shear flow experienced by a small volume of fluid within the flow field (see Eq.(3.4)). Here we only consider the fluid flow as it propagates outward from the axis of rotation. While the cover slip will have some effect fluid flow it is difficult to quantify the effects of a hard boundary on a rotating object when the boundary is perpendicular to the axis of rotation.

From Fig.3.7 there is not a strong relationship between particle size and rotation rate, this is contrary to much of the theoretical predictions that predict an exponential decay with particle size. This can be in part due to the fact that synthesising perfectly spherical spheres that have uniform birefringence across the whole population is difficult. Despite our best efforts at controlling the growth rate the smallest particle ever synthesised was around $3 \mu\text{m}$ in diameter. The Vaterite spheres would often stick together while suspended in water after a short period of time. The fastest reported rotation rate within a fluid was by [58] that achieved a rotation rate of 5 kHz , this is plotted in Fig 3.7. In addition we added the results from [57] as a more realistic example.

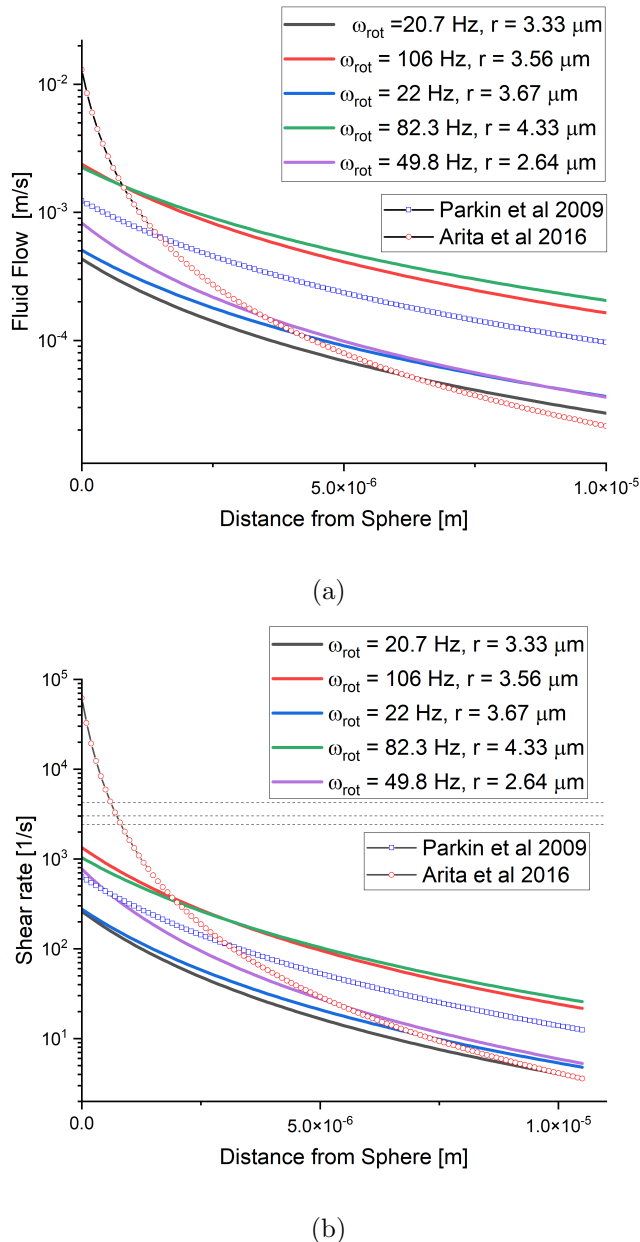


Figure 3.7: (Top) Fluid flow radiating out from the surface of a rotating Vaterite sphere. (Bottom) Shear rates computed using Eq.3.4, optimal shear rate is of 3000 s^{-1} is indicated by the dotted line. Vaterite radii and rotation frequencies are shown, the laser power was kept constant at 450 mW. Reported rotation rates, and their corresponding fluid flow and shear rates, for Vaterite are also plotted alongside lab results. Results from [57], [58] are included as well.

The optimal shear rate predicted by [67] is plotted on Fig. 3.7(b), the outer dotted lines represent the point when the nucleation rate is less than 90% of the maximum. We can visualise the fluid around the rotating sphere by dividing it up into radial sections. Assuming the sphere is rotating sufficiently quickly there are three sections of concern, as demonstrated by fig. 3.8. The fluid close to the sphere experiences a shear rate that is far greater than the optimal shear rate, in which case nucleation is suppressed [66]. Secondly, there is a region of fluid that experiences a shear rate close to the optimal value ($\pm 5\%$) where the nucleation rate is enhanced significantly compared to the bulk fluid. Lastly, beyond the optimal region the shear rate drops off exponentially in which case the nucleation rate is barely different compared to the bulk fluid.

3.4 Rotating spheres in Supersaturated solution

If rotation rates in bulk solution are insufficient then a rotating sphere close to an artificial barrier may be able to improve the shear rate of the surrounding fluid. Of course placing a solid barrier in a supersaturated fluid may well encourage nucleation somewhere on the surface outside of our control. Instead we chose to use the droplet edge of the supersaturated solution, while not a hard barrier per say, the molecular mobility close to the droplet edge is reduced due to surface tension. Furthermore, it has been shown through multiple results that nucleation is enhanced at the air-solution interface [24], [46], [110].

Estimating the distance from the trap focus to the cover slip is difficult to measure directly, often requiring one fits a complex Lorentzian curve to the recorded power spectra in order to measure the fluid drag from being in close proximity to the cover slip [91]. We estimate that the vaterite must be at least $15 - 20 \mu m$ from the cover slip for us to reliably trap them. The contact angle between the cover slip and solution was previously measured in [111], while being loosely dependent on the supersaturation the measured contact angle for supersaturated solutions was between 30° and 35° . This is shown in fig.3.9.

Supersaturated solutions of glycine and water were prepared and stored in an in-

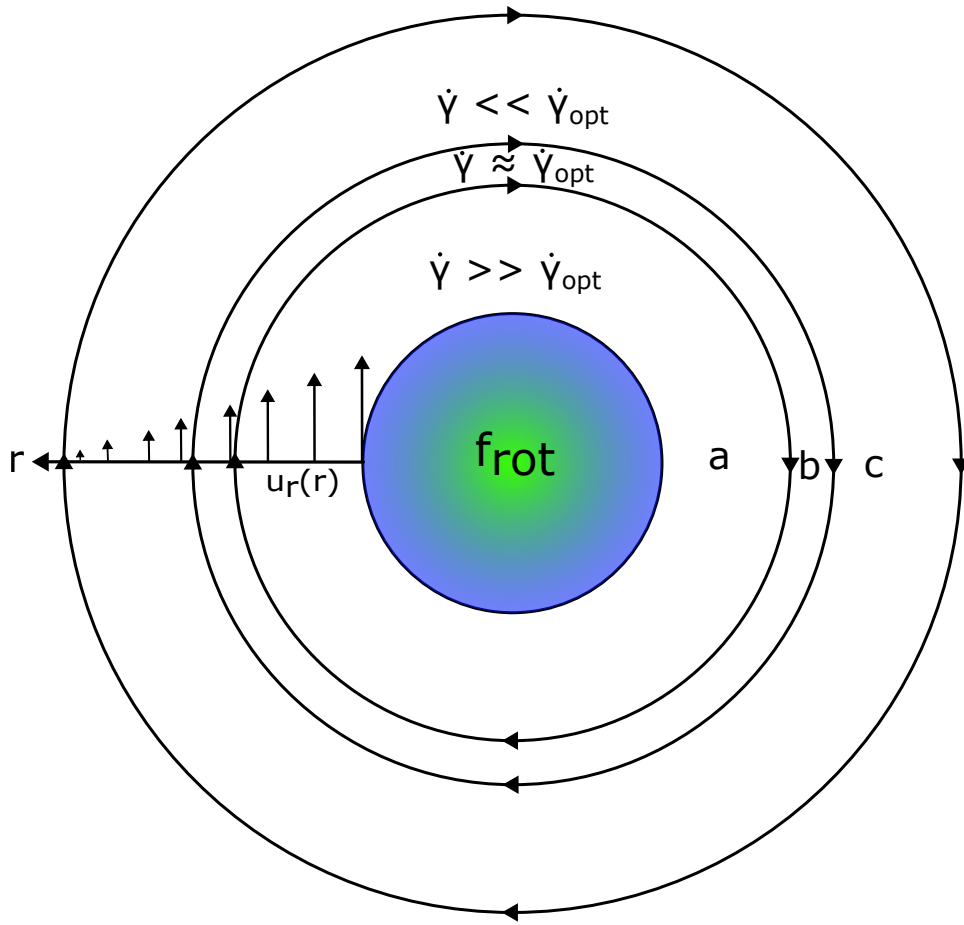


Figure 3.8: Diagram demonstrating how fluid shear rate varies radially from a rotating sphere (rotation rate = f_{rot}). (a) the shear rate exceeds the optimal shear rate ($\dot{\gamma}_{opt}$) and suppresses the nucleation rate. (b) shear rate is close to the optimal amount, enhancing the nucleation rate. (c) shear rate is far below the optimal amount and the nucleation rate is comparable to the bulk fluid.

cubator at $40^{\circ}C$ prior to use. When ready to be studied $15 \mu L$ of vaterite suspension was pipetted into the solution and $20 \mu L$ of the combined solution was pipetted onto the cover slip. A Vaterite sphere was located, trapped, and moved to the droplet edge where the solution meets the cover slip. This removed the need for hydrophilic coatings to achieve a flat fluid layer (as used by [24], [112]).

Particle sizing was achieved by converting the particle diameter from pixels to physical units within an accuracy of $\pm 0.05 \mu m$. The QPD was used to measure the frequency of fluctuations in the QPD signal. After measuring the rotational frequency the sphere

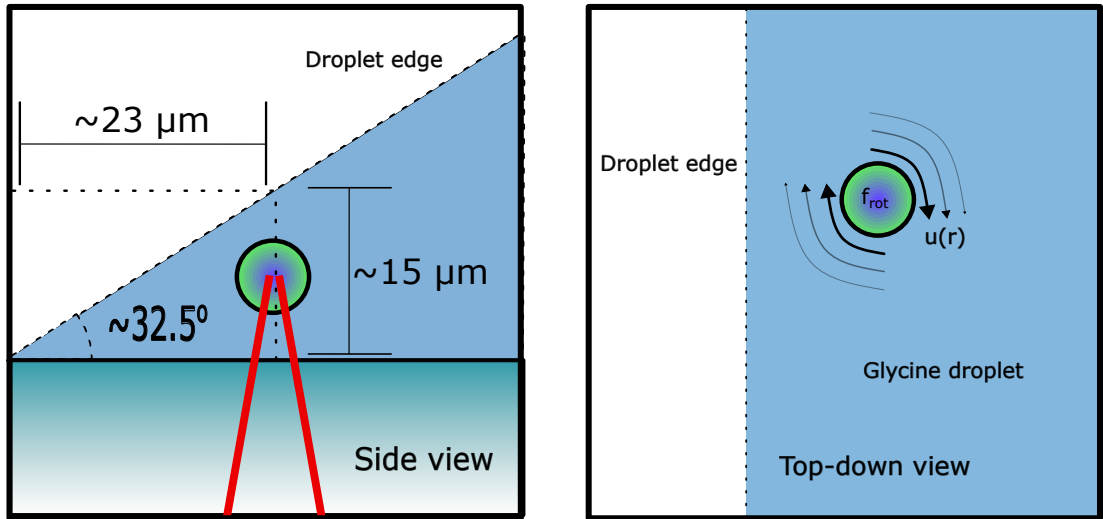


Figure 3.9: Diagram of optical trapping set up for rotating birefringent particles in a supersaturated solution. Left: side view of the trapping set up showing the location of the trap focus at the edge of the droplet of a supersaturated solution. The approximate contact angle (calculated by [111]) is used to provide a scale of how close a trapped particle could be located. Right: top down view of the glycine droplet with a trapped birefringent particle shown close to edge of the trap. As the particle rotates the drag force from the surrounding fluid generates a flow field around itself (see Eq. 3.3).

was left to rotate for a period of ten minutes after which, if no nucleation event was observed the particle was released. The overall results are catalogued in table 3.1.

It should be noted that rotational frequencies equal to 0.00 Hz are not due to a rounding error. Simply looking at the live video shows no rotation of the vaterite particles, and even looking at the QPD signals shows no discernable fluctuations that would arise due to rotation. Trying to trap a particle close to the edge proved more challenging than expected. Unlike in previous reports where the beam is focused at the upper edge of the droplet [24], [46], [113], we attempted trapping in close to the contact point of the droplet and the cover slip.

It is suspected that trapping is much harder at the interface due to increased surface tension and unpredictable scattering forces. The closest we could trap a microsphere to the droplet edge was in the range of $5 - 10 \mu m$, at that distance the fluid flow is so low that even the presence of a hard boundary would be insufficient for shearing the fluid. Furthermore, as is evident in Table 3.1, the rotation rate drops off significantly with

Table 3.1: Results from rotating Vaterite within supersaturated solution of H_2O and Glycine. Solubility concentration for Glycine at 16° was $C^* = 0.2016g/g$

Super Saturation	Particle radius [μm]	ω [Hz]	Nucleation [\checkmark/\times]
1.01	2.34	10.4	\times
	3.26	8.46	\times
	5.67	9.63	\times
1.14	1.89	1.23	\times
	3.75	3.54	\times
	4.35	4.86	\times
1.4	1.59	0.00	\times
	3.47	0.00	\times
	6.24	0.00	\times
1.45	3.68	0.00	\times
	5.43	0.00	\times
	6.32	0.00	\times
1.49	1.52	0.00	\times
	4.76	0.00	\times
	7.27	0.00	\times

increased supersaturation, due to higher fluid viscosities. While in theory a sufficiently focused laser could rotate any microsphere to a fast enough to reach the shear rate predicted by [67] the localised intensity would be so large that even using D_2O would see a significant increase in temperature.

It is not impossible that fluid shearing could be used in the future to localise nucleation; but from these results, using individual micro-rotors is not an appropriate method due to two key factors. Firstly, the area of influence is far too small to see any noticeable increase in the nucleation rate this is demonstrated most clearly in fig. 3.7. Due to the exponential decay in the expected shear rate it is very difficult trying to shear a large volume of fluid. Even if the optimal shear rate at a micro-level was an order of magnitude less than what was predicted by [67], only a small volume of fluid would even experience that shear rate. In order to properly understand the microscopic effects of fluid shear a method of localised shearing over a larger fluid volume is necessary.

Secondly, increased fluid viscosity significantly reduces the limits the maximum rotation rate possible. As indicated by 3.1, the rotation rate achievable by a vaterite sphere falls off significantly with increasing supersaturation. Experimental estimations

of relative viscosities showed a 12% increase when looking at undersaturated glycine solutions ($S \approx 0.34$) [114]. As far as we are aware there are no reported fluid viscosities for higher supersaturations. Extrapolating the results from [114] suggests that a saturated solution would have a 35% increase in fluid viscosity (compared to pure water). This also does not account for any other factors such as the fact that close to a boundary a rotating particle will experience a reaction torque from the stationary surface [53].

If multiple micro-rotors could be trapped in close proximity to one another they could create a large region of fluid where nucleation is more likely than the bulk fluid. Because optical torque is not contingent on the fluid properties the only limiting factor would be the total angular momentum transferred to each particle. Micro-rotors have been created that allow for precise control of suspended micro-particles [115] and could potentially be used to generate sufficient shearing. However these could not be used in this project as we lacked the necessary hardware to form multiple gradient traps.

3.5 Nucleation with a Stationary and Moving Beam

As mentioned previously, shearing via optical rotation did not result in any localised nucleation events even while in the proximity of the droplet edge. An alternative approach was suggested, using a galvano mirror to move a particle quickly through a supersaturated solution. Preliminary calculations suggested a particle moving rapidly through a fluid could produce significantly greater shear rates (see *Appendix X.X* for breakdown) than a rotating particle. While a particle is within the optical trap the gradient forces are significantly reduced meaning simply trapping a particle is insufficient for inducing nucleation [111]. This is why we did not see any nucleation events while rotating the vaterite, there is not a large gradient force to draw in material.

During initial testing using silica beads we found that even in undersaturated solutions the optical trap would produce a crystal nucleus when the trap was empty. This has been reported prior [24], [112], but what is more interesting is how the beam's motion influenced the growth of the nucleus.

3.5.0.1 Choice of Crystal growth rate units

The growth rate of a crystal can be described using different units depending on the situation. For example, seed crystals often use growth units in the form of *length per unit time*. This can either be used to describe the overall length of the longest edge of a crystal, or to describe how individual faces grow separately. This works well for crystals with a clear morphology, in regards to laser induced nucleation the crystal growth is heavily influenced by the local fluid conditions meaning tracking the length of an individual face is challenging. Instead we utilise image analysis software such as imageJ to measure the area of the crystal after each frame to get a rough estimate of the crystal growth rate in units of *length² per unit time*. With the addition of the contact angle information from [111] we can approximate the crystal height based on how close it is to the droplet edge.

3.5.1 Stationary beam

Its well known that a supersaturated solution can nucleate if irradiated by a focused beam with sufficient power [112]. First we look at how a laser induced nucleation event unfolds using a stationary focused beam. The laser was focused at the edge of a $20\mu L$ droplet consisting of water and dissolved glycine ($S = 1.03$). The solution was monitored for 10 minutes, if a nucleation event was observed the event was recorded using a high speed CCD. If no nucleation event was observed after 10 minutes the solution was disposed of and a new sample was prepared. After ten repeats only 30% of the samples observed a nucleation event at the focus. All of which displayed similar growth behaviour to one another.

Consider Fig. 3.10, the frames taken from a nucleation event, the beam is a stationary being $\approx 3.5\mu m$ from the droplet edge. After a period of roughly 5 minutes a nucleus forms at the trap focus, growing quickly (growth rate was approximated using imageJ to be on the order of $700 \mu m^2/min$) from the focal point of the trap until after roughly 6 seconds the crystal escapes. A likely reason that the trap is escaped is due to the fact that crystal is far too large to be held in place and is in fact still growing as the solution is supersaturated. Based on the contact angle measurements from [111],

Chapter 3. Effects of localised shearing on crystal growth and nucleation

the droplet height could not have been any more than $2 - 5\mu\text{m}$ at the trap focus.

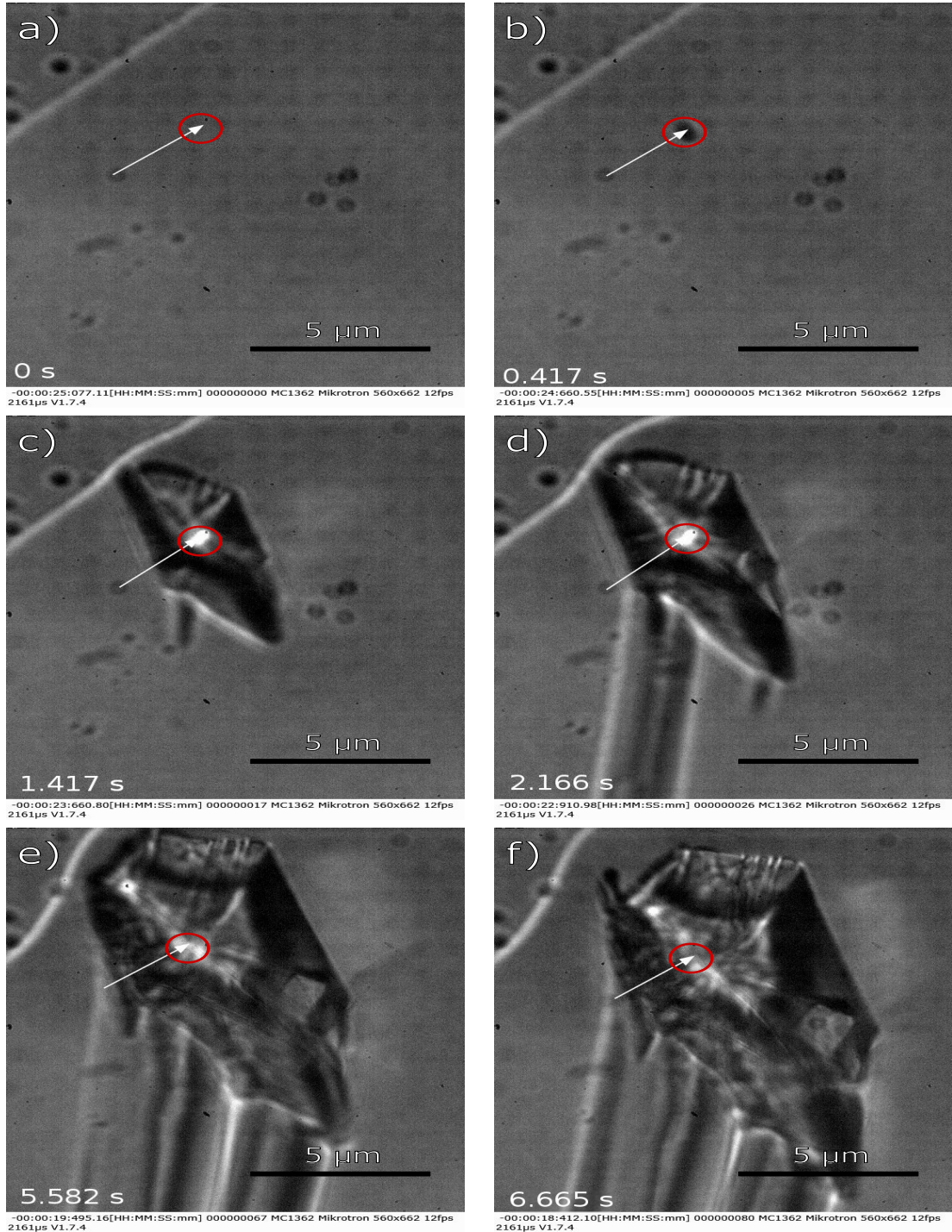


Figure 3.10: Laser induced nucleation at the edge of a droplet of supersaturated glycine solution. (b) shows the first instance of a crystal nucleus, growing quickly through (c)-(e) until after 6.665 s the crystal begins to escape the trap.

Comparing to previous literature using optical tweezers shows that the growth rate is only loosely connected to the solutions supersaturation. Crystal growth rates for a solution of glycine and water ($S \approx 1.00$) was found to vary from as much as $3900\mu m^2/min$ to as low as $675\mu m^2/min$ [111]. The reason for such high crystal growth rates is due primarily to the tweezer focus bringing in material due to gradient forces. A study of glycine crystals in water found that for a similarly supersaturated solution the growth rate along the 011 face was around $0.1 \mu m/min$ where as the 010 face was found to have a growth rate of around $0.01 \mu m/min$. While its difficult to extrapolate an exact area growth rate from these results we can approximate that if the we looked directly perpendicular to the crystal growth the area would increase at $\approx 0.02 \mu^2/min$ (see X.X for a breakdown of this approximation).

The key take away to remember is that the beam has no influence over the crystal shape, instead it grows outward from the trap focus. Furthermore, due to the fact that the solution is supersaturated the crystal growth cannot be contained to the trap focus. Instead the crystal escapes as its size exceeds the trap focus.

3.5.2 Moving Beam

To test if a rapidly moving silica bead could generate the necessary shear rate for crystal nucleation we wanted to see if a trapped silica bead could be trapped and moved in an aqueous solution. $20 \mu L$ of glycine and water ($S = 1.03$) was added to $10 \mu L$ of a dilute water-silica mixture making the solution unsaturated ($S \approx 0.7$). However, due to the beam's motion we instead encountered unexpected growth behaviour.

Shown below in Fig. 3.11 where we have the laser focus moving in a small elliptical pattern. While nothing is seen directly entering the focus a nucleus forms close to the droplet edge, unlike in fig. 3.10 the crystal does not grow out from the focal point evenly. Due to the galvano mirror, the crystal is simultaneously being moved by and growing around the focal point of the trap. Because of this the crystal nucleus lacks a clear morphology at first. Until roughly $20 s$ the crystal reaches a almost prismatic structure, with further irradiation increasing the size.

Interestingly the galvano-mirror allows the trap to impart a slight torque on the

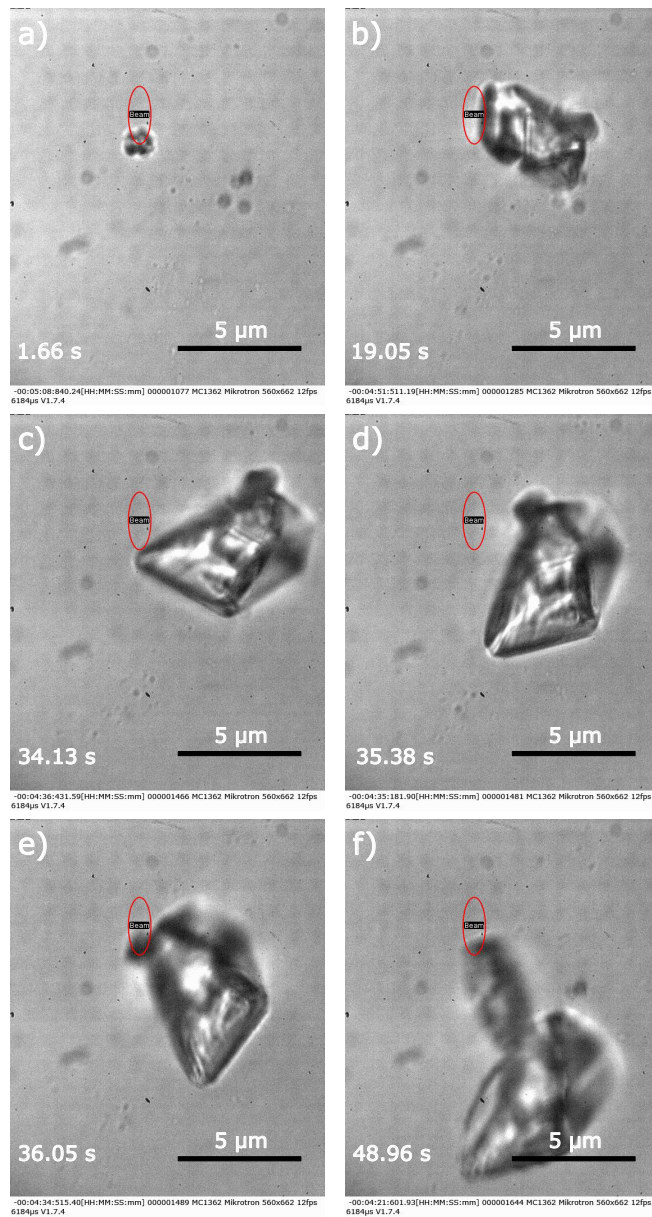


Figure 3.11: Frames from a longer video depicting the growth of a nucleus using a moving beam. Beam power is kept at 700 mW and the supersaturation was estimated at $S=0.86$. Initially the crystal shape is amorphous (a) but eventually reaches a more regular shape (b). This crystal is still influenced by the optical trap as even when not directly irradiated by the laser the crystal rotates between (c) and (d). When the laser is focused on a corner the crystal growth is localised to that region, resulting in an elongated section forming between frames (e) and (f).

crystal, as shown in fig. 3.11(c) and (d), where even though the crystal is not directly in the trap focus it rotates in the $x - y$ plane and gets trapped again at a corner. The rotation could not be due to fluid flow close to the surface of the crystal as the dipole moment of individual water molecules is too small to be influenced by an optical trap. In figs.3.11(e) and (f), the crystal growth becomes localised to the corner. The area growth rate between figures 3.11 (a) and (d) was approximated using imageJ at $45.03 \mu\text{m}^2/\text{min}$, where as between figures 3.11(e) and (f) the growth rate at that particular edge was estimated at $42.10 \mu\text{m}^2/\text{min}$.

Nucleation in undersaturated conditions has been reported previously in D_2O [112] and H_2O [111], though not involving a moving beam. This modification allows for the crystal growth to be localised to a specific region of the bulk crystal whereas with a stationary beam there is no control over the crystal morphology. In fact this allows for a much finer control over the exact shape of the crystal nucleus, in some cases allowing for growth out of the viewing plane as shown in fig. 3.12.

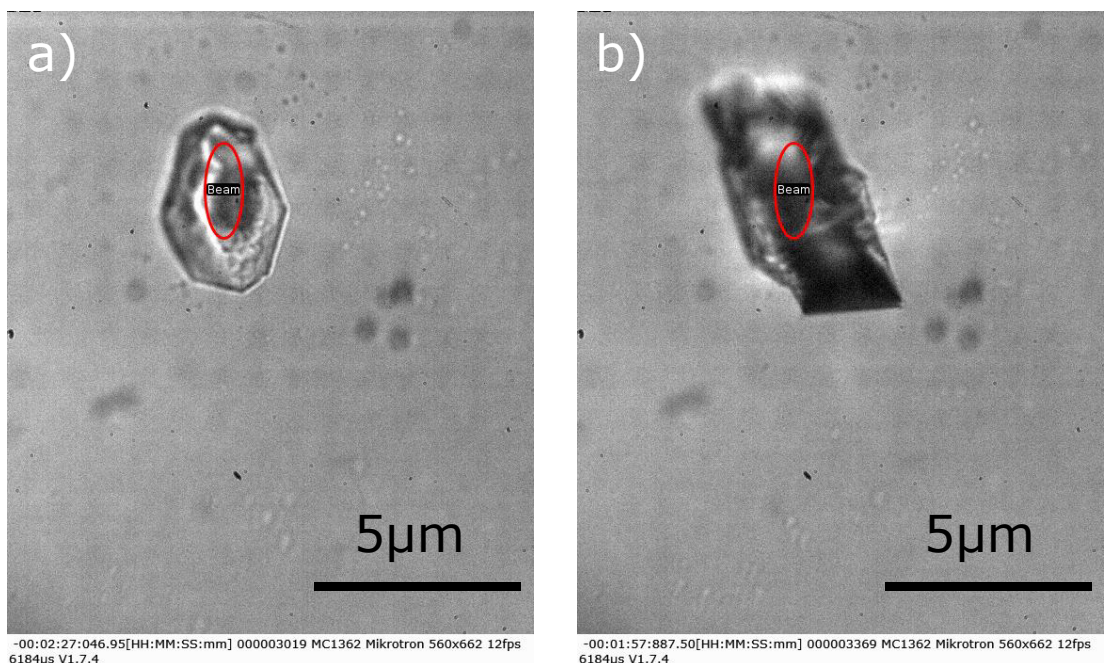


Figure 3.12: Interesting crystal growth on the surface of an existing crystal. Initially the crystal surface seems flat (a) but eventually a different crystal structure grows out off of the surface (b).

Where a large outgrowth forms on the surface of a nucleus, over a period of 30 s

the outgrowth develops into a rhombic crystal structure. The unique crystal growth demonstrated is likely a factor of the moving beam focus, but this raises a question over how the laser can localise the growth only around the focus and why the crystal does not grow or shrink when not directly within the trap. There should be some material that is being drawn into the trap as it scans across the camera frame.

3.5.3 Direct trapping of Glycine clusters

In a repeat experiment a solution similar to sec. 3.5.1 was made up, but without any silica micro-spheres. Once again the beam was focused close to the droplet edge, this time the galvano mirror was scanning a circular path (as shown in fig. 3.13). After a few minutes of irradiation droplets were seen entering the camera frame. Because no silica had been added, and that the solutions were filtered, these droplets had to be from the glycine solution. Trapping individual droplets did not result in immediate nucleation even after several minutes being trapped. Trying to bring two droplets together resulted in nucleation between the two droplets, compared to 3.5.1 & 3.5.2 the growth is much slower, taking nearly 40 seconds before the crystal structure becomes clearer.

The fact that these droplets can be trapped indicates they must have a higher refractive index than the surrounding solution. Previous reports have shown that a focused trap will draw in solute material from the bulk [45], [48]. This suggests that the droplets observed are concentrated spheres of glycine, which also explains how nucleation was initiated when those two spheres were brought into contact with one another. The droplets must be providing material for the crystal growth. It has been shown that the concentration of glycine solution is correlated with the refractive indices of the liquid [48], [116]. This suggests that we could measure the concentration of individual droplets based on the trapping strength of each droplet.

3.5.4 Influence of a moving beam front on seed crystals

One potential application of this phenomena would be in using a moving the moving beam front as a method for shaping the final crystal morphology. Therefore, we wanted to test if a moving beam front could have any influence on the shape of a seed crystal submerged in a bulk solution. Glycine seed crystals were grown via evaporative crystallisation over night. The resultant crystals were as wide as 0.5mm in some cases. Individual crystals were collected and suspended in a water + glycine solution ($S = 1.001$) and the laser was scanned along a narrow linear path. It should be noted that the seed crystal was fully submerged in the solution, meaning that there is no interface between the air and solution close to the seed. Five separate repeats were conducted, all demonstrating similar behaviour to one another.

As shown by fig. 3.14 the laser does not in fact promote crystal growth but instead forces the crystal to dissolve into the bulk solution. The dissolution rate is not as substantial as the growth rate seen in previous sections. It takes over 20 minutes for the for the crystal surface to dissolve more than a few microns. Furthermore we do not report any sightings of droplets close to the surface of the crystal nor do we see anything enter the optical trap.

This has some implications: Firstly, the lack of supposed glycine droplets suggests that the presence of an interface is crucial in order to promote the formation of these droplets. This is consistent with previous reports on laser nucleation, where a air-solution or solution-glass interface is necessary for the trap focus to have any noticeable effect on the solute [24], [48], [112]. Secondly, the fact that the seed crystal dissolved in a saturated solution suggests that this could be due to a localised heating effect. A commonly used heating model for optical tweezers is the Peterman model [117] which accounts for the lateral distance between the optical trap and a local heat sink (such as the glass cover slip or microscope objective). Even with the heat sink the predicted temperature rise in pure water would be around $5 - 10\text{K}$. The fact that the seed crystal dissolves so slowly could simply be due to the fact that the local heating is lessened by the moving beam front.

3.6 Summary of Moving Beam Phenomena

To summarise, the introduction of a moving beam helps to accelerate the local growth of a newly formed crystal. It seems that this phenomena will only occur when close to interface between the solution and air. We note the presence of droplets that can sometimes be seen entering the trap, though this is not always necessary for a nucleation event to occur. A plausible description of the phenomena is described thusly.

Initial nucleation is similar to typical optical trapping induced nucleation, with the air solution interface limiting the molecular mobility of the solute molecules [24], [48], [110]. The moving beam front can influence the motion of the nucleus initially, but eventually the drag force means the crystal is not moved by the optical trap. Localised crystal growth occurs when the trap is close to or partially over the interface of the crystal (see fig. 3.15(a)). This suggests that the laser itself is bringing in new solute material that can then adhere to the crystal surface. Interestingly even when the crystal growth is localised to a small section of the crystal we do not observe the crystal dissolving. This is consistent with other observed laser induced nucleation results, where as long as the laser is active the crystal remains stable within the solution [24], [110]–[112]. It does raise further questions however, mainly in an undersaturated solution is a moving beam front able to increase the size of the formed nucleus compared to a stationary beam? Additionally, it raises the question about what the role the ‘glycine droplets’ play in the nucleation process.

As shown in 3.5.3, the optical trap can manipulate these droplets similar to micro-spheres. When in close proximity to the trap these droplets are brought towards the crystal surface (see fig. 3.15(b)). We have already suggested that these droplets must contain glycine as they are to large to be a silica microsphere, and the solutions were filtered prior to being studied. The droplets provide material that grows the crystal around that region (see fig. 3.15(c)). Eventually the local solution is either depleted of solute material or the crystal front has grown to fully encompass the trap, preventing further growth (see fig. 3.15(d)).

What remains unclear is why the solution interface is necessary for localised crystal

growth. We know that the glycine droplets will form when the laser is close to the glass-solution interface [46]–[48]. This is consistent with our results as being able to image the droplet edge requires that the laser is brought close to the cover slip. However it is not clear how exactly these droplets contribute to localised crystal growth as in sec. 3.5.2 no droplets are seen entering the trap. It seems likely that the presence of droplets is necessary as we see that the seed crystals dissolve while there are no droplets present.

There are still several factors that need to be investigated. Firstly, there is the question of what conditions result in the production of concentrated droplets, it is not clear if the presence of a laser is required or if these droplets naturally occurring. Prior literature would suggest that the laser is required [24], [45], but this would not explain why in many cases the droplets are found far outside the influence of the optical trap. It has been shown that phase separation occurs when a trap is focused close to the cover slip [46]–[48], but there has been no cases of nucleation occurring at the cover slip. Furthermore these experiments all occurred in supersaturated condition ($S \geq 1.50$) with a much wider focus ($NA \leq 1.00$) whereas our results occurred in undersaturated conditions with a tighter focus. We did not not any occurrence of a phase separation as reported by [46]–[48] and yet we see the appearance of droplets that we surmise are partially constructed of glycine.

Secondly, there is the question of how these droplets supply material to the bulk crystal. In some instances it is clear that the droplets are being drawn into the trap, however, in other instances while there are no droplets close to the vicinity of the optical trap the crystal continues to grow. If these droplets are a necessary precursor to induce crystal nucleation then understanding how they provide materials to the bulk crystal may help with our understanding of the kinetics of multi-step nucleation.

3.7 Conclusion

In conclusion, the experimental results from this chapter provide no affirmative evidence of shear induced crystal nucleation. This is in part due to the limited rotational speed that could be achieved using vaterite microspheres. Simply adding a micro-rotor

Chapter 3. Effects of localised shearing on crystal growth and nucleation

to a supersaturated solution will not yield a significant fluid flow to induce crystal nucleation. Furthermore, the region in which the local shear rate is significant enough is so small that any nucleation events that could occur there may not grow large enough to be stable. This does not however, suggest that shear induced nucleation is impossible at a micro scale. In fact there have been several developments lately that allow for the precise rotation of multiple rotors to control the precise motion of silica beads [115]. This would allow for direct control of the shear rate within a given volume of fluid, allowing one to study the impact of fluid flow on a nucleus at a micro-scale.

On the other hand, the results utilising the galvano mirror have some interesting implications for future research into crystal nucleation using optical tweezers. We noted that a moving beam front is capable of localising the crystal growth around the beam focus in undersaturated conditions. Typically in laser induced nucleation the final crystal morphology is influenced primarily by the local fluid conditions [24], [111]. If this phenomena could be fully understood we could have a means of directly manipulating the morphology of any nucleating crystal. We noted that in undersaturated conditions the presence of droplets that could be trapped and later nucleated when brought into contact with one another. There remains some uncertainty over the role these droplets play in a nucleation event. Further research is also necessary to understand how the fluid and laser parameters (i.e. supersaturation and numerical aperture) impact the formation of these droplets. The fact that these droplets could be trapped suggests they have a higher refractive index to the solution, given that the solutions were filtered prior to irradiation dismisses that they could be dust particles. Prior literature suggests that optical trapping of a supersaturated solution can lead to the production of nano droplets [45], [48].

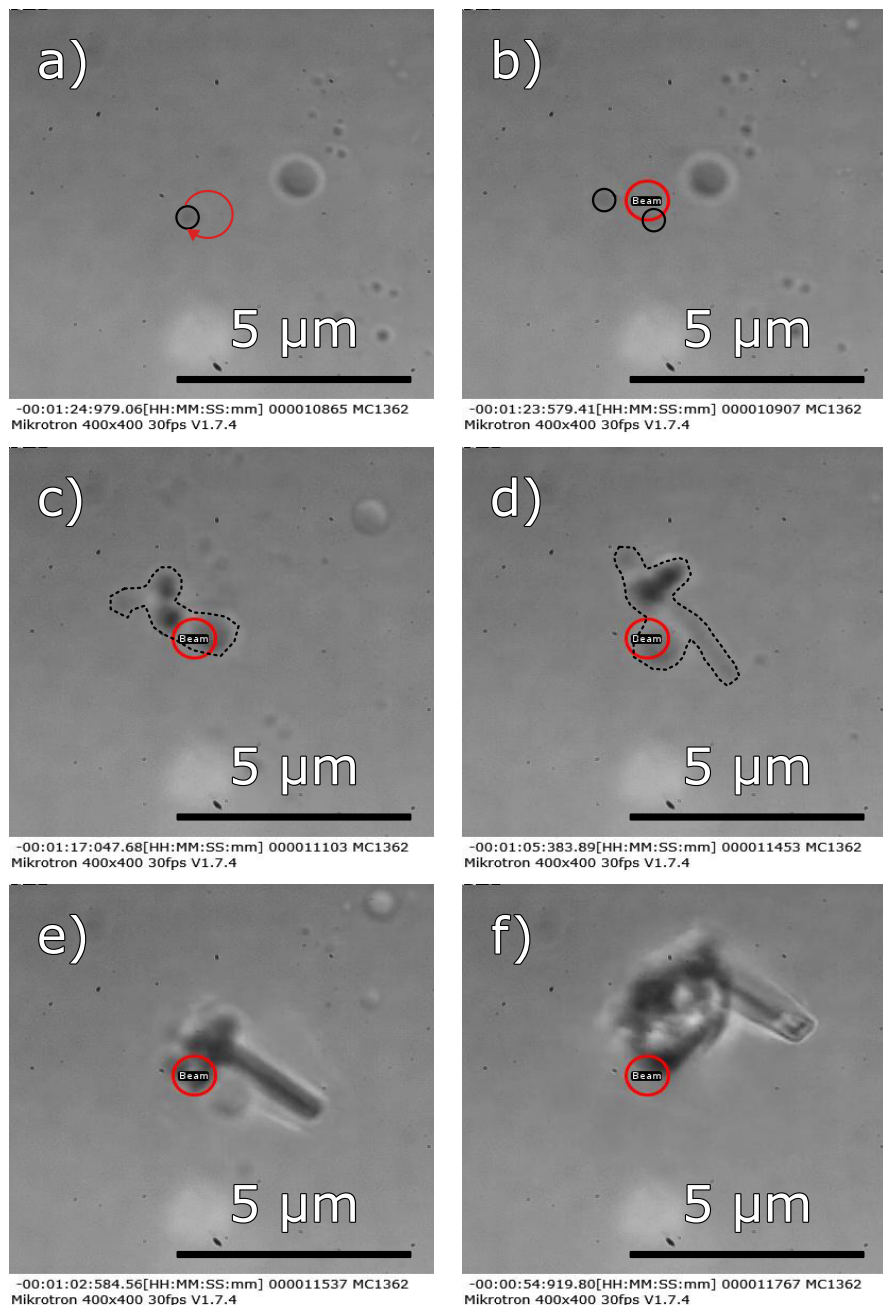


Figure 3.13: Frames from a longer video demonstrating the trapping of a glycine droplet. Solution is undersaturated glycine and water ($S = 0.86$), with the laser power set at 750 mW. (a) shows a trapped droplet (outlined in black) being brought into contact with a larger droplet. (b) upon contact a nucleus can be seen between the two droplets. The growth is rather slow with the crystal having no clear defined morphology through (c) and (d). Between frames (e) and (f) the larger droplet finally joins the main crystal.

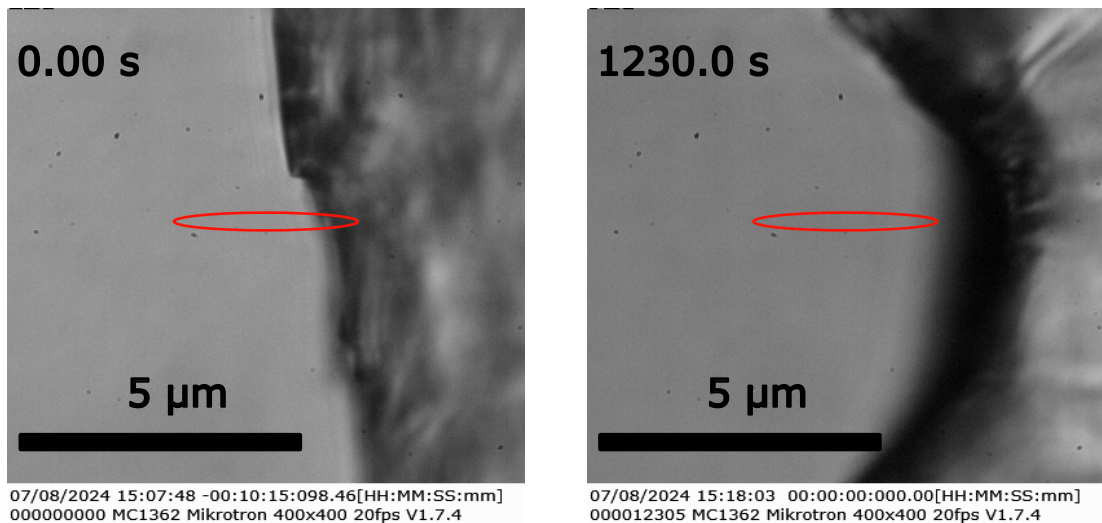


Figure 3.14: Frames from a seed crystal being irradiated by a scanning laser. The laser path is shown below in red. Initially the crystal edge is nearly perpendicular to the laser path. Over the course of nearly twenty minutes the crystal around the laser has dissolved leaving a concave indent.

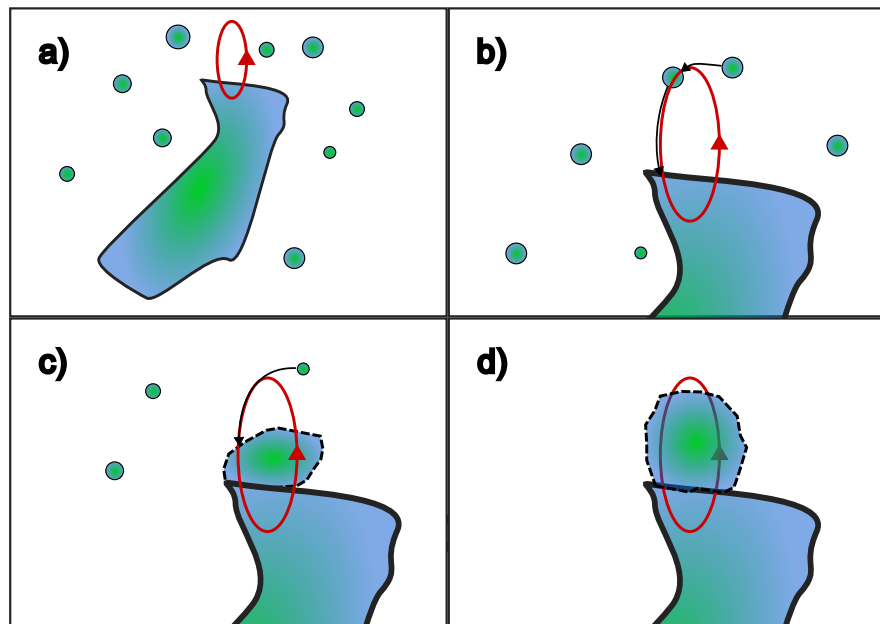


Figure 3.15: Diagram outlining how a moving beam assists in the growth of a crystal nucleus. (a) a crystal nucleus is partially trapped by a moving beam with solute droplets close to its surface. (b) droplets close to the laser focus can be drawn in by gradient forces and moved towards the crystal surface. (c) the laser brings in material that is then deposited on the surface of the crystal. (d) eventually the crystal area either fully surrounds the laser focus or the solution surrounding the laser is depleted of solute material.

Chapter 4

Complex Langevin dynamics of spherical dimers

Much of the calibration theory discussed in Chapter 2 assumes that the target particle in question is a single sphere, one whose scattering and motion is easily computed. However, while working with dense colloidal suspensions, one often ends up trapping more than one sphere. Li and Arlt [96] studied the case of two microspheres trapped in a single OT and found that multiple trapped beads could be mistaken for a single trapped bead with altered trap stiffness (see 2.1.0.1). Theoretical studies on the case of two trapped microspheres by Xu *et al.* [118] employed a ray-optics based model to show that the two trapped beads are brought into physical contact with each other by optical forces and they also calculated the axial equilibrium positions of the two trapped beads as a function of their size. Experiments in [119] confirmed that the two trapped beads indeed experience different trap stiffnesses in the vicinity of the same potential well.

There are further discussions looking into the dynamics of a whole host of asymmetrically shaped particles [120]–[122], their results all showing that predicting the behaviour an arbitrary shaped particle comes with great difficulty due to the fact that the optical force is dependent on a greater number of variables such as orientation and size factors.

With the initial goal of the project being to induce nucleation events via a rotating

sphere, the aim of this chapter is to - in a limited capacity simulate and investigate the influence of a second particle being bound to our target sphere. The choice of a dimer, instead of an amorphous solid that might better represent a growing crystalline solid, allows us to consider how the dynamics of the aggregate change by varying a single parameter, namely the size ratio of the two spheres. Additionally, attempting to simulate an amorphous aggregate is rather difficult as calculating the optical force and torque is computationally slow. We build upon the works of Vigilante *et al* [93] to consider asymmetric spherical dimers and how varying size parameters alters the dynamics and additionally makes characterising their interactions within an optical trap more cumbersome.

In this chapter we will consider how the addition of a second sphere changes the trapping dynamics by introducing multiple equilibrium positions. These positions are dependent on both the size ratio of the dimer and its orientation relative to the trap. This is important to address, for while the the dimers' diffusive behaviour is the same, regardless of position and orientation, how it interacts with the trap may produce the wildly different results. Furthermore, we look at how our dimers interact with circularly polarised light, this is especially pertinent as the original plan was to utilise circularly polarised light to generate fluid flow in a supersaturated solution. The rotational motion of dimers in circularly polarised light goes against much of the established literature and suggests that the transfer of spin angular momentum is enabled by combining particles together. And lastly, we demonstrate how a quadrant photo diode, performs in characterising the actual interactions between a dimer and the optical trap. We do so to demonstrate that much of the dimer's trajectory information is either lost or poorly described by simple calibration techniques, making their motion difficult to characterise.

4.0.1 Simulation Parameters

As a paradigmatic example, consider a dimer suspended in water ($n_p = 1.59, n_m = 1.33$) located at the focus of a Gaussian beam (more specifically a Laguerre-Gaussian beam of mode $[0, 0]$, see (2.12)), the beam is focused by a objective with numerical aperture

of 1.2 and is x polarised. The size ratio of the two spheres is given by $a_I/a_{II} = 2$ where a_I is kept at $1 \mu m$ unless specified otherwise; the dimer's orientation is given by a unit vector connecting the centres of both spheres (see 2.6.1). We define the 'standard' orientation as being aligned with the direction of beam propagation direction - and therefore the 'inverted' orientation is defined when the dimer is orientated against the direction of beam orientation (see left hand side of figure 4.1).

4.1 Positional and Orientational dependence of Trapping forces

If we wanted to start from first principles and determine the trap strength on our target particle the first step would be to locate the equilibrium position relative to the trap focus. For a single sphere it is easy to enough to understand that its centre of mass will be drawn to focal point of the laser due to gradient forces, once there the force is analogous to a harmonic spring with a fixed trap stiffness (see fig.2.1). Now, if we consider instead a dimer, we now have two spheres both being drawn to the focus along by the same gradient force; in addition the scattering force is significantly more complex due to both spheres scattering the electromagnetic fields. This mutual scattering between individual spheres is what makes simulating spherical aggregates far more difficult compared to a single sphere, and even harder still to predict the position where the dimer's centre of mass is in equilibrium.

Because the scattering force is only significant in the direction of beam propagation [73] we can assume there will only be a single potential well lying at the centre of the beam. Along the beam axis, such an assumption is no longer valid due to fact that spherical aggregates experience inter-particle scattering. This is a key reason for using *mstm* as it accounts for that behaviour. The methodology for computing optical forces has been covered extensively for a number of different trapping conditions [74]. So it is relatively easy to compute the trapping force and determine the equilibrium position by finding the position that minimises the net optical force and the local gradient is negative ($\delta F/\delta x < 0$) - we can assume that for a dielectric sphere the optical torque is

negligible. For a dimer (or any arbitrary spherical aggregate), we now must consider both its position and orientation and find where the net optical force and torque are minimised.

After computing its T -matrix via *mstm* and supplying that to *ott* we compute the optical force exerted by a 50 mW laser via (2.56) in the axial direction while the dimer is in its 'standard' orientation. As expected we see a single point where the dimer will be in equilibrium, the linear fit in fig. 4.1 (a) indicates that the force can be modelled as a harmonic potential close to the equilibrium position ($F_z \approx -\kappa_z z$). The second point where the axial force goes to 0 cannot be considered as equilibrium position as the positive gradient indicates that the trap is unstable unless Brownian motion is ignored.

We repeated the same calculation but now while the dimer is in its 'inverted' orientation, instead of a single point where the optical force is minimised we see that there are instead two separate equilibrium positions, one above the focus and one below the focus. In this particular example the two positions are far enough apart that both can be considered as separate harmonic traps.

We can see that both equilibrium positions have comparable axial trap stiffness (κ_z), however the difference in the transverse trap stiffness (κ_x) is far more noticeable. The same dimer was trapped at each of the axial equilibrium positions and the transverse force was evaluated. While in all three cases the dimer can be trapped the linear range where that would typically associated with a stable trap is far narrower in the 'standard' orientation compared to the 'inverted' cases. This highlights one of the challenges involved with studying asymmetric particles, even though it's a simple enough process to trap them they maybe characterised very differently depending on their relative position and orientation towards the focus. This can have a significant impact on rheological studies - or attempting to probe any local property - as the variance in trap strength can result in large errors over repeated measurements.

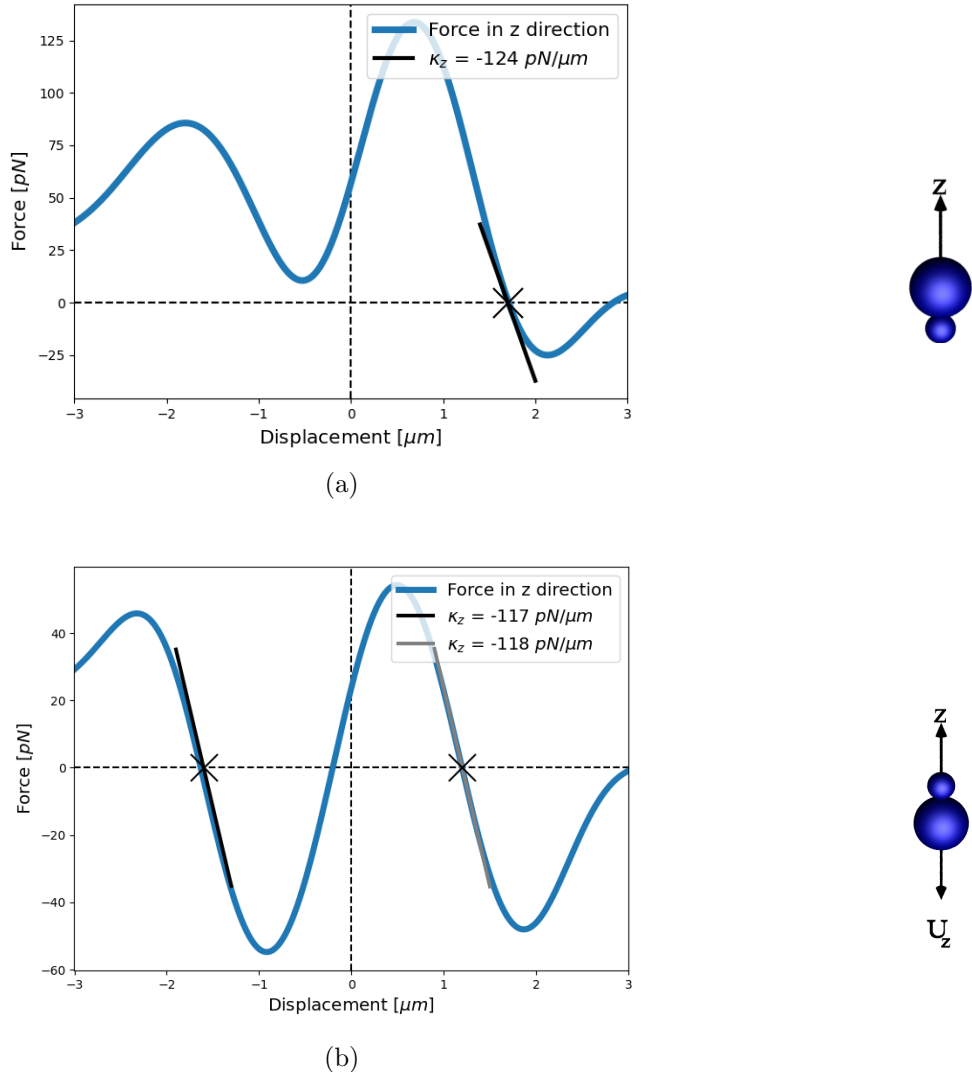


Figure 4.1: Plots of force vs displacement of the centre of mass of the dimer (μm) for the case of a dimer of size ratio 2. (a) is the case where the dimer is in its' 'standard' orientation, where the dimer is trapped at $z = 1.71 \mu\text{m}$. (b) is the case where the dimer is in its' 'inverted' orientation, the dimer is trapped at two positions: $z = 1.20 \mu\text{m}$ & $z = -1.63 \mu\text{m}$. On the left are renders to visualise the dimer orientation are shown below each plot. The black lines on each force-curve is a linear fit with the slope being reported as the trap stiffness in the legend.

For completeness the harmonic traps were located for dimers across a range of size ratios - from $a_I/a_{II} = 1$ to $a_I/a_{II} = 10$ - while also recording the trap stiffness for each trap. The same simulation parameters are used here as for figures 4.1 & 4.2. As shown

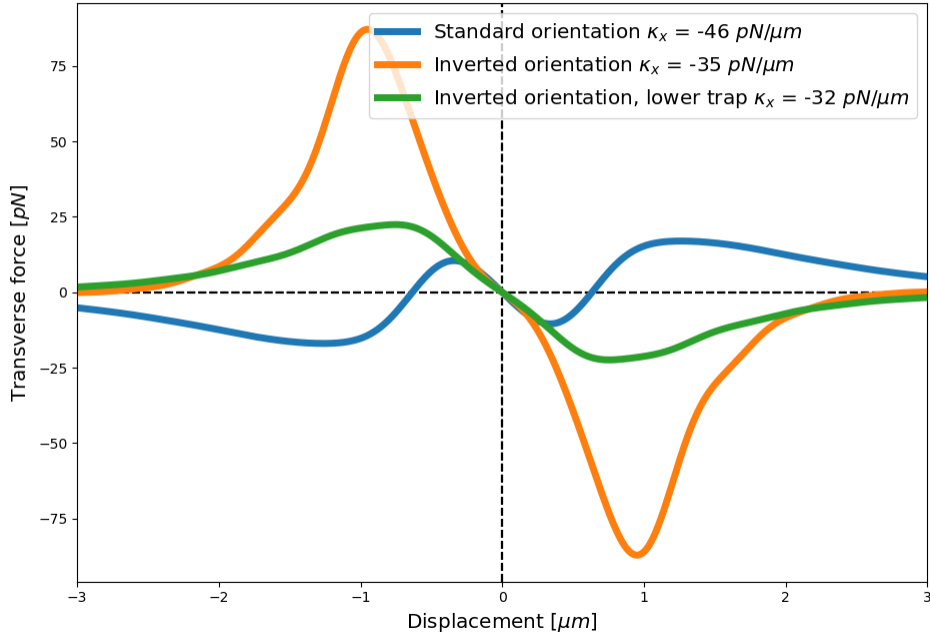


Figure 4.2: Plots of force vs displacement of the dimer’s centre of mass spheres, where a positive force indicates the dimer is directed right on the x-axis, and vice versa for a negative force. The same simulation parameters are used here as in fig 4.1(a) and (c). The blue curve representing the force response for a dimer in its standard orientation, orange being the inverted case, and green the same case but placed below the focus.

in Fig. 4.3 a_{II} decrease the dimer begins to approximate a single homogenous sphere - at least in terms of location and trap strength. However, for intermediate sized dimers (between $a_I/a_{II} = 1.1$ to $a_I/a_{II} = 4$), a second equilibrium position is found below the trapping focus. Previous work using the ray-optics model have confirmed even in the case that two spheres begin separated the electric field will align the particles as such that they make contact and are trapped together about a single trapping position [118]. Furthermore it has been shown through proper manipulation of the Gaussian or Bessel beam modes that any number of trapping potentials can be developed [123] for nanoparticles. This result however, is the first example of an orientation dependent trapping situation using only a TEM_00 beam. Typical experimental arrangements cannot determine much information on the axial position of a trapped particle rela-

Chapter 4. Complex Langevin dynamics of spherical dimers

tive to the trap focus; this result indicates not only that dimers can be trapped in multiple axial positions but also their trapping behaviour is heavily dependent on said axial position. As such it is necessary that positional information in the z-axis can be elucidated if multiple spheres are trapped simultaneously.

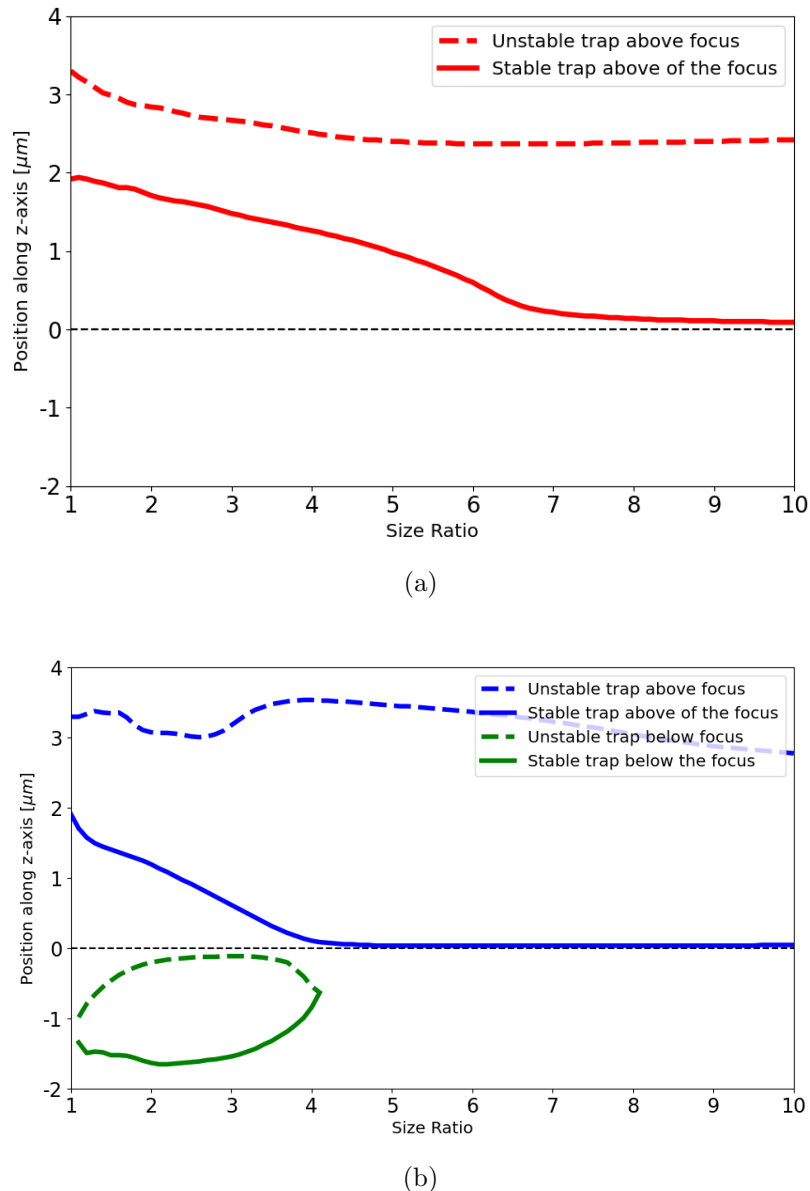


Figure 4.3: Equilibrium positions of optically trapped dimers with varying size ratio, dashed lines represent unstable traps whereas solid lines are for stable equilibrium positions. (a) shows that dimers while in their 'standard' orientation will always have a single equilibrium position. (b) shows that when the same dimer is in its' 'inverted' orientation can be trapped in two axial positions, one below the focus and one above the focus.

4.1.1 Non-trivial equilibrium configurations

Computing the equilibrium positions when a dimer is aligned with the electric field is relatively simple as the orientational torque is minimised (see Eq.1.5). Meaning once trapped the dimer is unlikely to change orientation enough to escape the trap. Regardless, that does not rule out the possibility that there is a stable configuration where the orientation not strictly vertical, in fact most experimental work with symmetric nano-dimers will trap them lying perpendicular to the beam direction [30], [61]. Unlike in Sec. 4.1 we cannot simply measure the optical force and torque as the parameter space is too large and determining if a particular position and orientation is stable is not clear based solely on force and torque measurements [124]. Using the same simulation parameters as before we ran a number short simulations (total simulation time was 0.005 s) with the laser power increased to 500 mW. Each simulation started with the dimer in a different starting position and orientation, due to the high laser power the dimers either escaped the trap or were stably trapped. The $z - \theta$ phase space - where θ is the angle between the direction of beam propagation and the dimer's orientation vector ($\theta = 0^\circ$ is the 'standard' orientation) - can be divided into different regions depending on which equilibrium configuration is reached.

Interestingly while the trap strength of these off-axis traps are similar in magnitude to the vertically aligned dimers, but when the laser power is lowered (around 5 mW) the traps become metastable; after reaching its' equilibrium configuration the particle behaves similarly to a typically trapped dimer but the trapping potential is small enough that the dimer escapes in as little time as less than a second or after nearly a full 3 seconds. Running similar simulations but for vertical configurations sees the dimer remaining trapped, even after 30 seconds of run time, indicating that the trapping potential is far greater than the thermal energy. This suggests that the reason this off-axis configuration is metastable is due to the increased rotational freedom. Similar configurations have been explored with ellipsoids; Zhu *et al.* looked at the dynamics of various elliptical particles and found that regardless of shape or initial orientation the particle would tend towards either a purely vertical or purely horizontal orientation [62].

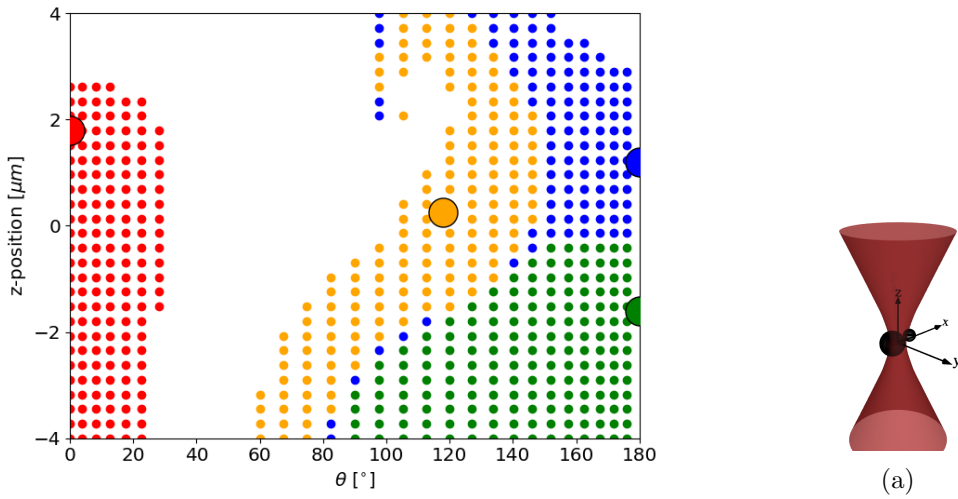


Figure 4.4: Map of $z - \theta$ phase space using a dimer of size ratio 2 with a laser power of 500 mW ($\theta = 0^\circ$ is the 'standard' orientation and $\theta = 180^\circ$ is the 'inverted' orientation). The stable configurations are indicated by the larger circles and the starting conditions are colour coded to match the stable point they end up in. Right hand render shows a dimer in its off-axis configuration.

4.2 Continuous rotational motion due to second-order scattering

One aspect that has yet to be covered in depth with regards to spherical aggregates of any construction is their interaction with circularly polarised light. For homogenous spheres the optical torque is regarded as being negligible as the spin density cannot impart angular momentum while propagating in a homogenous medium. Dimers however, have been shown to experience an optical torque [30], [61], [93] while trapped in a circular polarised beam. In our simulations we found that dimers would rotate about their long axis when trapped in circularly polarised light. In this section we want to discuss how this behaviour is influenced by size, position, and orientation; and furthermore, we wish to address possible explanations for this behaviour, as none of the current theories into optically induced rotation seem plausible.

4.2.1 Polarisation Dependency on Dimer trajectory

In their paper Vigilante *et al* attribute the rotational motion to the anisotropic shape of the dimer [93]. Anisotropic scattering is a viable theory for describing optical rotation, however there is usually an optical axis about which rotation occurs. For a dimer this is typically the orientation vector that passes through the centres of both spheres [30], [53], [61]. There have been cases where the particle's cross sectional shape is engineered to scatter light in one particular direction [64], but if this was the case then the dimer should rotate when illuminated by any polarisation of light.

To that end, we simulated the motion of an optically trapped dimer in beams of varying polarisation ($NA = 1.2$, $P = 100 \text{ mW}$), the dimer is composed of polystyrene ($n_p = 1.59$, $n_m = 1.33$). Each simulation was run for 1 second ($\Delta t = 10^{-5}$) and at the end we looked at the orientational time series; the dimer's orientation is recorded as a quaternion which can be easily converted to a 3-dimensional rotation matrix. By considering only the transverse components ($U_{1,x}$, $U_{1,y}$, $U_{2,x}$, & $U_{2,y}$) of the rotation matrix and taking the Fourier transformation of their time series reveals the rotational frequency. The laser power is set to 100 mW to avoid large thermal fluctuations and so that the Fourier series of the transverse components approximates $\delta(\omega_{rot} - f)$ - the Dirac delta function centred at the rotational frequency ω_{rot} .

$$q(t) \rightarrow R(t) = \begin{pmatrix} U_{1,x}(t) & U_{2,x}(t) & U_{3,x}(t) \\ U_{1,y}(t) & U_{2,y}(t) & U_{3,y}(t) \\ U_{1,z}(t) & U_{2,z}(t) & U_{3,z}(t) \end{pmatrix} \quad (4.1)$$

$$\rightarrow \int_{-\infty}^{\infty} R(t) e^{-i2\pi ft} dt = \begin{pmatrix} \delta(\omega_{rot} - f) & \delta(\omega_{rot} - f) & \delta(f) \\ \delta(\omega_{rot} - f) & \delta(\omega_{rot} - f) & \delta(f) \\ \delta(f) & \delta(f) & \delta(f) \end{pmatrix}$$

If the rotational frequency was not immediately obvious the simulation was repeated but over a longer simulation time. Four different size ratio of dimers were studied, both in their 'standard' and 'inverted' orientations. The results of this are displayed in

Fig. 4.5:

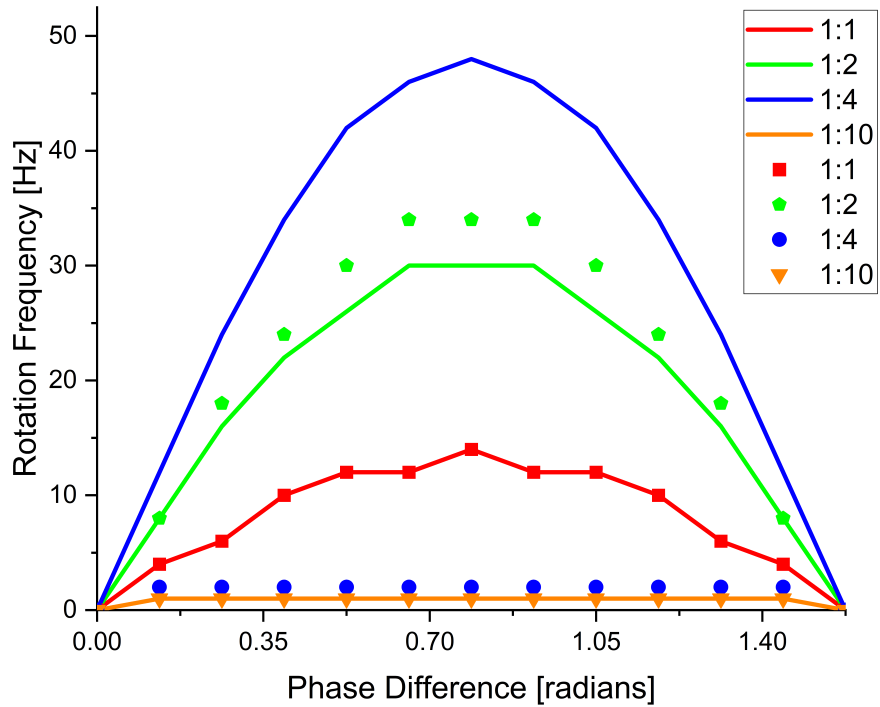


Figure 4.5: Rotation frequency vs component phase difference for differently sized dimers. The solid lines represent the rotation rate experienced while the dimer is in its standard orientation, whereas the solid points are for the case where the orientation is inverted. Laser power = 100 mW.

This shows us that these optical rotations are polarisation dependent and not merely an example of the dimer scattering light asymmetrically. The question then becomes, by what mechanism is the angular momentum of the trapping beam being transferred to the dimer.

In their work Vigilante refers to the spin-curl effects demonstrated by Grier *et al* [125], in which the curl of the spin density leads to a second order optical force that orbits around the beams central axis [126]. While several papers have demonstrated this phenomena [44], [127], [128] it was only properly formalised by [125]. In which they showed that the seemingly random trajectory of a trapped sphere was biased by the polarisation state of the trapping beam. While not immediately evident from the

trajectory the helicity of the trapping beam was revealed by computing the particle's probability flux using.

$$j(r) = \frac{1}{N-1} \sum_{j=1}^{N-1} \frac{r_{j+1} - r_j}{\tau} \delta_{sigma_j} \left(r - \frac{r_{j+1} + r_j}{2} \right) \quad (4.2)$$

where δ_{σ_j} is the kernel of an adaptive density estimator [129]. (4.2) describes the direction a trapped sphere is most likely move in given our statistical knowledge of the trajectories probability density function. A finite estimation of the density function $p(r)$ is used in [125].

$$p(r) = \frac{1}{N} \sum_{j=1}^N \delta_{\sigma_j}(r - r_j) \quad (4.3)$$

The probability flux reveals a biased motion in the trajectory of a single sphere (see Fig. 4.6). This biased motion results in a slight orbital motion about the central axis of the trapping beam, the orbital frequency is shown to be proportional to the polarisation state of the trapping beam.

While the results from [125] suggest that the optical rotation seen in asymmetric dimers can be attributed to the same spin-curl forces there are several discrepancies that cannot be explained purely by the spin-curl force. Firstly, there is the question of magnitude, the resulting rotation rate

4.2.2 Comparison of optical torques for Sphere and Dimers

It does raise the question of how come our simulations show that despite the dimer being orientated so their long axis' align with the parallel to the direction of propagation they still readily rotate. You would not expect that the addition of a single additional sphere should drastically adjust the torque especially if said sphere is relatively small. However when we measured the optical torque of a single sphere and a dimer - $a_I/a_{II} = 10$ - we found the exact opposite. In both cases we used the same trapping beam as used for fig. 4.5 but with a circularly polarised beam. Both the sphere and dimer were rotated in the $x - z$ plane and the all three components of the optical torque were recorded.

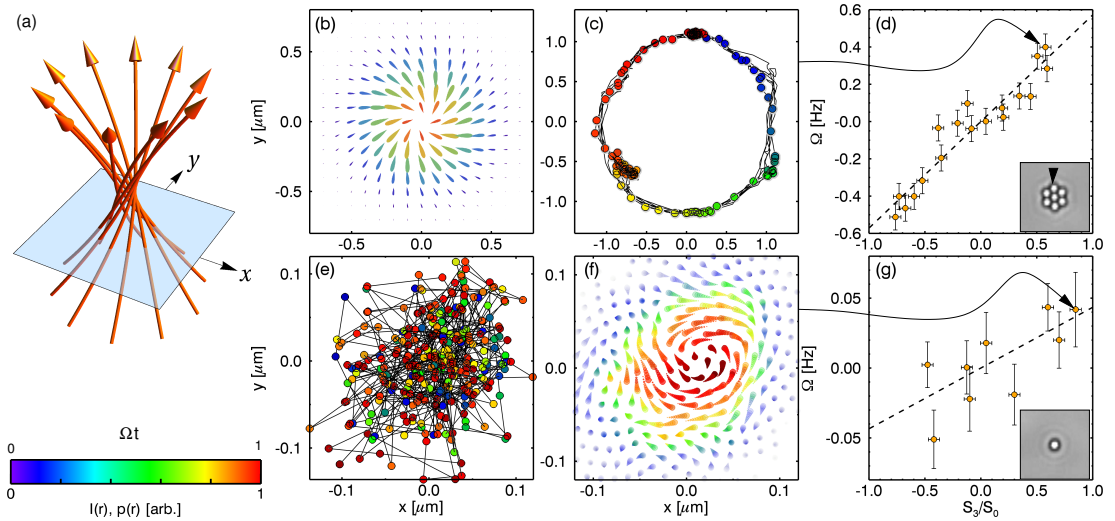


Figure 4.6: Figure reused from [125]. (a) shows how the momentum density of a Gaussian beam is twisted while using circularly polarised light. The top row (figures (b)-(d)) shows a 7 sphere cluster trapped in a circularly polarised beam. Due to the clusters asymmetric susceptibility to polarization the cluster rotates in the $x - y$ plane. Whereas the bottom row (figures (e) - (g)) show the similar results for a single sphere. In this instance the sphere does not rotate but instead orbits the beam axis. In both instances the motion is proportional to the degree of polarisation (see figures (d) and (g)) but for the single sphere this motion is only revealed when using (4.2) & (4.3). Reused with permission from author

The torques about the x and y axis can be somewhat understood as the second sphere is being drawn back towards the centre of the trap by the gradient forces. The same cannot be said for the z - component of the optical torque; while this effect could still be attributed to the spin-curl force, but it is clear that the internal scattering between the two spheres has some unintended effects.

4.2.3 Rotational frequency as a function of size ratio and orientation

Next we want to see how the rotational speed is influenced by different sized dimers. Intuitively, you would expect that a larger would experience a greater torque and therefore rotate faster. By repeating the same kinds of simulation as used in 4.5 but for a circularly polarised beam $\phi = 90^\circ$ it was found that not only is the rotation rate dependent on the size of the dimer, but also on its orientation and therefore their axial position.

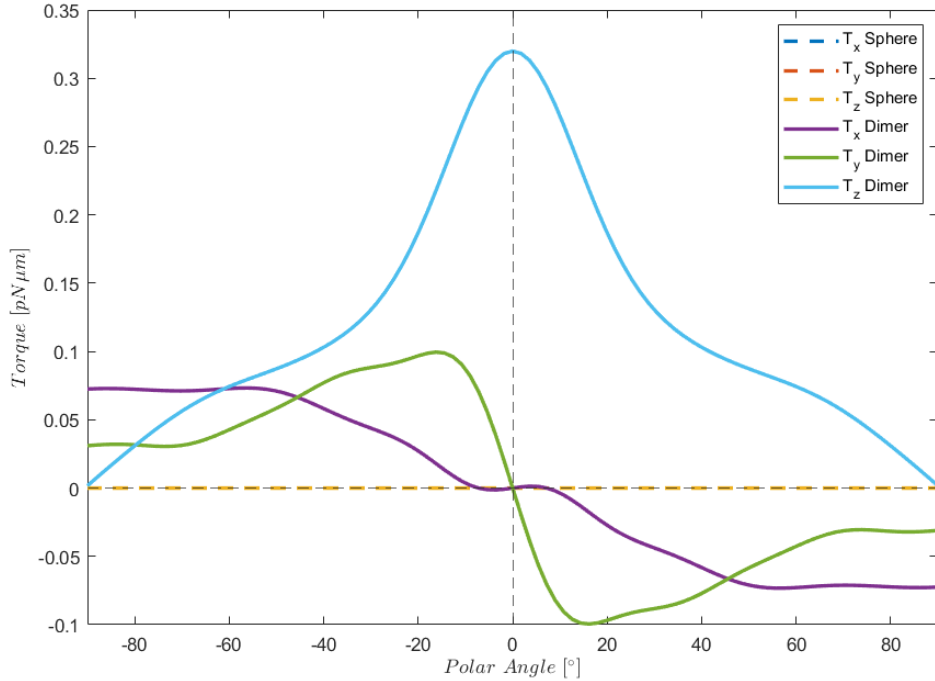


Figure 4.7: Optical torque experienced by a dimer ($a_I/a_{II} = 10$) and a single isotropic sphere. Both were rotated in the $x - z$ plane and the angle between U_z and the beam axis gives the polar angle. The solid lines denote the torque experienced by the dimer whereas the dashed lines represent the torque experienced by the sphere.

It is difficult to see from the graph, but the rotation rate never truly goes down to zero, reaching a minimum of 2 Hz, which would imply that a second sphere of radius 200 nm is enough to induce rotational motion. This brings into question what mechanism is generating the optical torque. We used *mstm* to look at the stokes parameters from the scattered field from a simple plane wave incident on a symmetric dimer, the proportion of circularly polarised light is minimal compared to the proportion of plane polarised light, which indicates that this rotational motion is not due to any inhomogeneity in the dimer that might impart angular momentum to the scattered beam - as compared to a anisotropic scatterer like vaterite.

These results are somewhat contradictory to other work with silica dimers [30], [61], [67]; previous experiments have trapped the dimer in an orientation perpendicular to the beam propagation direction. The rotational motion is attributed to the dimers

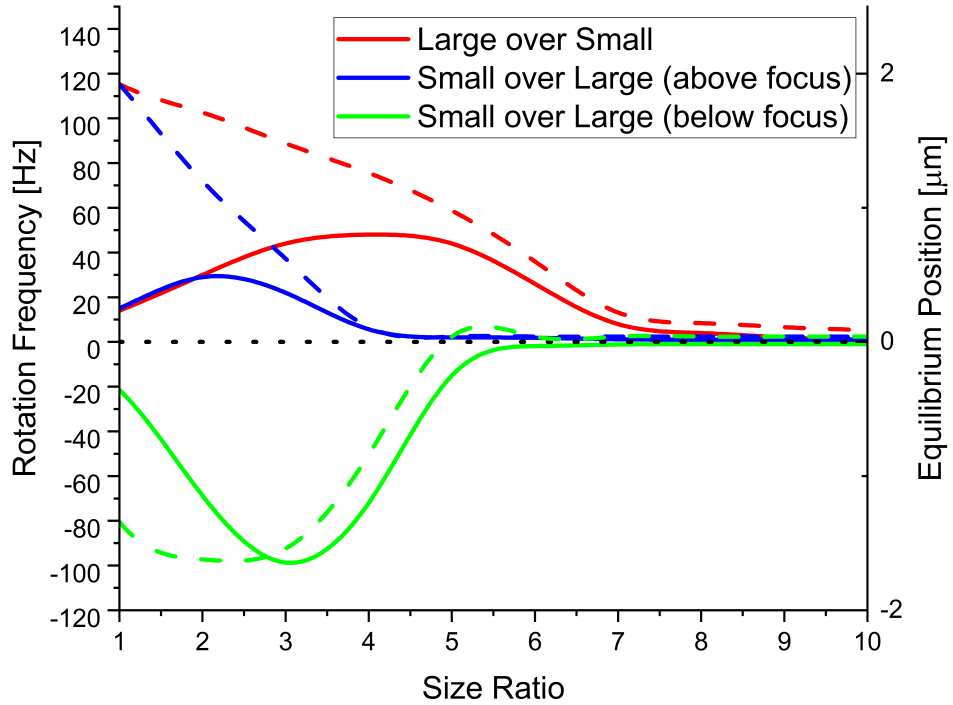


Figure 4.8: Rotation rate plotted against dimer size ratio while trapped in a circularly polarised beam; a positive rotation rate indicates clockwise rotation, whereas a negative rotation rate indicates counter-clockwise rotation. The red line is for the case of a dimer in its 'standard' orientation. The blue line is for the case when the dimer is in its 'inverted' orientation while trapped above the focus of the beam. And lastly the green line is for the case when the dimer is in its 'inverted' orientation, but when it is trapped below the focus of the beam.

asymmetric geometry creating an unbalanced polarisation susceptibility along its long axis as compared to its short axis; therefore its long axis is aligned with the polarisation vector and can rotate freely [30]. This however cannot be the case with our simulations as the dimer rotates about its long axis, meaning there cannot be an asymmetric axis to align with the beam's polarisation vector. Furthermore, we see a non-linear increase in the rotational speed of our dimers with size, the drag torque from the surrounding fluid is $\propto r^3$ so the expectation is that the rotation frequency should fall off with increasing size. This indicates that the rotational motion is due to the shape asymmetry of the dimer and not solely due to the beam's angular momentum. Measurement of this photo-

kinetic force is difficult to achieve due to the fact that previous analysis was conducted in the Rayleigh regime, where the polarizability of our dimer can be approximated as:

$$\mathbf{p}(\mathbf{r}, t) = \alpha_x E_x(\mathbf{r}, t) \hat{\mathbf{e}}_x + \alpha_y E_y(\mathbf{r}, t) \hat{\mathbf{e}}_y + \alpha_z E_z(\mathbf{r}, t) \hat{\mathbf{e}}_z \quad (4.4)$$

where the polarizability is given as a 3D vector for the three principle Cartesian directions. In order to measure the magnitude of second order contributions we would need to construct a dipole array that fully captures the scattering of a dimer. Measuring the optical torque makes it clear that the polarizability is a contributing factor to this optical rotation phenomena.

4.2.4 Gyroscopic Precession using asymmetric dimers

As mentioned in section 4.1.1 for specificity sized dimers there is the potential for non-vertical trapping orientations in which the dimer is still stably trapped. When a circularly polarised beam is used the dimer exhibits gyroscopic precession. As shown in fig. 4.9 the dimer's trajectory exhibits periodic rotation about its long axis U_z , precession motion as the dimer spins around the central beam axis, and nutation motion as the dimer's orientation rocks backwards and forwards.

Applying a Fourier analysis to the above trajectory reveals the 3 fundamental frequencies typically associated with precession; the $u_{z,1}$ and $x(t)$ series show a precession frequency of 1.33 Hz whereas the series $u_{x,1}$ and $u_{y,1}$ show a combined periodic signal - a rotational frequency of 23 Hz and a nutation frequency of 20 Hz. Previous studies into amorphous silica nanoparticles found a linear relationship with the rotational frequency and the laser power, but no such relationship existed with the precession frequency.

This gyroscopic motion has been demonstrated previously in nanoparticles [62], [130]–[132] but has not been observed for micron scale aggregates. Since the torque applied to the dimer is computed by evaluating the beam coefficients of the scattered field it is difficult to apply this result to micro-rheology experiments as one would need to know the exact magnitude of the optical torque ahead of time in order to make

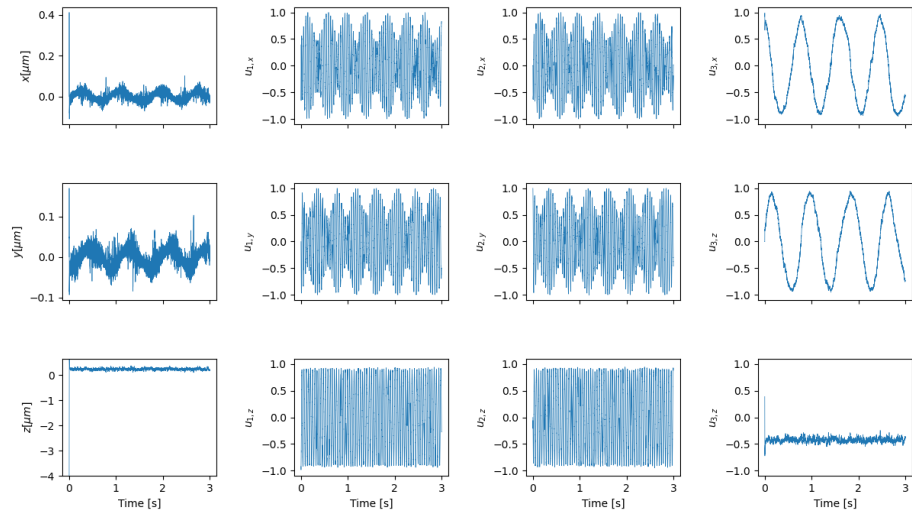


Figure 4.9: 3 second trajectory of a dimer ($a_I/a_{II} = 2$) trapped in an off axis orientation with a circularly polarised beam ($P = 100 \text{ mW}$). The far left column depicts the dimer’s centre of mass position with time; middle two columns are the x , y , and z components of the vectors u_x and u_y ; last column depicts the components of the vector u_z which defines the dimer’s orientation.

estimations about the local fluid viscosity. This is trivial for a birefringent spherical particle, less so for spherical aggregates whose equilibrium position and orientation are unknown. However, further analysis of the mechanism behind the precessive motion of off-axis dimers may provide insights into controlling Brownian motion. An experimental work trying to ‘cool’ nano-dimers by controlling the motion in all 6 degrees of freedom found that even while the rotation about the short axis’ could be controlled the free rotation around the dimers’ long axis resulted in an unpredictable torsional vibration [65]. Understanding how rotational motion arises in the Mie-Regieme could allow researchers to build a robust theoretical framework to construct beam structures that eliminate any unwanted rotational motion from a target particle. Conversely, the same framework could allow for precise measurements of the optical torque applied to a target particle, allowing for characterisation of complex shaped particles’ interactions with an optical trap.

4.3 Characterisation of asymmetric dimers via PSD analysis

As discussed in 2.7, one of the methods developed to work in conjunction with [93] is a simulated quadrant photo diode for as a position detection system. While it is possible to extract all of the relevant dynamical information from a simulation, confirming the same behaviour in an experimental setting can be challenging if dealing with a non-birefringent anisotropic scatterer. The QPD is composed of 4 photodiodes that measure the intensity of light incident on their surfaces. Using ott we can define a region in the far-field that is analogous to the surface of the QPD surface. Evaluating the electric field across this surface gives us an approximation of the QPD signal outputted in an experimental situation. This does not provide a one-to-one result however as hardware errors (i.e. internal resistance, external light sources, and vibrations) would distort the signal somewhat. We can use this as a means to examine the limitations of using back-focal plane interferometry as a means for characterising anisotropic scatterers.

As a benchmark we start by considering a single sphere within an optical trap. A single polystyrene sphere suspended in water ($a = 1\mu m$, $n_p = 1.59$, $n_m = 1.33$) was trapped by a focused Gaussian beam ($NA = 1.25$) using circularly polarised light. For the sake of time efficiency the trajectory was sampled every 10 time steps, meaning the upper bound on the power spectra is $f_{Nyq} = f_{sample}/2 = 5000\ Hz$. To optimise the frequency window we fitted the power spectra using the aliased Lorentzian (Eq. (??)).

As shown in fig. 4.10, the two power spectra report different corner frequencies which would indicate that the trap is not perfectly circular. We can use both ott and the trajectory itself to derive an estimation of the trap geometry. The corner frequencies and corresponding trap stiffness are reported below:

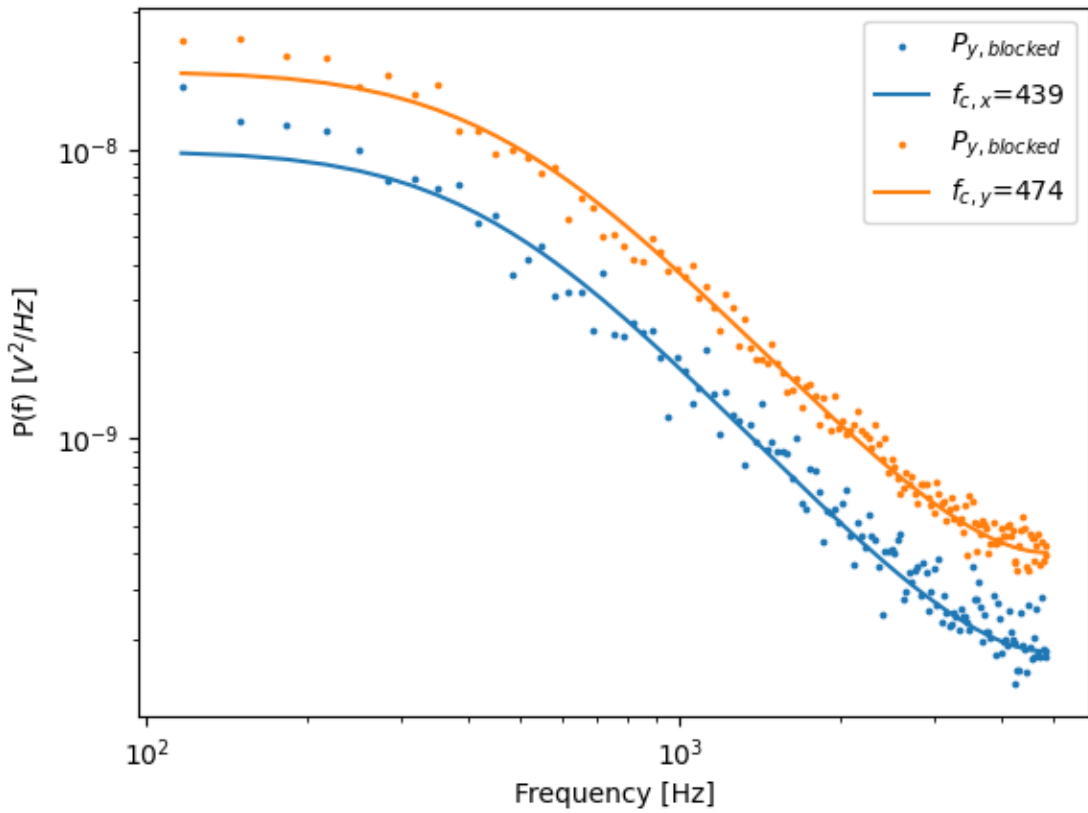


Figure 4.10: Recorded power spectra fitted to eq. 2.49, scattered points represents the blocked data ($n_b = 100$). Corner frequency for the Lorentzian curves are reported in the legend.

Table 4.1: QPD fitting for single sphere

Fitting parameter	<i>ott</i> estimates		QPD fitting		Trajectory fitting	
f_c [Hz]	447	450	439	474	523	513
$\sigma(f_c)$ [Hz]	—	—	9.30	9.65	8.67	8.61
κ [$pN/\mu m$]	53.05	53.40	51.96	56.09	61.94	60.7
Ellipticity	8.16 %		27.17 %		13.8 %	

Where $\sigma(f_c)$ is computed from [91], where the variance is based upon our choice of frequency boundaries ($f_{min} : f_{max} = 100$ Hz : 5000 Hz). And the ellipticity of the beam is given by $e = (1 - \kappa_y/\kappa_x)^{0.5}$ and is a measure of the symmetry of the beam wavefront. Its clear from these initial results that the QPD is more sensitive to changes along the y-axis than the x-axis when compared to the direct *ott* calculations. This

is somewhat reflected in the trajectory results. Typically, even an industrial Gaussian beam will produce an elliptical diffraction limit spot when heavily focused; in their tutorial for optimizing the PSD analysis, Berg and Sorensen reported a ellipticity of around 15 % after a total calibration time of 80 seconds [91].

The reason for the discrepancies between all 3 methods is due to what is actually being measured. The *ott* estimates are simply looking at the differences in the trapping strength along the Cartesian axis'. If calibrated over an long enough time frame you would expect that the resulting power spectra would exactly mirror the *ott* predictions. However over a short calibration time a QPD can predict large discrepancies in the trap strength. There is a clear trade off in terms of accuracy and computation time as shorter calibration runs are computationally more efficient but prone to errors. This is the case even if we know the exact positional data.

With this in mind, let us consider a symmetric dimer that is optically trapped by the same Gaussian beam. Not only does the dimer's equilibrium position change but it is subjected to rotational motion due to the beam's angular momentum. This is reflected in the calibration results using the simulated QPD, where we see a drastically different estimation between the *ott* estimate and the QPD estimate.

Table 4.2: QPD fitting for symmetric dimer

Fitting parameter	<i>ott</i> estimate		QPD fitting		Simulation fitting	
f_c [Hz]	409	334	431	424	274	285
κ [$pN/\mu m$]	48.51	39.58	51.13	50.26	32.45	33.75
Ellipticity	42.8 %		12.7 %		13.8 %	

Now we see that the *ott* predicts a more elliptical trap compared to the QPD model which says the trap is far more symmetrical while trapping a symmetric dimer. A potential reason that *ott* no longer expects a circular trap could be due to how it computes the beam shape coefficients; by point matching in the far field before the focus means a loss in accuracy for objects that trap above the focus. The change in the QPD estimation can be partially explained by the fact that rotational effects are not accounted for in the Lorentzian power spectra, only translational motion. Typically, rotational motion is only ever detected when it is periodic (take for example Fig. 3.4), when the

motion is stochastic the entire power spectra is effected making it near impossible to separate the translational and rotational contributions from a single power spectra.

4.4 Conclusions

Considering the simplicity of a scatterer such as a dimer, one would assume that the dynamics of such an object would be relatively easy to predict. Simulations of dimers in the Mie regime show that not only do they have multiple positions and orientations in which they can be trapped but also that their interaction with circularly polarised light is heavily dependent on the axial position and trapping orientation.

Dimer's have the potential to be used as tunable micro-rotors, being simple to synthesise and can be made out of any material of choice. The rotation demonstrated by dimer's is not accurately described in previous literature which raises questions on the interactions between circularly polarised light and spherical aggregates. Being made up of homogenous materials there is no change in polarisation as expected by birefringence. Shape birefringence is also not applicable as the preferred orientation is perpendicular to the polarisation axis, meaning there can be no asymmetry in the dimer's susceptibility.

Chapter 5

Detection and Characterisation of rotational spherical aggregate rotational dynamics

As outlined in the end of Chapter 4, one of the difficulties in characterising interactions with asymmetric objects is the coupled motion between translation and rotation. In order to characterise the optical trap a position detection system such as a lateral effect photodiode or a quadrant photo diode (see fig.??). Typically, a position detection system assumes that there exists a linear relationship between the a particle's displacement and the detected signal. However, this is not always the case as demonstrated in chapter 4; as dimer's demonstrate non-harmonic trapping beyond a certain displacement. In addition, the rotational effects of the trapped dimer become a more significant factor when characterising the trap strength. This can have unintended effects when it comes to areas of research that require a precise understanding of the hydrodynamic behaviour of particles. As such there has been a concerted effort to either eliminate rotational motion, or describe how the rotational behaviour influences the trajectory reported by the position detector.

Rotational motion about a single axis is easiest to account for. When the power spectra of elliptical polystyrene particles was fitted by Yogesh *et al* [97], they assumed that the rotational motion was purely in the transverse plane. As such they did not

have to account for any variance in the trapping strength due to orientation nor did they need to consider non-periodic rotational behaviour. In the case where rotational motion is stochastic the problem is more complex. For example, when an optical fibre trap characterisation technique was implemented by Saffron *et al* [133], [134], they were able to use dynamic light scattering to characterise both the axial and lateral trap stiffness acting on microspheres. The only drawback admitted to in their work was that the technique was constrained to isotropic scatters as their theoretical model for describing the auto-correlation function was predicated on the fact that any variations in the signal are due to the particles translational motion within the confines of a cylindrical trap [133]. Where the upper limit of the cylindrical trap is given by the Rayleigh range ($z_R = n\omega_0/NA$). However, as demonstrated by the results from Chapter 4.1, the axial traps of spherical aggregates is often situated far beyond the Rayleigh range (for a 1.2 NA laser this is $\pm 5.985\mu m$).

To accurately describe the full dynamics of an anisotropic scatterer its clear that additional characterisation techniques are necessary. In this chapter we demonstrate two such techniques, quadrant photo-diode simulation, and an optical fibre static light scattering arrangement. The former is based on the work of Rohrbach and Stelzer [100], where their work is limited to single spheres, we extend the possible particle space to allow for any theoretical combination of spheres. The results from chapter 4 demonstrate that the rotational motion causes significant deviations between the computed trapping strength and the expected trapping strength according to Lorenz-Mie theory. By utilizing vector regression we can accurately recreate a particle's trajectory simply from the QPD signal, both in the transverse plane and along the beam axis.

The latter method builds upon [133] but now accounts for the full rotational motion. This was initially developed in tandem with the work conducted in chapter 3, with the idea being that if a crystal nucleus formed on a rotating sphere how would that nucleus influence the motion of the rotating sphere. Using static light scattering we can map the outputted signal from a optically trapped dimer to its expected orientation in real time. Thus allowing us to estimate the optical torque being applied to the dimer by the trapping beam. As demonstrated in chapter 4, the influence of a circularly polarised

beam can result in gyroscopic precession for specifically sized dimers.

We start by outlining the working principle behind the optical fibre detection system, before demonstrating how it can be used to instantaneously predict orientational information on a trapped particle. We then consider common factors of error in the characterisation process, such as signal error, and incorrect particle sizing. Both of which have a significant impact on the performance of the model, but by utilising Bayesian inference, and time averaging we can better refine our model.

5.1 Monitoring Stochastic rotational motion using static light scattering

Part of the optical fibre arrangement borrows code from the optical tweezer simulations discussed in Chapter 2 and 4. Rather than repeat the simulation details we will instead only focus on the specifics of the optical fibre scattering.

5.1.1 Coordinate System

Consider a particle (either a sphere or dimer) trapped by a Gaussian beam, with its focal point being set at [0,0,0]. At the same time an optical fibre directs a plane wave that is incident on the trapped particle scattering light in all directions. The probe beam is assumed to be x-polarised and propagating in the +z direction, this is a 90° rotation from the previous simulations (see fig X.X).

5.1.2 Dimer

The dimer is defined by two spheres with refractive indices of 1.59 and suspended in water ($n_{med} = 1.33$). *MSTM* requires a target origin for setting the scattering expansion, as with our simulations we set it as the dimer's centre of diffusion.

5.1.3 Scattering and Detection

Each detector is placed some distance \mathbf{r} from the origin, detector positions are defined by angles θ & ϕ . With $\theta = \phi = 0$ being directly in front of the probe beam. The

position of each detector is given by:

$$\begin{pmatrix} x_{fiber} \\ y_{fiber} \\ z_{fiber} \end{pmatrix} = \begin{pmatrix} r\cos(\phi)\sin(\theta) \\ r\sin(\phi)\sin(\theta) \\ r\cos(\theta) \end{pmatrix} \quad (5.1)$$

Where r is the distance between the detector and the target origin. In an ideal situation the surface of the detector is oriented towards the target origin perfectly. Pixels can be thought of as points lying on the surface of the detector, each point has its own position in real space. Using *mstm* we can find the components of the scattering matrix at each point and compute the intensity of the electric field via:

$$\begin{pmatrix} I_s \\ Q_s \\ U_s \\ V_s \end{pmatrix} = \begin{pmatrix} S_{11} & S_{12} & S_{13} & S_{14} \\ S_{21} & S_{22} & S_{23} & S_{24} \\ S_{31} & S_{32} & S_{33} & S_{34} \\ S_{41} & S_{42} & S_{43} & S_{44} \end{pmatrix} \begin{pmatrix} I_i \\ Q_i \\ U_i \\ V_i \end{pmatrix} \quad (5.2)$$

Where:

$$I_s = E_{x, scat}^2 + E_{y, scat}^2 \quad (5.3)$$

$$\rightarrow I_s = S_{11}I_i + S_{12}Q_i + S_{13}U_i + S_{14}V_i \quad (5.4)$$

By computing the scattering at each point on the detectors surface we can compute the average scattering over the detector. From a experimental perspective the distance from the particle to the detectors must be considered. The near field scattering can be computed with relative ease using *mstm* as shown in

While *mstm* does provide the amplitude matrix it is not scaled to account for distance from the target to the detector. We amend this by simply scaling according to the inverse square law. As the detector is moved further from the target the intensity distribution across the entire detector will decrease substantially. Because of the fall off it is more computationally efficient to instead consider only the central pixel of

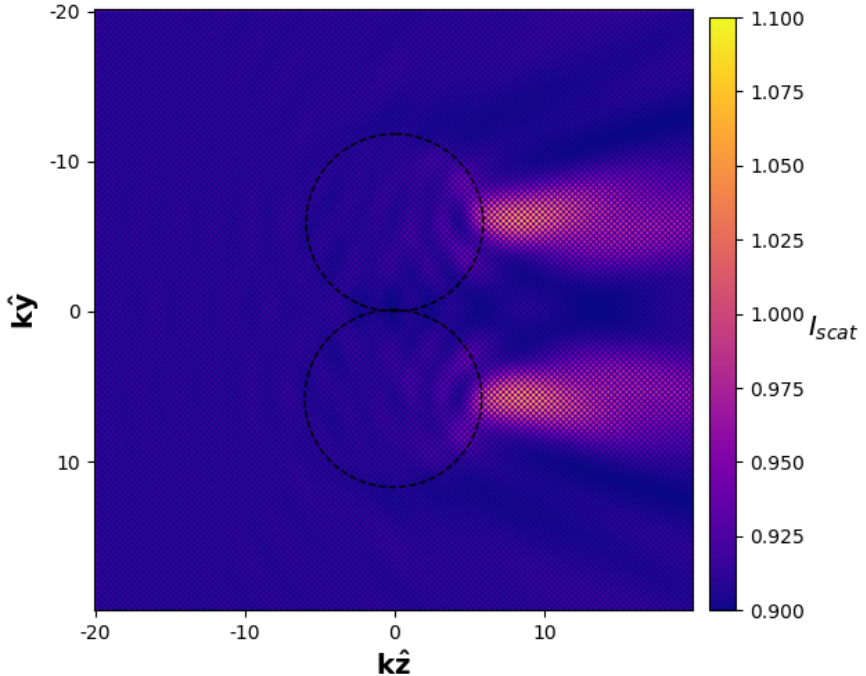


Figure 5.1: Intensity distribution (as defined by (5.3)) from a symmetric dimer when irradiated by the probe beam propagating in the $k\hat{z}$ direction (viewed in the z-y plane). Axis are given in dimensionless units of $k\hat{z}$ and $k\hat{y}$.

the detector rather than across the entire surface. If we consider the difference between the average intensity and the intensity of the central point we can see that after not even 20μ away from the target particle the average intensity across the surface is within 0.1% of the central pixel.

By moving the detectors further back we can treat each detector as single point and compute the intensity at the centre of the detector rather than consider the full surface. For computing the instantaneous orientation we only consider the intensity at the centre of the detector.

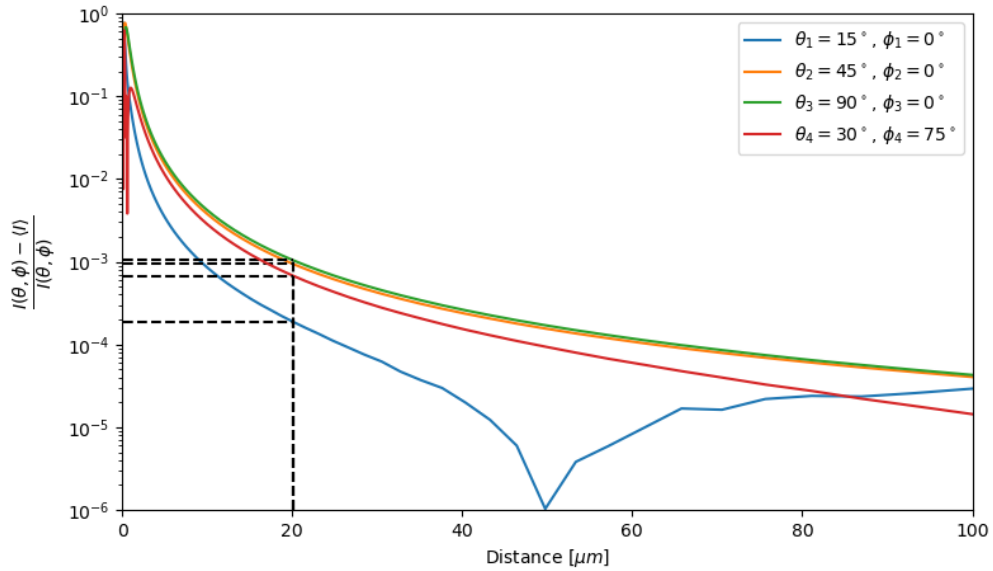


Figure 5.2: Normalised difference between the central pixel intensity $I(\theta, \phi)$ and the average pixel intensity over the surface of the optical fibre $\langle I \rangle$ as a function of distance. 4 different optical detectors were tested (spherical coordinates are given in the legend). While the choice of coordinates is arbitrary they all demonstrate the same exponential decay. Dashed lines indicate the difference after $20\mu m$ from the trap focus, in most practical cases getting an optical fibre any closer would disrupt the trap stability.

5.2 Interpretation of scattering data into orientation estimates

We now discuss the methodology for computing the instantaneous orientation of an optically bound particle based on scattering detected by a finite grouping of optical fibres.

Consider a dimer in the optical trap (Fig. 5.3a), we can define at any point in time a unit vector \hat{s} pointing from the centre of the larger sphere to the centre of the smaller sphere. A plane wave probe beam incident, is incident on the dimer, generating a scattering pattern dependent on the dimer's orientation $I(\hat{s}, \theta, \phi)$ which is computed using *mstm* [135]. To represent the experimental set up consisting of a set of optical fibres recording scattered light, we choose four sets of spherical angles $[(\theta_1, \phi_1), (\theta_2, \phi_2), (\theta_3, \phi_3), (\theta_4, \phi_4)]$ and record the calculated intensity at each angle

$$I(\hat{s}, \theta_k, \phi_k).$$

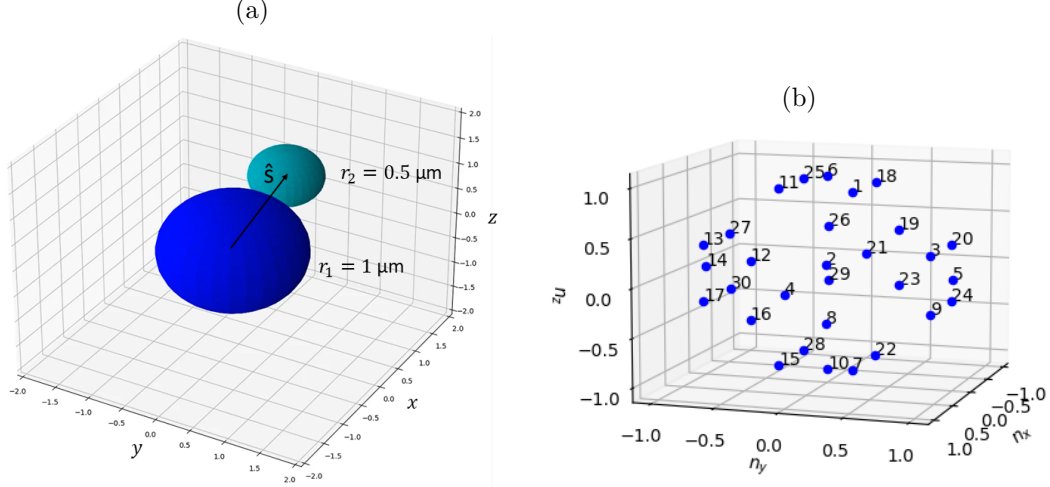


Figure 5.3: (a) Example dimer in orientation \hat{s} , (b) 30 Reference orientations represented by vectors pointing from $[0,0,0]$ to each point

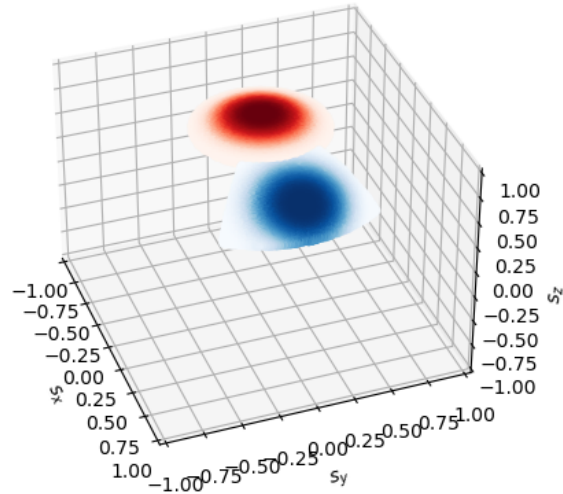
Our goal is to determine the orientation of the trapped dimer based on the measured intensity $I(\hat{n}, \theta_k, \phi_k)$. Rather than aim an exact estimate of the dimer's orientation, for the purposes of interpretation of the scattering and optimisation of the measurement setup it is more convenient to discretize the possible orientation space into a number of possible reference orientations. We can then use each as 'classification categories' in a neural network methodology to map scattering data to orientation (see below for further discussion). Here we choose $n_{ref} = 30$ reference orientations $\hat{\mathbf{n}}_\alpha$ evenly distributed on a unit sphere [136] (Figure 5.3b) leading to a maximum nearest neighbour spacing between two neighbouring reference orientations of 0.895 radians. Using *mstm* we compute the raw intensities at each of the measurement angles that would be generated by a dimer in each reference orientation, $I(\hat{\mathbf{n}}_\alpha, \theta_k)$. While the number and position of detection fibres is technically arbitrary there are several constraining factors that limit our ability to infer useful information from the trapped object, see Section 5.2.2 for a detailed breakdown of our choice of detection angles. In order for a neural network to properly weight each signal the raw intensities are normalized according to:

$$y_k(\hat{\mathbf{n}}_\alpha) = \frac{I(\hat{\mathbf{n}}_\alpha, \theta_k) - \langle I(\hat{\mathbf{n}}, \theta_k) \rangle}{\langle I^2(\hat{\mathbf{n}}, \theta_k) \rangle - \langle I(\hat{\mathbf{n}}, \theta_k) \rangle^2} \quad (5.5)$$

where the denominator is simply the standard deviation across the set of values $I(\hat{\mathbf{n}}, \theta_k)$. Note that the collected scattering signals are not necessarily simply related to their associated reference orientations: as is well known from such examples of the inverse scattering problem. While it is trivial to compute the light scattering pattern for any given particle with any particular characteristic (i.e. size, shape, or orientation), inferring the light scattering from a unknown particle to determine said characteristic is incredibly difficult due to complex mapping between scattering and said characteristic. Even if the orientation space is divided evenly between reference orientations the subsequent signal space ends up being appearing mixed making simple comparisons of signals useless for inferring information on the particle.

Fig 5.4 shows two clusters of orientation vectors and their respective signals collected from 3 detectors - the points have been coloured based on their proximity to the centre of their respective cluster. While the orientation space appears tightly packed and ordered the signal space quickly spreads out in an asymmetric fashion. Furthermore as seen in Fig 5.4b the signal mapping can intersect itself which only further increases the complexity. While in some instances the mapping between one reference orientation and another is discrete, in other instances the mapping becomes far more complex to discern.

(a)



(b)

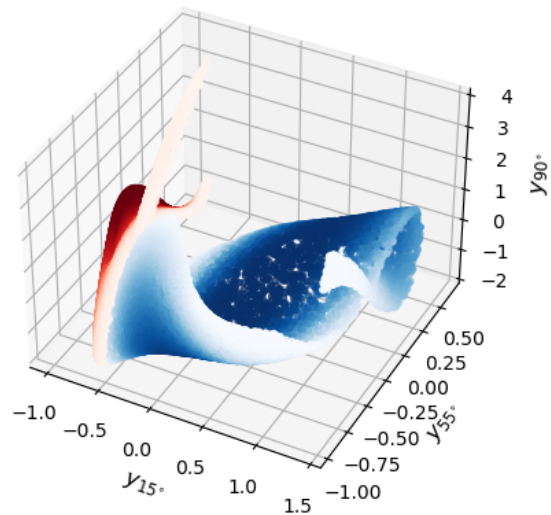


Figure 5.4: (a) Distribution of orientation vectors and (b) their respective scattering signals. Points are coloured according to their distance from the centre of each cluster (red points centred around $[0.00, 0.00, 1.00]$, blue points centred at $[0.71, 0.00, 0.71]$)

Nevertheless, at least where the uncertainty in signal measurements is low, we can predict the orientation from the scattering scattering by utilising computational techniques such as neural networks. We thus utilised the Python machine learning program *scikit-learn* [137] to build a neural network for identifying the dimer's orientation from its light scattering signal. The network was trained by generating a database of random orientation vectors, calculating the corresponding light scattering signals, and then using the network to estimate the probability of a given signal coming from a dimer in a given reference orientation. The network's loss function was evaluated and used to improve the estimation, the network being trained until the improvement in the loss function was less than 0.0001.

Importantly, the estimation provided by the neural network can be improved further by accounting for any prior information we know about the dimer, utilising Bayesian inference to update the neural network's estimation:

$$p(\hat{\mathbf{n}}_\alpha | y_k(\hat{\mathbf{s}})) = \frac{p(y_k(\hat{\mathbf{s}}) | \hat{\mathbf{n}}_\alpha)p(\hat{\mathbf{n}}_\alpha)}{p(y_k(\hat{\mathbf{s}}))} \quad (5.6)$$

where $p(\hat{\mathbf{n}}_\alpha)$ and $p(y_k(\hat{\mathbf{s}}))$ are the prior estimates of the distributions of particle orientations and instantaneous signals, respectively. *Without* any prior evidence we must assume that the orientation prior of the dimer $p(\hat{\mathbf{n}}_\alpha)$ is uniform. However, inference about the dimer's possible current orientation from knowledge of previous measurements can be used to inform our estimate of $p(\hat{\mathbf{n}}_\alpha)$. The latter prior $p(y_k(\hat{\mathbf{s}}))$ is the probability of measuring a signal (y_1, y_2, y_3). This is given by taking the discrete integral over the collection of reference orientations:

$$p(y_k(\hat{\mathbf{s}})) = \sum_{\alpha=1}^{n_{\text{ref}}} p(y_1, y_2, y_3, y_4 | \hat{\mathbf{n}}_\alpha)p(\hat{\mathbf{n}}_\alpha) \quad (5.7)$$

From (5.6) we obtain the key result, a mass probability distribution denoting the probability that our dimer is in orientation $\hat{\mathbf{n}}_\alpha$ given a measured signal (y_1, y_2, y_3), *i.e.* an estimated mapping from scattering measurement to orientation estimate.

5.2.1 Calculation of error

Using (5.6) we get a snapshot estimation of the instantaneous orientation of the trapped dimer based on a single measurement from a collection of detector signals. Of course in reality these detectors will be returning a discrete time series representative of the dimer's trajectory within the optical trap.

Using the simulation code from [93] we can replicate this trajectory and furthermore use *mstmmo* to calculate the far field intensity produced by said dimer. At each time step we measure the signal produced at each measurement angle and use our neural network to calculate $p(y_k(\hat{\mathbf{s}})|\hat{\mathbf{n}}_\alpha, t)$.

Evaluating how well Eq. (5.6) performs in predicting $\hat{\mathbf{n}}$ is difficult because we have discretised the orientation space meaning there will always be some degree of inaccuracy in our prediction. The Kullback-Liebler divergence method provides a measure of the relative entropy change between two probability distributions:

$$D_{KL}(P(t) \parallel Q(t)) = \sum P(t) \log_2 \left[\frac{P(t)}{Q(t)} \right] \quad (5.8)$$

Where $P(t)$ and $Q(t)$ are two probability distributions we are comparing, often it is common to use a base 2 log as this converts the entropy to base 2. By relative entropy we are talking about the useful information gained/lost by switching from $P(t)$ to $Q(t)$. In our case $Q(t)$ is simply the distribution given by Eq. (5.6) and $P(t)$ is an idealised distribution, one where the model is accurate with 100% certainty.

$$p_{best} = P(t) = \begin{cases} 1 & \text{when } \hat{\mathbf{n}}_\alpha = \hat{\mathbf{n}}_{best} \\ 0 & \text{when } \hat{\mathbf{n}}_\alpha \neq \hat{\mathbf{n}}_{best} \end{cases} \quad (5.9)$$

In reality the distribution from Eq. (5.6) will assign some non-zero probability to every reference orientation. Therefore the relative entropy for a single measurement is given as:

$$D_{KL}(p_{best} \parallel p(\hat{\mathbf{n}}_\alpha|y_k(\hat{\mathbf{s}}), t)) = \log_2 \left[\frac{1}{p(\hat{\mathbf{n}}_\alpha|y_k(\hat{\mathbf{s}}), t)} \right] \quad (5.10)$$

The relative entropy is a measure if how spread out our distribution is. With larger values of D_{KL} indicating that our prediction is spread out so the correct orientation is unsure about $\hat{\mathbf{n}}_{best}$. Whereas a low value of D_{KL} means that our model is more confident in $\hat{\mathbf{n}}_{best}$. The only draw back being that the relative entropy does nothing to indicate accuracy, only how closely our distribution matches our ideal result. This will be better exemplified later in 5.2.3.

5.2.2 Brownian Simulation

We use the Brownian OT package developed by Fung *et al* [93] to simulate the motion of an asymmetric dimer (Figure 5.3a) within an optical trap. We simulate the motion of a dimer trapped in a highly focused Gaussian beam by calculating the optical forces imparted by the laser, and the Brownian force due to the surrounding fluid. We simulated a polystyrene dimer ($n = 1.59$) in a suspension of water ($n_{med} = 1.33$). As discussed in chapter 4 dimers can be stably trapped in off-axis orientations. We simulate a dimer (of size ratio 2) that is trapped in this off-axis orientation by a $5mW$ laser, due to the meta-stability of the trap the dimer is only trapped for second before it escapes the trap. The dimer's position and orientation is shown below:

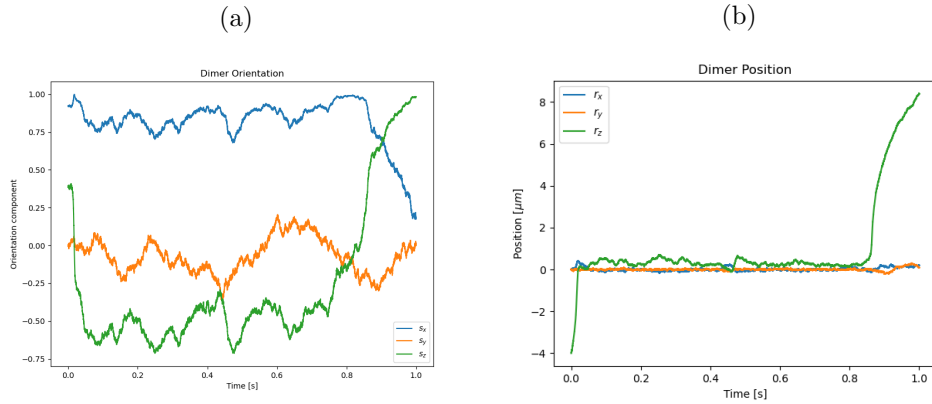


Figure 5.5: Simulation results of: (a) the dimer's orientation vector with time, (b) the dimer's [x,y,z] position with time.

At the same we use *mstm* to replicate the intensity of light incident on the surfaces of detectors placed around the focus of the optical trap. The exact number of detectors

was initially assumed to be arbitrary, in that it made no difference to our estimate whether we used 2 angles or 200. For practical purposes it seemed beneficial that we demonstrate our method works for a minimal number of detection angles, as geometric constraints come into play when trying to install a high number of detection fibres for any optical tweezer set up.

When all of the detectors lie in the same plane the expected signal can appear identical despite the dimer being in completely different orientations. It should be noted that these pairs are reflected in one or more axis which suggests that these are due to the arrangement of our detectors. More specifically, if the detectors are placed say in the x-y plane then only when the dimer is pointed nearly fully upright will the expected signal be entirely unique. This is not an issue with typical analytical static light scattering experiments because the signal being collected is averaged over a population of particles all in different orientations. Whereas in our set up we are concerned with the scattering of a single particle whose scattering is orientationally dependant.

To remedy this we raise the third detector out of the x-y plane; as such the expected signals from each reference orientation is unique, though with limited resolution. By adding a 4th detector we can differentiate signals more reliably, improving the neural networks performance. In line with our goal of making this method viable in a laboratory setting we decided not to increase the number of detectors further than 4.

5.2.3 Testing the Neural Network

We applied Eq. (5.6), taking the reference orientation with the highest probability as our estimate of the dimer's instantaneous orientation $\hat{\mathbf{n}}_{est}$. To visualise the model's performance we plotted the orientation components of our estimation $\hat{\mathbf{n}}_\alpha$ and the dimer's *actual* instantaneous orientation $\hat{\mathbf{s}}$ versus time. For comparison, we also plotted the orientation components of the closest reference orientation, $\hat{\mathbf{n}}_{best}$. Assuming a uniform prior of the reference orientations $p(\hat{\mathbf{n}}_\alpha)$ the neural network's predictions ($\hat{\mathbf{n}}_\alpha$ from Eq. (5.6)) are at times reasonable, but there are significant large and random jumps away from the correct result (Fig. 5.6).

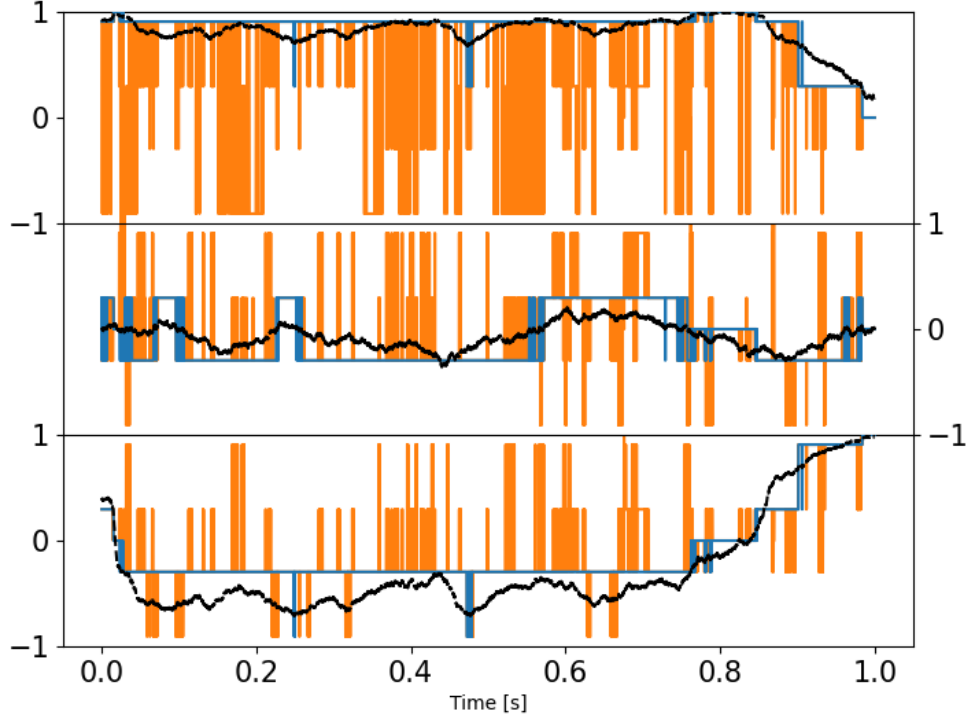


Figure 5.6: Model's estimation of dimer orientation over the simulation time, assuming uniform prior $p(\hat{\mathbf{n}}_\alpha)$, broken up into x, y, and z components for clarity. Blue line denotes the best result we can achieve (the reference orientation $\hat{\mathbf{n}}_{best}$ that is closest to the actual orientation), orange line denotes the result provided by eq 5.6: where the blue line is not visible, the model's prediction agrees with $\hat{\mathbf{n}}_{best}$. Dotted black line is the instantaneous orientation $\hat{\mathbf{s}}$.

One reason we observe such large jumps in the estimated orientation is simply because the neural network is assuming that the signals are unrelated from one another. We can observe this if we take the average relative entropy change across the entire trajectory:

$$\langle D_{KL} \rangle = \frac{1}{N} \sum_{i=1}^N \log_2 \left[\frac{1}{p(\hat{\mathbf{n}}_\alpha \parallel y_k(\hat{\mathbf{s}}), t_i)} \right] \quad (5.11)$$

Where we get an average entropy change of ≈ 0.604 , in base 2 this means that on average the model has narrowed down its options from 1 in 30 to 1 in 1.52. This is

not reflected though in fig. 5.6 which indicates that while the model is highly confident in its results it is not at all accurate. As demonstrated by fig 5.4 the orientation and signal spaces are uncorrelated with one another which results in the neural network to assign orientations incorrectly. Combining this fact with use of a uniform prior ($p(\hat{\mathbf{n}}_\alpha)$), there is no constraint on how much estimated orientation can change from time-step to time-step.

To improve the estimation we can therefore use knowledge of the physical limitations of the object in the trap and its dynamics. Imposing a more physically grounded prior, accounting in this case for the fact that the rotational motion of the dimer is limited by the rotational trap stiffness (κ_r). Here the prior of the reference orientations $p(\hat{\mathbf{n}}_\alpha)$ was redefined at each time step as a Boltzmann distribution of the physical distance between the previous estimate $\hat{\mathbf{n}}_{est}(t - \Delta t)$ and each reference orientation $\hat{\mathbf{n}}_\alpha$. Put simply, we are reweighing our estimation based on the size of rotation, with smaller movements being favoured over large movements:

$$p(\hat{\mathbf{n}}_\alpha) = \frac{e^{\hat{\mathbf{n}}_\alpha \cdot \hat{\mathbf{n}}_{est}(t - \Delta t)}}{\sum_{\alpha=1}^{n_{ref}} e^{\hat{\mathbf{n}}_\alpha \cdot \hat{\mathbf{n}}_{est}(t - \Delta t)}} \quad (5.12)$$

As shown in Figure 5.7 implementation of Eq (5.12) helps significantly reduce the large random excursions of estimated orientation away from the 'best' result. However at the same time result is still subpar.

Once again using Eq. (5.11) we now get a result of ≈ 0.204 or a 1 in 1.2 result. This is only a slight improvement in terms of confidence but has drastically reduced the variation in our models predictions. There are other improvements that can be made, which additionally also help with potential sources of error in our set up.

5.2.4 Accounting for sources of error in light scattering measurements

When it comes to analysing light scattering from any size particle, error analysis becomes a significant factor. Typically this can be accounted for by averaging over long periods of time to get an assessment of the steady state conditions of the target particle. However in our case where we wish to know the instantaneous orientation, we

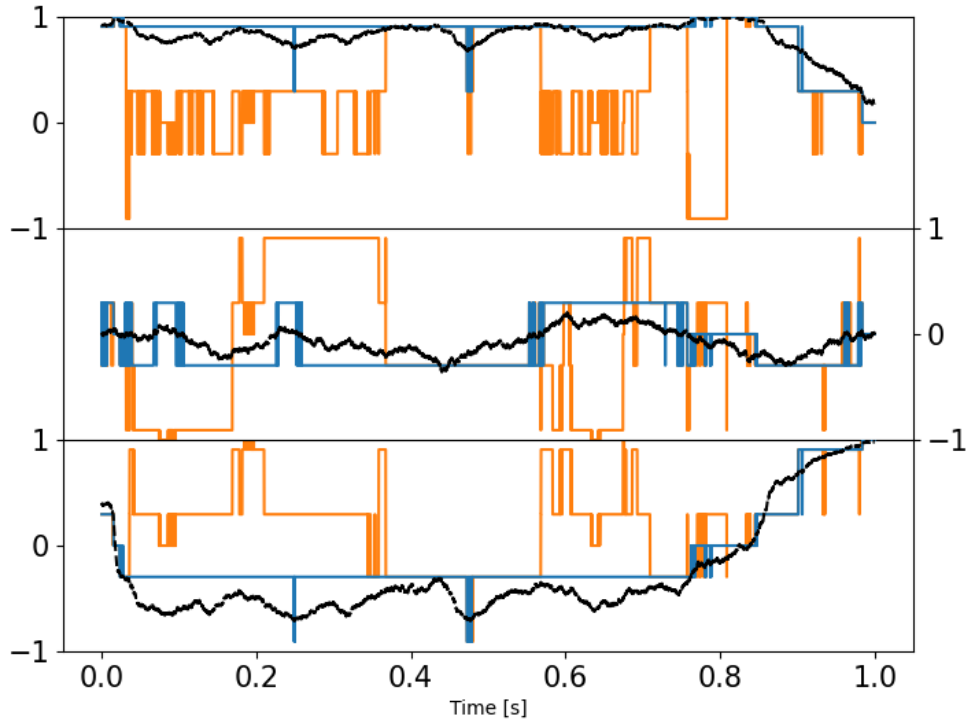


Figure 5.7: Estimation of dimer orientation with $p(\hat{\mathbf{n}}_\alpha)$ defined by Eq (5.12). Blue line denotes the best result we can achieve, orange line denotes the result provided by eq 5.6. Dotted black line is the instantaneous orientation $\hat{\mathbf{s}}$ (see Section ??).

instead have to rely on our understanding of how uncertainty can effect our model's performance. We identified two areas which are likely sources of error in our estimation: firstly, an incorrect modelling of the target particle, and secondly, signal noise arising from experimental factors. We highlight how we address these areas below.

Impact of incorrect dimer sizing One of the main limitations of our model is that we assume that the dimer being modelled in *mstm* is accurate to the dimer being trapped in the optical tweezer. Sizing molecules accurately is a significant challenge for single particle analysis so there is bound to be some uncertainty with the measurements. We ran our model 3 times with the neural net being trained on a dimer of size ratio 1 : 1.95, 1 : 2.00 and 1 : 2.05.

As can be seen from Fig 5.8 even the slightest change in size ratio makes a very

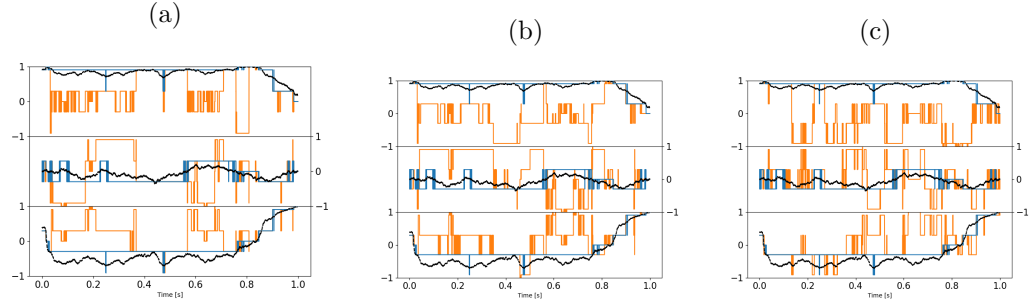


Figure 5.8: Model estimates of orientation when neural net has been trained on dimer of size ratio: (a) 1:2 [$\langle D_{KL} \rangle = 0.519$], (b) 1:2.05 [$\langle D_{KL} \rangle = 3.706$], (c) 1:1.95 [$\langle D_{KL} \rangle = 3.705$] ($n_{refs} = 30$)

significant difference to the performance of our model. This amounts to just over 100 nm in the dimer’s overall size, yet results in our model being correct from over 90 % of the time to now as low as 30 %. This highlights the importance of correctly sizing trapped entities before performing any in depth analysis of the scattering pattern, as even the slightest deviation can have a serious impact. We addressed this by increasing the number of available reference orientations from 30 to 126 (following the same procedure as given by [136] to evenly space out the coordinates) and increasing the weighting factor in Eq 5.12. While this didn’t have a significant improvement on the overall accuracy of the model, in the worst case having a slight increase from 30.5 % to 40.3 %, it did help to significantly reduce the magnitude between our model’s estimations and the dimer’s motion as seen below in Fig 5.9.

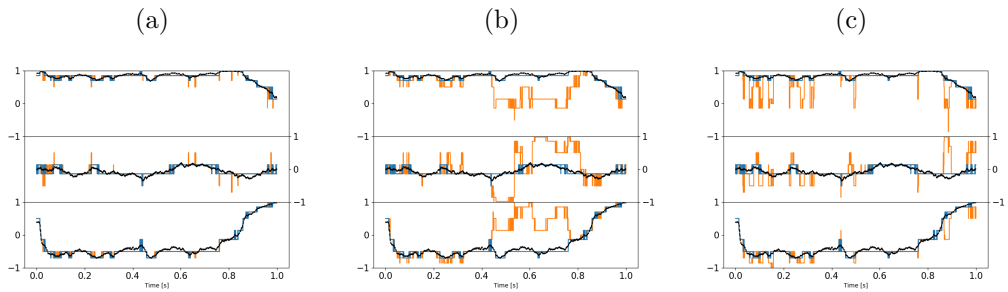


Figure 5.9: Model estimates of orientation when neural net has been trained on dimer of size ratio: (a) 1:2 [$\langle D_{KL} \rangle = 0.593$], (b) 1:2.05 [$\langle D_{KL} \rangle = 5.659$], (c) 1:1.95 [$\langle D_{KL} \rangle = 3.279$], ($n_{refs} = 126$)

Notably the increasing the number of reference orientations had a greater effect

when our neural network was trained on a 1:1.95 dimer than a 1:2.05 dimer. This suggests that overshooting our size estimate will be less detrimental to our estimation. Notably if the our sizing is off the neural network does not predict a smooth motion within the trap; instead predicting that the dimer is jumping back and forth between different orientations. This suggest that we can narrow down our estimate of the particle's size by assessing how the dimer is reorienting within the trap, as we should expect a smooth continuos prediction. Since we are working with a spherical dimer it also stands to reason that techniques such as image analysis could be used in part to address this, so long as the trapped entity is sufficiently illuminated.

Impact of measurement noise on model predictions So far a key assumption of the neural network implementation is that the detected scattering signal has no uncertainty associated with it. In reality of course scattering signals will always have some non-zero measurement noise. This can be attributed to a variety of factors, from a measurement bias in the detector, to the Brownian motion of the dimer itself. To explore the impact of measurement uncertainty on orientation estimation model performance we introduce a Gaussian noise to the measured signal:

$$I(\hat{\mathbf{s}}) = I(\hat{\mathbf{s}}) \pm \epsilon I(\hat{\mathbf{s}}) \quad (5.13)$$

where ϵ is the percentage error associated with the scattering signal. Figure 5.10 shows the performance of the model at a range of ϵ using in-plane detector angles 15° , 55° , 90° and out-of-plane detector at 75° , with β set to 1:

As can be seen from Figure 5.10, the inclusion of signal noise quickly leads to a decrease in the model's performance. So much so that beyond 15% the model is actually worse than just randomly guessing. This is due to an inherent feature of the inverse scattering problem: two distinct regions in orientation space can become heavily intertwined and thus no longer well separated when mapped to intensity space (even though the mapping remains continuous): so even small uncertainties in the scattering data can lead to large 'mistakes' in the choice of orientation by the neural network. (Indeed if this was not the case the inverse scattering problem would be quite simple.)

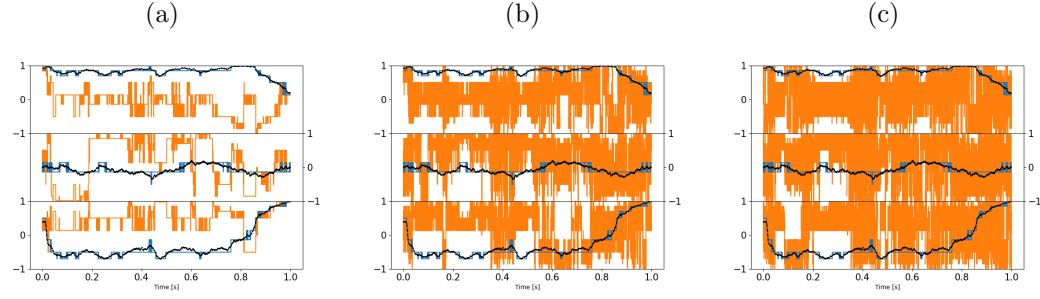


Figure 5.10: Model prediction for signal error of (a) 1% [$\langle D_{KL} \rangle = 0.962$], (b) 15% [$\langle D_{KL} \rangle = 13.654$], and (c) 25% [$\langle D_{KL} \rangle = 13.017$].

To reduce the effects of the signal noise we took the time average of the expected signal over 0.001s and then had our neural network estimate the orientation based on the average signal.

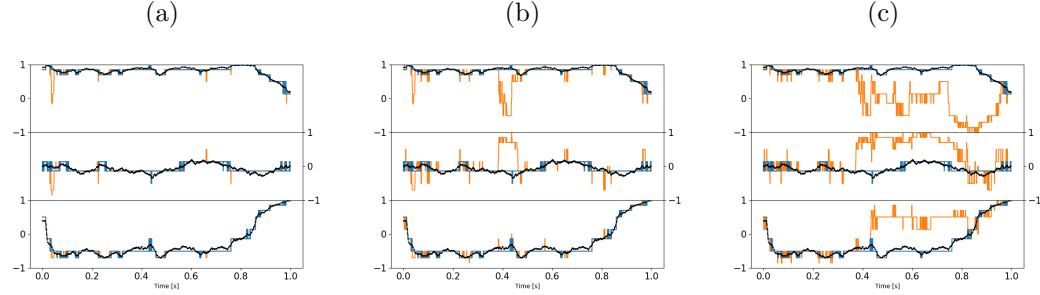


Figure 5.11: Model prediction for signal error of (a) 1% [$\langle D_{KL} \rangle = 1.447$], (b) 15% [$\langle D_{KL} \rangle = 4.670$], and (c) 25% [$\langle D_{KL} \rangle = 7.911$], time averaged over 1 ms

This resulted in a reduction in the overall signal noise and provided a higher degree of accuracy for our model. There appears to be no clear correlation between the length over which we time average and the performance of our model. Time averaging over every 0.05s resulted in a drastically worse performance; this is due to the fact that over longer time periods there is greater uncertainty regarding how the dimer's orientation has changed, thus tracking the instantaneous orientation becomes harder for the neural network. Fortunately, time averaging even over 1 ms seems to provide a satisfactory estimation of the dimer's angular dynamics within the optical trap.

From the above discussion it's clear that estimation of the dimer's orientation is a problem that can be endlessly tuned to fully maximise our end result. Here we sim-

plify the problem somewhat by employing a relatively small finite number of 'reference orientations' to map between scattering and dimer orientation: the precision of estimation could be improved by utilising a greater number of reference orientations, although there remains a balance between the realisable precision of orientation estimate and the noise level of the scattering measurement. Another avenue to further explore would be using the method to optimise the choice of detection angles, essentially to find the region in the mapping between measured scattering and orientation that others the best degree of confidence through optimal separation of scattering signals for distinct orientations. For sequences of data such as dynamic measurements, a further potential enhancement would be to consider more complex correlations based on prior expectations of the dynamics. Here already we improve the method using a non-uniform prior based on only the immediately previous measurement in time (see Section 2.1): considering a non-uniform grouping of reference orientations might result in a better estimation, if we have information regarding the dimer's preferred axis of rotation.

5.3 QPD Simulations

A QPD is simply a measure of the total electric field incident on a photo diode, in order to accurately simulate a QPD response careful consideration of how the Electromagnetic fields are defined is required.

5.3.1 Incident beam

The incident beam is simple enough to define given our set up parameters, for the sake of simplicity we assume that our beam is a Laguerre-Gaussian beam of mode [0.0, 0.0] (which is simply a pure Gaussian beam). *Ott* uses a point matching approach to approximate the beam shape coefficients of the incident field by fitting it to the far field estimate, the beam is of the form:

$$E_{inc}(kr) = \sum_n^{\infty} \sum_{m=-n}^n a_{mn} Rg M_{nm}(kr) + b_{nm} Rg N_{nm}(kr) \quad (5.14)$$

Where $RgM_{nm}(kr)$ & $RgN_{nm}(kr)$ are regular vector spherical wave functions, *ott* allows us to change the basis of the incident beam to suit our needs, because we are measuring in the far field we want to set our incident beam to be an outgoing spherical wave so that we can compute the intensity on the QPD. For spherical waves the field can either be expressed as an incoming/outgoing wave (with a singularity at the origin) or as a regular wave around the origin; for incoming/outgoing waves the wave functions use the first/second forms of the Hankel function respectfully. In order to compute the regular spherical wave at the origin we replace the Hankel function with the Bessel function which is simply the average of the first and second forms of the Hankel function, so at the origin we avoid a singularity of the EM field.

We can if we want further restrict the incident beam by applying setting the truncation angle to match our microscope object, this essentially applies a cut off point to the In order to compute the scattering from the target particle *ott* uses the t-matrix method, this is not essential for a simple sphere but is far more important for complex shaped particles such as our dimers. If the T-matrix is loaded in from *mstm* we need to convert the *mstm* t-matrix to a form more suitable for *ott*:

$$\begin{pmatrix} p_{nm} \\ q_{nm} \end{pmatrix} = T \begin{pmatrix} a_{nm} \\ b_{nm} \end{pmatrix} = \begin{pmatrix} aT_{nm}^{TM} & aT_{nm}^{TE} \\ bT_{nm}^{TM} & bT_{nm}^{TE} \end{pmatrix} \begin{pmatrix} a_{nm} \\ b_{nm} \end{pmatrix} \quad (5.15)$$

For *mstm* the T-matrix is packed as a column vector:

$$T_{MSTM} = \begin{bmatrix} aT_{n,-n}^{TE} & bT_{n,-n}^{TE} \\ aT_{n,-n+1}^{TE} & bT_{n,-n+1}^{TE} \\ \cdots & \cdots \\ aT_{n,n}^{TE} & bT_{n,n}^{TE} \\ \hline bT_{n,-n}^{TM} & bT_{n,-n}^{TM} \end{bmatrix} \quad (5.16)$$

Where as *ott* packs the T-matrix with sub matrices:

$$T_{Ott} = \begin{bmatrix} \begin{pmatrix} aT_{n,-n}^{TM} & aT_{n,-n}^{TE} \\ bT_{n,-n}^{TM} & bT_{n,-n}^{TE} \end{pmatrix} \\ \begin{pmatrix} aT_{n,-n+1}^{TM} & aT_{n,-n+1}^{TE} \\ bT_{n,-n+1}^{TM} & bT_{n,-n+1}^{TE} \end{pmatrix} \\ \dots \\ \begin{pmatrix} aT_{nm}^{TM} & aT_{nm}^{TE} \\ bT_{nm}^{TM} & bT_{nm}^{TE} \end{pmatrix} \end{bmatrix} \quad (5.17)$$

5.3.2 Scattered and Total Fields

With the T-matrix in hand we can compute the scattered beam by multiplying our beam shape coefficients with the T-matrix to get out the scattered field. Now in order to simulate a real QPD we need to account for the motion of our target particle within the trap, taking a typical trajectory file we read off each line in order to translate and rotate the beam. Translation is a rather simple process, simply involving us to shift the beam laterally, small deflections are generally unnoticeable for the incident beam but are much more noticeable in the scattered field (the below figure shows the result of shifting the incident beam $1\mu m$ to the right):

The QPD does not just pick up the scattered light however, it instead is receiving a combined signal from both the incident field and scattered field simultaneously, as mentioned by [Rohrbach](#) the total intensity can be computed by taking the magnitude of both the incident field *focused at the origin $[0, 0, 0]$ * and the scattered field originating from $[\delta x, \delta y, \delta z]$ (top left and bottom right plots in the above figure). This means we do not need to worry about any translation effects being 'double-counted' in the QPD's signal as we are only shifting the scattered field meaning the QPD signal is only picking up the interference due to the shifted scattered field. I conducted some unitary tests where I scanned the beam position laterally along the x-axis and measured the QPD's 'x-signal' for x, circular and y-polarized light which yielded the following QPD responses. The target particle was $1.57 \mu m$ and the scan range is set to $[-4, 4\mu m]$

Where S_x is given in blue, and S_y is given in orange, the plots make it clear that

Chapter 5. Detection and Characterisation of rotational spherical aggregate rotational dynamics

the polarisation of the beam have a minimal effect on the QPD signals if the particle is traversing in one direction, its clear that the displacement from the beam centre is far more important than the polarization of said beam. This is backed up when we look at Rohrbach's results, who studied a 150 nm sphere ($n = 1.57$) submerged in water with a focusing lens of numerical aperture 1.2, and beam power of 3 mW . The condensing lens' numerical aperture was not set to a particular value and was instead varied between 0.13-1.2, as a compromise we selected a condenser numerical aperture of 0.525, corresponding to a acceptance angle of 31.6° .

Where the points are Rohrbach's results and the solid line's are our QPD's own replication. The dashed horizontal lines on the left represent the maximum displacement in the lateral displacement which is given by the combined beam radius and particle radius (assuming a beam radius of $0.54\text{ }\mu\text{m}$); we can say that any displacements beyond this distance, while non-zero these displacements are unlikely to occur while a particle is trapped at the focus. Whereas the right most plot's dashed horizontal lines represents the Rayleigh range of the Gaussian beam, this represents the transition between plane wave and spherical wave regimes. Interestingly while our results close to Rohrbach's while close to the focus we see it begins to diverge beyond the first peak, this shouldn't be an issue for a typical optical tweezer calibration as we can assume that the maximum displacement will be within this linear regime.

Now the above plots only consider the QPD response to movements along the cartesian axis, however obviously for any Brownian motion the movements are a combination of displacements in each cartesian direction. We might assume naively that any displacement Δr will result in a linear combination of QPD responses; for low precision force measurements this assumption is adequate, however when high precision is required we find that this assumption is longer adequate due to something referred to as cross-talk. Cross talk arises when movement in one direction results in a QPD response change in the other orthogonal direction, there is no one reason for this effect, it could be a result of differing sensitivity in the photo diodes, it could be because the scattering is slightly asymmetric meaning the scattering falls outside the QPD, or it could be a result of mis-alignment in the set up. This can have unintended effects, for example

it may lead to the apparent rise of a curved trajectory rather than a straight path: Consider a particle moving purely along the x-axis, with 0 cross-talk the QPD response should perfectly match the above curve $S_x(x, 0, z_0)$, with S_y being flat in comparison; if however there is cross talk between the channels then S_y will have some significant non-zero value (or it may even grow with increasing displacement), implying that the particle is actually moving in both the x and y directions simultaneously. First we checked for this by measuring the QPD response for random positions within the XY plane:

Where S_x is plotted on top and S_y is plotted below, as shown by the above plot we see that they still possess similar shapes to the previous plots but now with additional noise terms, making it clear that for any trajectory there will be cross talk. This means that trying to get a one-to-one measurement of the particle's displacement is not possible by simply looking at the QPD response, to do that we can need to calibrate the trap.

[Berg and Flyvbjerg](#) have an excellent breakdown for accurately calibrating an optical tweezer, in addition they discuss how to minimise cross-talk effects. For two correlated power spectra, the cross correlation is given as:

$$P_x = |\hat{S}_x(f)|^2 \quad (5.18)$$

$$P_y = |\hat{S}_y(f)|^2 \quad (5.19)$$

$$\rightarrow P_{xy} = \text{Re}(\hat{S}_x \hat{S}_y^*) \quad (5.20)$$

Now if the two directions are correlated then $|P_{xy}|^2 / P_x P_y$ should be non-zero for all frequencies, in order to eliminate cross-talk effects we need to minimise the cross-correlation for all frequencies. They showed that it is possible to find a transformation of the time series $(x(t), y(t))$ to one that possesses the property that $P_{x'y'}(f) = 0$ for all frequencies. They found these transformed positions by minimising the sum cross-correlation:

$$\sum \frac{P_{x'y'}}{P_{x'}P_{y'}} = \sum \frac{(1+bc)P_{xy} + cP_x + bP_y}{(P_x + 2bP_{xy} + b^2P_y)(Py + 2cP_{xy} + c^2P_y)} \quad (5.21)$$

Where b and c are fitting parameters, by minimising this function one can adjust each spectra in order to eliminate cross talk effects and provide a more accurate calibration of the optical trap. Furthermore with the fitting completed, the time series can be then transformed in order to eliminate the cross talk effects:

$$x'(t) = S_x(t) + bS_y(t), \quad y'(t) = S_y(t) + cS_x(t) \quad (5.22)$$

Where x' and y' are now uncoupled coordinates that when Fourier transformed provide the uncorrelated power spectrum. With the fitting complete we can now adjust our time series in order to get a replication of the lateral trajectory.

5.4 Rotations and Asymmetric particles

Rotational motion is something that is not often necessarily considered when characterising Brownian motion, often because separating the contributions from rotational and translational motion is challenging. Depending on the rotational and translational trap stiffness the collected QPD signal will be aliased and typical calibration techniques cannot characterise the particle and trap interactions. This is often why most of the research into trapping asymmetric objects does not delve into power spectra analysis, as there is no real way of modelling the QPD response from an asymmetric object.

Now for isotropic scatterers any rotation is often not an issue when it comes to QPD analysis, even if a sphere rotates 180° the scattering should be identical (assuming its relative position is the same). Now *ott* deals with both translations and rotations by moving the beam itself and computing the scattering from by once again expanding the spherical wave functions, the problem that arises from this is that the portion of the spherical wave that is evaluated by the QPD will pick up said rotation and produce a non-zero signal even if the scatterer in question is isotropic. This means we need

Chapter 5. Detection and Characterisation of rotational spherical aggregate rotational dynamics

to counter rotate the total field prior to collecting the QPD signal, this captures the effects of an anisotropic scatterer but has no effect for an isotropic scatterer. As a test the QPD response from an isotropic sphere of $1.57 \mu m$ was collected at multiple angles, between 0 and 2π , then as a comparison a symmetrical and 1:2 dimer were also subjected to the same rotations and their QPD responses evaluated.

Where on the left we have an isotropic sphere, then a symmetrical dimer, and lastly a 1:2 dimer. The left most plot shows that simply using the inverted rotation matrix is sufficient to prevent rotation effects being double counted. For dimers however, rotating about a given axis gives us a clear change in the signal for even a slight rotation about any axis.

5.5 Power Spectra of single sphere vs spherical aggregates

In order to verify that the QPD is outputting correct signals we first compared the module to the only other known instance of simulating a QPD response, that being the work of [Rorrbach](#). In their paper they looked at the signal response produced by a single sphere ($r = 150 nm$, $n = 1.57$) being scanned along the three Cartesian axis in the proximity of a $1064 nm$ NIR beam with a numerical aperture of 1.2. As shown by fig 2.7 the two responses are remarkably accurate close to the origin; with only slight deviations as you move past the harmonic region, the difference can be explained due to how the two evaluate the total fields. Where in our case the incident and scattered fields are reduced to 0 at the origin, whereas Rohrbach's work evaluates the fields as being non-zero at all points, as you move beyond the origin this discrepancy grows.

Since we are only interested in the dynamics of spherical aggregates upon reaching equilibrium we do not need to be concerned about the deviation from Rohrbach's results so long as the particle's displacement does not exceed the linear region at the origin. The axial response curve is slightly more involved, requiring that the condenser lens numerical aperture is adjusted until a harmonic response curve is achieved [101].

In order to verify that the QPD can accurately capture the dynamics of the target particle we first simulated a single sphere ($a = 1\mu m$, $n = 1.59$) in the focus of a

1064 nm laser. Using *ott* the trap stiffness is computed by applying a linear fit to the force-displacement curve along the x and y axis'; for a linearly polarised trap the gradient force is greater in the polarisation direction than transverse case. We see this reflected in the simulated QPD, the fitted Lorentzian curves have different corner frequencies indicating that the beam's polarisation is influencing the dynamics of the trap.

Next we consider a dimer composed of two sphere's similar to the previous sphere, we again apply the QPD module to reproduce the power spectrum. Previous experimental work found that a pair of trapped beads would half the corner frequency from the reported power spectra. However, in our own simulations we see instead an increase in the expected trapping force from our QPD method, with the maximum trap stiffness expected for a dimer of size ratio 5. Compared to *ott* in which the maximum trapping strength is expected at a size ratio of 2. This can be somewhat explained by the fact that as the second sphere shrinks the centre of diffusion approaches the centre of the larger sphere and thus the dimer's orientational behaviour is similar to a single sphere, only subject to slight Brownian motion. Therefore one should expect that for aggregates containing multiple sized particles (e.g. cellular samples) typical characterisation techniques may over estimate the strength of the trap.

5.6 Conclusion

We have developed a method for measuring the dynamics of an optically-trapped colloidal objects based purely on measurements of the object's light scattering at a small number of detection angles. We demonstrate the method using the orientation of an asymmetric dimer as the dynamic variable and object of interest respectively, but in principle the model can be applied to any characteristic that impacts the light scattering pattern produced by a trapped entity such as size and shape. The MSTM package is a flexible tool for calculating the light scattering of complex objects using a representation of the object as a set of micro-particles, enabling training of a neural network to enable categorisation of the mapping between scattering and trapped object characteristics. By taking account of the physically realistic behaviour of the trapped

Chapter 5. Detection and Characterisation of rotational spherical aggregate rotational dynamics

object and the characteristics of the trap (which impact the dynamics of the object), the Bayesian inference method can be used to provide a reliable estimation of object characteristics of interest, even in the presence of measurement noise. Fundamentally, the inverse scattering problem is difficult to solve, since the mapping between object characteristics and scattering can be highly complex. We determined the minimum number of detectors required for a reliable estimation in the presence of measurement noise; furthermore, we demonstrated that the arrangement of these detectors is critical for a reliable estimation of an objects orientation. However, Bayesian inference based on neural network estimation of the mapping provides a powerful method for practical applications, extending the use of optical trapping beyond measuring microscopic force response toward detailed structural and dynamic information about complex trapped entities.

Chapter 6

Closing Remarks

Appendix A

Appendix

A.1 Estimation of fluid shear rates via galvano mirror

An alternative approach to generating fluid shear is to use a galvano-mirror to rapidly move a trapped particle in a bulk fluid. While typically galvano and gimble mirrors are used to trap multiple particles simultaneously, a single micro sphere can be moved quickly through a fluid along a preset path. The only limitation on the particle's speed being the ratio of the trap stiffness to the drag force. For low Reynolds numbers we can assume that the fluid flow is inversely proportional to the distance from the particle surface (see Eq. (3.4))

For a simple circular path one can estimate the sphere's speed by the radius of its path R and the frequency of its orbit ω so that $U = R\omega$. For a more complex path, such as an elliptical orbit the curve needs to be parametrised. One can describe the position of a sphere on an elliptical path as such:

$$r(p) = [a\cos(2\pi p), b\sin(2\pi p), 0] \quad (\text{A.1})$$

Where a and b are the characteristic radii of an ellipse. If we say that p is some dimensionless parameter that describes the distance travelled along a trajectory (so $p = 0$ is the start of the circular orbit and $p = 1$ is just as we return to the start). Then we can rewrite p as $p = t\omega$ where ω is the period of orbit. Taking the partial derivative

Appendix A. Appendix

of the position gives us the sphere's velocity vector along that path.

$$v(t) = \frac{\delta r(t)}{\delta t} = [-2\pi a\omega \sin(2\pi t\omega), 2\pi b\omega \cos(2\pi t\omega), 0] \quad (\text{A.2})$$

In order to compute the particle's speed U we simply take the magnitude of our velocity. For low velocities the fluid flow at the sphere's surface can be computed based on its velocity.

$$u_r(r) = -|v(t)| \left(1 - \frac{3R}{2r} + \frac{R^3}{2r^3} \right) \quad (\text{A.3})$$

Where r is the radial distance to that point. Again taking the partial derivative we can get the shear rate for a particle moving through the fluid:

$$\dot{\gamma}(r) = \left| \frac{\delta u_r(r)}{\delta r} \right| = |v(t)| \left(\frac{3R}{r^2} - \frac{2R^3}{r^4} \right) \quad (\text{A.4})$$

Moving a silica bead along an circular path can generate significant fluid flow around a larger volume compared to comparable micro-rotors. Using (A.4) we estimated the shear rate that the surrounding fluid would experience at varying speeds. The maximum speed of $7000 \mu\text{ms}^{-1}$ equates to moving the silica bead around a circular path with a frequency of 100 Hz .

From figure A.1 it is clear that not only is a galvano mirror a better option for generating high shear rates but also over a larger volume. The only limitation to this method is the effective drag experienced by the trapped particle.

Appendix A. Appendix

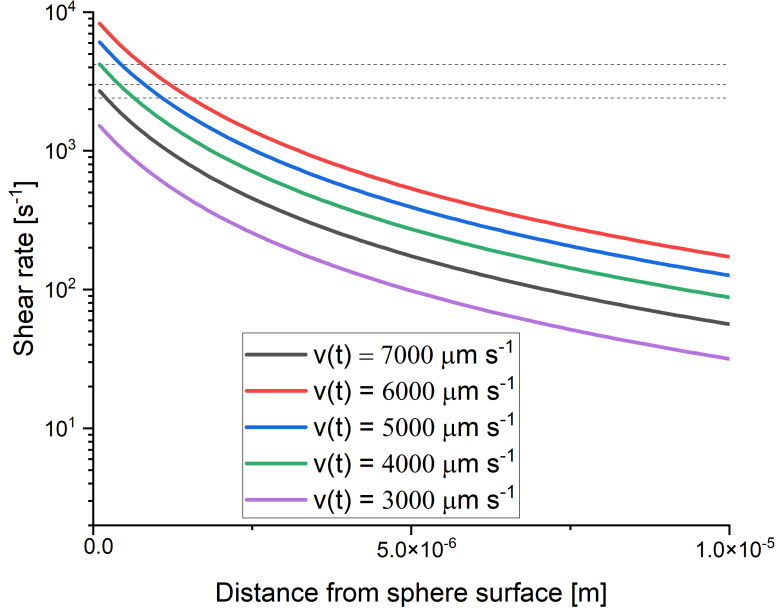


Figure A.1: Shear rate generated by a silica microsphere ($a = 1.57 \mu\text{m}$) in bulk water moving at different speeds. The shear rate is calculated using (A.4), with the assumption that the bead is moving in a circular path and so the speed is constant throughout its path.

A.2 Approximation of Area growth rate

Data collected from [26] provides face growth rates for glycine seed crystals in supersaturated solutions. The reported growth rates are given in terms of $\mu\text{m/sec}$, in order to compare to the laser induced nucleation events we need some method of converting to area units. In [26] the seed crystals are viewed from a top down perspective with the edges marked L_b and L_c . The authors calculated the face growth rates by:

$$G_{011} = \frac{1}{2} \sin(67.5^\circ) \frac{dL_c}{dt} \quad (\text{A.5})$$

$$G_{010} = \frac{1}{2} \sin(68.5^\circ) \frac{dL_b}{dt} \quad (\text{A.6})$$

The face growth rates are provided in the final paper, its easy enough to rearrange the two equations to get dL_c/dt and dL_b/dt . The area growth rate can be computed

Appendix A. Appendix

via the chain rule, where we overestimate the area of the glycine crystal to have a rectangular cross section of side lengths L_b and L_c . Numerically computing the area gives us an approximate total growth rate of around $0.02\mu m^2/min$. This is also an over estimation of the crystal growth rates as in [26] they only consider crystals between $30\mu m$ and $80\mu m$ and note that the growth rate of smaller crystals is even slower.

Overall this demonstrates clearly that the growth rate of a single crystal is accelerated by the presence of an optical trap, at least just after nucleation. The presence of an optical trap close to a larger seed crystal is shown to inhibit the growth of the crystal front, both with a stationary beam [111] and a moving beam (see sec. 3.5.4)

Bibliography

- [1] H. M. Schoen, C. S. Grove, and J. A. Palermo, “The early history of crystallization,” *Journal of Chemical Education*, vol. 33, no. 8, p. 373, Aug. 1956, ISSN: 1938-1328. DOI: [10.1021/ed033p373](https://doi.org/10.1021/ed033p373).
- [2] Z. Gao, S. Rohani, J. Gong, *et al.*, “Recent developments in the crystallization process: Toward the pharmaceutical industry,” *Engineering*, vol. 3, no. 3, pp. 343–353, Jun. 2017, ISSN: 2095-8099. DOI: [10.1016/j.eng.2017.03.022](https://doi.org/10.1016/j.eng.2017.03.022).
- [3] R. W. Hartel, “Crystallization in foods,” in *Handbook of Industrial Crystallization*. Elsevier, 2002, pp. 287–304, ISBN: 9780750670128. DOI: [10.1016/b978-075067012-8/50015-x](https://doi.org/10.1016/b978-075067012-8/50015-x).
- [4] A. S. Myerson and R. Ginde, “Crystals, crystal growth, and nucleation,” in *Handbook of Industrial Crystallization*. Elsevier, 2002, pp. 33–65, ISBN: 9780750670128. DOI: [10.1016/b978-075067012-8/50004-5](https://doi.org/10.1016/b978-075067012-8/50004-5).
- [5] H. Fu, X. Gao, X. Zhang, *et al.*, “Recent advances in nonclassical crystallization: Fundamentals, applications, and challenges,” *Crystal Growth & Design*, vol. 22, no. 2, pp. 1476–1499, Nov. 2021, ISSN: 1528-7505. DOI: [10.1021/acs.cgd.1c01084](https://doi.org/10.1021/acs.cgd.1c01084).
- [6] J. W. Mullin, *Crystallization*. 4th ed. Oxford: Elsevier Science Technology, 2001, 1611 pp., Description based on publisher supplied metadata and other sources., ISBN: 9780080530116.
- [7] G. D. Botsaris, “Secondary nucleation — a review,” in *Industrial Crystallization*. Springer US, 1976, pp. 3–22, ISBN: 9781461572589. DOI: [10.1007/978-1-4615-7258-9_1](https://doi.org/10.1007/978-1-4615-7258-9_1).

Bibliography

- [8] J. Anwar, S. Khan, and L. Lindfors, “Secondary crystal nucleation: Nuclei breeding factory uncovered,” *Angewandte Chemie International Edition*, vol. 54, no. 49, pp. 14 681–14 684, Mar. 2015, ISSN: 1521-3773. DOI: 10.1002/anie.201501216.
- [9] S. G. Agrawal and A. H. J. Paterson, “Secondary nucleation: Mechanisms and models,” *Chemical Engineering Communications*, vol. 202, no. 5, pp. 698–706, Jan. 2015, ISSN: 1563-5201. DOI: 10.1080/00986445.2014.969369.
- [10] J. Frenkel, “A general theory of heterophase fluctuations and pretransition phenomena,” *The Journal of Chemical Physics*, vol. 7, no. 7, pp. 538–547, Jul. 1939, ISSN: 1089-7690. DOI: 10.1063/1.1750484.
- [11] M. Volmer and Weber, “Keimbildung in ubersattigten gebilden,” *Zeitschrift fur Physikalische Chemie*, vol. 119U, no. 1, pp. 277–301, Jan. 1926, ISSN: 0942-9352. DOI: 10.1515/zpch-1926-11927.
- [12] S. Karthika, T. K. Radhakrishnan, and P. Kalaichelvi, “A review of classical and nonclassical nucleation theories,” *Crystal Growth & Design*, vol. 16, no. 11, pp. 6663–6681, Oct. 2016, ISSN: 1528-7505. DOI: 10.1021/acs.cgd.6b00794.
- [13] M. Gharibeh, Y. Kim, U. Dieregsweiler, *et al.*, “Homogeneous nucleation of n-propanol, n-butanol, and n-pentanol in a supersonic nozzle,” *The Journal of Chemical Physics*, vol. 122, no. 9, Mar. 2005, ISSN: 1089-7690. DOI: 10.1063/1.1858438.
- [14] P. G. Vekilov, “The two-step mechanism of nucleation of crystals in solution,” *Nanoscale*, vol. 2, no. 11, p. 2346, 2010, ISSN: 2040-3372. DOI: 10.1039/c0nr00628a.
- [15] W. T. Lee, E. K. H. Salje, and M. T. Dove, “Effect of surface relaxations on the equilibrium growth morphology of crystals: Platelet formation,” *Journal of Physics: Condensed Matter*, vol. 11, no. 38, pp. 7385–7410, Sep. 1999, ISSN: 1361-648X. DOI: 10.1088/0953-8984/11/38/316.
- [16] S.-T. Yau and P. G. Vekilov, “Direct observation of nucleus structure and nucleation pathways in apoferritin crystallization,” *Journal of the American Chemical Society*, vol. 132, no. 42, pp. 14 681–14 684, Oct. 2010, ISSN: 0002-7261. DOI: 10.1021/ja104820x.

Bibliography

- ical Society*, vol. 123, no. 6, pp. 1080–1089, Jan. 2001, ISSN: 1520-5126. DOI: 10.1021/ja003039c.
- [17] P. R. t. Wolde and D. Frenkel, “Enhancement of protein crystal nucleation by critical density fluctuations,” *Science*, vol. 277, no. 5334, pp. 1975–1978, Sep. 1997, ISSN: 1095-9203. DOI: 10.1126/science.277.5334.1975.
- [18] O. Gliko, N. Neumaier, W. Pan, *et al.*, “A metastable prerequisite for the growth of lumazine synthase crystals,” *Journal of the American Chemical Society*, vol. 127, no. 10, pp. 3433–3438, Feb. 2005, ISSN: 1520-5126. DOI: 10.1021/ja043218k.
- [19] V. J. Anderson and H. N. W. Lekkerkerker, “Insights into phase transition kinetics from colloid science,” *Nature*, vol. 416, no. 6883, pp. 811–815, Apr. 2002, ISSN: 1476-4687. DOI: 10.1038/416811a.
- [20] J. R. Savage and A. D. Dinsmore, “Experimental evidence for two-step nucleation in colloidal crystallization,” *Physical Review Letters*, vol. 102, no. 19, p. 198302, May 2009, ISSN: 1079-7114. DOI: 10.1103/physrevlett.102.198302.
- [21] K. G. Soga, J. R. Melrose, and R. C. Ball, “Metastable states and the kinetics of colloid phase separation,” *The Journal of Chemical Physics*, vol. 110, no. 4, pp. 2280–2288, Jan. 1999, ISSN: 1089-7690. DOI: 10.1063/1.477881.
- [22] W. Ostwald, “Studien über die bildung und umwandlung fester körper: 1. abhandlung: Übersättigung und überkaltung,” *Zeitschrift für Physikalische Chemie*, vol. 22U, no. 1, pp. 289–330, Feb. 1897, ISSN: 0942-9352. DOI: 10.1515/zpch-1897-2233.
- [23] P. Tan, N. Xu, and L. Xu, “Visualizing kinetic pathways of homogeneous nucleation in colloidal crystallization,” *Nature Physics*, vol. 10, no. 1, pp. 73–79, Dec. 2013, ISSN: 1745-2481. DOI: 10.1038/nphys2817.
- [24] Z. Liao and K. Wynne, “A metastable amorphous intermediate is responsible for laser-induced nucleation of glycine,” vol. 144, pp. 6727–6733, 2022, ISSN: 0002-7863. DOI: 10.1021/jacs.1c11154.

Bibliography

- [25] K. Srinivasan, “Crystal growth of alpha and gamma glycine polymorphs and their polymorphic phase transformations,” *Journal of Crystal Growth*, vol. 311, no. 1, pp. 156–162, Dec. 2008, ISSN: 0022-0248. DOI: [10.1016/j.jcrysgro.2008.10.084](https://doi.org/10.1016/j.jcrysgro.2008.10.084).
- [26] L. Li and N. Rodríguez-Hornedo, “Growth kinetics and mechanism of glycine crystals,” *Journal of Crystal Growth*, vol. 121, no. 1–2, pp. 33–38, Jun. 1992, ISSN: 0022-0248. DOI: [10.1016/0022-0248\(92\)90172-f](https://doi.org/10.1016/0022-0248(92)90172-f).
- [27] A. Ashkin, J. M. Dziedzic, J. E. Bjorkholm, *et al.*, *Observation of a single-beam gradient force optical trap for dielectric particles*. DOI: [10.1887/0750309016/b1142c30](https://doi.org/10.1887/0750309016/b1142c30).
- [28] A. Ashkin, “Applications of laser radiation pressure,” *Science*, vol. 210, no. 4474, pp. 1081–1088, Dec. 1980, ISSN: 1095-9203. DOI: [10.1126/science.210.4474.1081](https://doi.org/10.1126/science.210.4474.1081).
- [29] P.-W. Yi, W.-H. Chiu, T. Kudo, *et al.*, “Cooperative optical trapping of polystyrene microparticle and protein forming a submillimeter linear assembly of microparticle,” *The Journal of Physical Chemistry C*, vol. 125, no. 34, pp. 18 988–18 999, Aug. 2021, ISSN: 1932-7455. DOI: [10.1021/acs.jpcc.1c05796](https://doi.org/10.1021/acs.jpcc.1c05796).
- [30] J. Ahn, Z. Xu, J. Bang, *et al.*, “Optically levitated nanodumbbell torsion balance and ghz nanomechanical rotor,” *Physical Review Letters*, vol. 121, no. 3, p. 033 603, Jul. 2018, ISSN: 1079-7114. DOI: [10.1103/physrevlett.121.033603](https://doi.org/10.1103/physrevlett.121.033603).
- [31] F. Monteiro, S. Ghosh, E. C. van Assendelft, *et al.*, “Optical rotation of levitated spheres in high vacuum,” *Physical Review A*, vol. 97, no. 5, p. 051 802, May 2018, ISSN: 2469-9934. DOI: [10.1103/physreva.97.051802](https://doi.org/10.1103/physreva.97.051802).
- [32] B. A. Garetz, J. E. Aber, N. L. Goddard, *et al.*, “Nonphotochemical, polarization-dependent, laser-induced nucleation in supersaturated aqueous urea solutions,” *Physical Review Letters*, vol. 77, no. 16, pp. 3475–3476, Oct. 1996, ISSN: 1079-7114. DOI: [10.1103/physrevlett.77.3475](https://doi.org/10.1103/physrevlett.77.3475).

Bibliography

- [33] B. A. Garetz, J. Matic, and A. S. Myerson, “Polarization switching of crystal structure in the nonphotochemical light-induced nucleation of supersaturated aqueous glycine solutions,” *Physical Review Letters*, vol. 89, no. 17, p. 175501, Oct. 2002, ISSN: 1079-7114. DOI: 10.1103/physrevlett.89.175501.
- [34] X. Sun, B. A. Garetz, and A. S. Myerson, “Supersaturation and polarization dependence of polymorph control in the nonphotochemical laser-induced nucleation (nplin) of aqueous glycine solutions,” *Crystal Growth & Design*, vol. 6, no. 3, pp. 684–689, 2006, ISSN: 1528-7483. DOI: 10.1021/cg050460+.
- [35] R. Kacker, S. Dhingra, D. Irimia, *et al.*, “Multiparameter investigation of laser-induced nucleation of supersaturated aqueous kcl solutions,” *Crystal Growth & Design*, vol. 18, no. 1, pp. 312–317, Dec. 2017, ISSN: 1528-7505. DOI: 10.1021/acs.cgd.7b01277.
- [36] B. C. Knott, M. F. Doherty, and B. Peters, “A simulation test of the optical kerr mechanism for laser-induced nucleation,” *The Journal of Chemical Physics*, vol. 134, no. 15, Apr. 2011, ISSN: 1089-7690. DOI: 10.1063/1.3574010.
- [37] A. J. Alexander and P. J. Camp, “Single pulse, single crystal laser-induced nucleation of potassium chloride,” *Crystal Growth & Design*, vol. 9, no. 2, pp. 958–963, Dec. 2008, ISSN: 1528-7505. DOI: 10.1021/cg8007415.
- [38] V. Korede, N. Nagalingam, F. M. Penha, *et al.*, “A review of laser-induced crystallization from solution,” *Crystal Growth & Design*, vol. 23, no. 5, pp. 3873–3916, 2023. DOI: 10.1021/acs.cgd.2c01526. eprint: <https://doi.org/10.1021/acs.cgd.2c01526>. [Online]. Available: <https://doi.org/10.1021/acs.cgd.2c01526>.
- [39] M. R. Ward, A. M. Mackenzie, and A. J. Alexander, “Role of impurity nanoparticles in laser-induced nucleation of ammonium chloride,” *Crystal Growth & Design*, vol. 16, no. 12, pp. 6790–6796, Nov. 2016, ISSN: 1528-7505. DOI: 10.1021/acs.cgd.6b00882.
- [40] H. Y. Yoshikawa, Y. Hosokawa, and H. Masuhara, “Explosive crystallization of urea triggered by focused femtosecond laser irradiation,” *Japanese Journal*

Bibliography

- of Applied Physics*, vol. 45, no. 1L, p. L23, Dec. 2005, ISSN: 1347-4065. DOI: 10.1143/jjap.45.123.
- [41] A. Soare, R. Dijkink, M. R. Pascual, *et al.*, “Crystal nucleation by laser-induced cavitation,” *Crystal Growth & Design*, vol. 11, no. 6, pp. 2311–2316, Apr. 2011, ISSN: 1528-7505. DOI: 10.1021/cg2000014.
- [42] E. R. Barber, N. L. H. Kinney, and A. J. Alexander, “Pulsed laser-induced nucleation of sodium chlorate at high energy densities,” *Crystal Growth & Design*, vol. 19, no. 12, pp. 7106–7111, Oct. 2019, ISSN: 1528-7505. DOI: 10.1021/acs.cgd.9b00951.
- [43] K. Ikeda, M. Maruyama, Y. Takahashi, *et al.*, “Selective crystallization of the metastable phase of indomethacin at the interface of liquid/air bubble induced by femtosecond laser irradiation,” *Applied Physics Express*, vol. 8, no. 4, p. 045 501, Mar. 2015, ISSN: 1882-0786. DOI: 10.7567/apex.8.045501.
- [44] X.-L. Wang, J. Chen, Y. Li, *et al.*, “Optical orbital angular momentum from the curl of polarization,” *Physical Review Letters*, vol. 105, no. 25, p. 253 602, Dec. 2010, ISSN: 1079-7114. DOI: 10.1103/physrevlett.105.253602.
- [45] Y. Tsuboi, T. Shoji, and N. Kitamura, “Optical trapping of amino acids in aqueous solutions,” *The Journal of Physical Chemistry C*, vol. 114, no. 12, pp. 5589–5593, Dec. 2009, ISSN: 1932-7455. DOI: 10.1021/jp9072334.
- [46] K.-i. Yuyama, T. Sugiyama, and H. Masuhara, “Millimeter-scale dense liquid droplet formation and crystallization in glycine solution induced by photon pressure,” *The Journal of Physical Chemistry Letters*, vol. 1, no. 9, pp. 1321–1325, Apr. 2010, ISSN: 1948-7185. DOI: 10.1021/jz100266t.
- [47] K.-i. Yuyama, T. Rungsimanon, T. Sugiyama, *et al.*, “Formation, dissolution, and transfer dynamics of a millimeter-scale thin liquid droplet in glycine solution by laser trapping,” *The Journal of Physical Chemistry C*, vol. 116, no. 12, pp. 6809–6816, Mar. 2012, ISSN: 1932-7455. DOI: 10.1021/jp210576k.

Bibliography

- [48] O. Y. Gowayed, T. Moosa, A. M. Moratos, *et al.*, “Dynamic light scattering study of a laser-induced phase-separated droplet of aqueous glycine,” vol. 125, pp. 7828–7839, 2021, ISSN: 1520-6106. DOI: 10.1021/acs.jpcb.1c02620.
- [49] M. B. Sweatman, N. D. Afify, C. A. Ferreiro-Rangel, *et al.*, “Molecular dynamics investigation of clustering in aqueous glycine solutions,” *The Journal of Physical Chemistry B*, vol. 126, no. 25, pp. 4711–4722, Jun. 2022, ISSN: 1520-5207. DOI: 10.1021/acs.jpcb.2c01975.
- [50] A. I. Bishop, T. A. Nieminen, N. R. Heckenberg, *et al.*, “Optical microrheology using rotating laser-trapped particles,” *Physical Review Letters*, vol. 92, no. 19, p. 198 104, May 2004, ISSN: 1079-7114. DOI: 10.1103/physrevlett.92.198104.
- [51] R. M. Robertson-Anderson, “Optical tweezers microrheology: From the basics to advanced techniques and applications,” *ACS Macro Letters*, vol. 7, no. 8, pp. 968–975, Aug. 2018, ISSN: 2161-1653. DOI: 10.1021/acsmacrolett.8b00498.
- [52] R. A. Beth, “Mechanical detection and measurement of the angular momentum of light,” *Physical Review*, vol. 50, pp. 115–125, 1936. [Online]. Available: <https://api.semanticscholar.org/CorpusID:126010764>.
- [53] G. D. Bruce, P. Rodríguez-Sevilla, and K. Dholakia, “Initiating revolutions for optical manipulation: The origins and applications of rotational dynamics of trapped particles,” *Advances in Physics: X*, vol. 6, no. 1, Dec. 2020, ISSN: 2374-6149. DOI: 10.1080/23746149.2020.1838322.
- [54] V. Svák, O. Brzobohatý, M. Šiler, *et al.*, “Transverse spin forces and non-equilibrium particle dynamics in a circularly polarized vacuum optical trap,” *Nature Communications*, vol. 9, no. 1, Dec. 2018, ISSN: 2041-1723. DOI: 10.1038/s41467-018-07866-8.
- [55] J. Courtial and M. J. Padgett, “Limit to the orbital angular momentum per unit energy in a light beam that can be focussed onto a small particle,” *Optics Communications*, vol. 173, no. 1-6, pp. 269–274, 2000, ISSN: 0030-4018. DOI: 10.1016/s0030-4018(99)00619-7.

Bibliography

- [56] K. Y. Bliokh, A. Y. Bekshaev, and F. Nori, “Extraordinary momentum and spin in evanescent waves,” *Nature Communications*, vol. 5, no. 1, Mar. 2014, ISSN: 2041-1723. DOI: [10.1038/ncomms4300](https://doi.org/10.1038/ncomms4300).
- [57] S. J. Parkin, R. Vogel, M. Persson, *et al.*, “Highly birefringent vaterite microspheres: Production, characterization and applications for optical micromanipulation,” *Optics Express*, vol. 17, no. 24, p. 21944, Nov. 2009, ISSN: 1094-4087. DOI: [10.1364/oe.17.021944](https://doi.org/10.1364/oe.17.021944).
- [58] Y. Arita, J. M. Richards, M. Mazilu, *et al.*, “Rotational dynamics and heating of trapped nanovaterite particles,” *ACS Nano*, vol. 10, no. 12, pp. 11505–11510, Dec. 2016, ISSN: 1936-086X. DOI: [10.1021/acsnano.6b07290](https://doi.org/10.1021/acsnano.6b07290).
- [59] J. Millen, T. Deesawan, P. Barker, *et al.*, “Nanoscale temperature measurements using non-equilibrium brownian dynamics of a levitated nanosphere,” *Nature Nanotechnology*, vol. 9, no. 6, pp. 425–429, May 2014, ISSN: 1748-3395. DOI: [10.1038/nnano.2014.82](https://doi.org/10.1038/nnano.2014.82).
- [60] P. Rodríguez-Sevilla, Y. Arita, X. Liu, *et al.*, “The temperature of an optically trapped, rotating microparticle,” *ACS Photonics*, vol. 5, no. 9, pp. 3772–3778, Aug. 2018, ISSN: 2330-4022. DOI: [10.1021/acspophotonics.8b00822](https://doi.org/10.1021/acspophotonics.8b00822).
- [61] R. Reimann, M. Doderer, E. Hebestreit, *et al.*, “Ghz rotation of an optically trapped nanoparticle in vacuum,” *Physical Review Letters*, vol. 121, no. 3, p. 033602, Jul. 2018, ISSN: 1079-7114. DOI: [10.1103/physrevlett.121.033602](https://doi.org/10.1103/physrevlett.121.033602).
- [62] Q. Zhu, N. Li, H. Su, *et al.*, “Dynamic analysis and simulation of an optically levitated rotating ellipsoid rotor in liquid medium,” *Photonic Sensors*, vol. 12, no. 2, pp. 105–116, Sep. 2021, ISSN: 2190-7439. DOI: [10.1007/s13320-021-0639-0](https://doi.org/10.1007/s13320-021-0639-0).
- [63] B. M. Mihiretie, P. Snabre, J. ... Loudet, *et al.*, “Optically driven oscillations of ellipsoidal particles. part i: Experimental observations,” *The European Physical Journal E*, vol. 37, no. 12, Dec. 2014, ISSN: 1292-895X. DOI: [10.1140/epje/i2014-14124-0](https://doi.org/10.1140/epje/i2014-14124-0).

Bibliography

- [64] E. Higurashi, H. Ukita, H. Tanaka, *et al.*, “Optically induced rotation of anisotropic micro-objects fabricated by surface micromachining,” *Applied Physics Letters*, vol. 64, no. 17, pp. 2209–2210, Apr. 1994, ISSN: 1077-3118. DOI: 10.1063/1.111675.
- [65] J. Bang, T. Seberson, P. Ju, *et al.*, “Five-dimensional cooling and nonlinear dynamics of an optically levitated nanodumbbell,” *Physical Review Research*, vol. 2, no. 4, p. 043054, Oct. 2020, ISSN: 2643-1564. DOI: 10.1103/physrevresearch.2.043054.
- [66] F. Mura and A. Zacccone, “Effects of shear flow on phase nucleation and crystallization,” *Physical Review E*, vol. 93, no. 4, p. 042803, Apr. 2016, ISSN: 2470-0053. DOI: 10.1103/physreve.93.042803.
- [67] R. Debuyschère, B. Rimez, A. Zacccone, *et al.*, “Experimental and theoretical investigation of nonclassical shear-induced nucleation mechanism for small molecule,” *Crystal Growth & Design*, vol. 23, no. 7, pp. 4979–4989, Jun. 2023, ISSN: 1528-7505. DOI: 10.1021/acs.cgd.3c00232.
- [68] D. Richard and T. Speck, “The role of shear in crystallization kinetics: From suppression to enhancement,” *Scientific Reports*, vol. 5, no. 1, Sep. 2015, ISSN: 2045-2322. DOI: 10.1038/srep14610.
- [69] A. Goswami, I. S. Dalal, and J. K. Singh, “Seeding method for ice nucleation under shear,” *The Journal of Chemical Physics*, vol. 153, no. 9, Sep. 2020, ISSN: 1089-7690. DOI: 10.1063/5.0021206.
- [70] A. Mersmann, *Crystallization Technology Handbook*. CRC Press, May 2001, ISBN: 9780203908280. DOI: 10.1201/9780203908280.
- [71] J. D. Jackson, *Classical Electrodynamics*. New York: Wiley, 1975.
- [72] T. A. Yasuhiro Harada, “Radiation forces on a dielectric sphere in the rayleigh scattering regime,” *Optics Communications*, vol. 124, no. 5-6, pp. 529–541, Mar. 1996. DOI: [https://doi.org/10.1016/0030-4018\(95\)00753-9](https://doi.org/10.1016/0030-4018(95)00753-9). [Online]. Available: <https://www.sciencedirect.com/science/article/pii/0030401895007539>.

Bibliography

- [73] M. Capitanio, G. Romano, R. Ballerini, *et al.*, “Calibration of optical tweezers with differential interference contrast signals,” *Review of Scientific Instruments*, vol. 73, no. 4, pp. 1687–1696, Apr. 2002, ISSN: 1089-7623. DOI: 10.1063/1.1460929.
- [74] A. A. Ranha Neves and C. L. Cesar, “Analytical calculation of optical forces on spherical particles in optical tweezers: Tutorial,” *Journal of the Optical Society of America B*, vol. 36, no. 6, p. 1525, Mar. 2019, ISSN: 1520-8540. DOI: 10.1364/josab.36.001525.
- [75] Ø. Farsund and B. U. Felderhof, “Force, torque, and absorbed energy for a body of arbitrary shape and constitution in an electromagnetic radiation field,” *Physica A*, vol. 227, no. 1–2, pp. 108–130, May 1996, ISSN: 0378-4371. DOI: 10.1016/0378-4371(96)00009-x.
- [76] J. H. Crichton and P. L. Marston, “The measurable distinction between the spin and orbital angular momenta of electromagnetic radiation,” 2000. [Online]. Available: <https://api.semanticscholar.org/CorpusID:16957430>.
- [77] J. P. Gordon, “Radiation forces and momenta in dielectric media,” *Physical Review A*, vol. 8, no. 1, pp. 14–21, Jul. 1973, ISSN: 0556-2791. DOI: 10.1103/physreva.8.14.
- [78] W. Li, H. Hu, H. Su, *et al.*, “Numerical analysis on the optical force calculation in the rayleigh scattering regime,” *Optical Review*, vol. 28, no. 1, pp. 1–7, Jan. 2021, ISSN: 1349-9432. DOI: 10.1007/s10043-020-00631-7.
- [79] P. C. Waterman, “New formulation of acoustic scattering,” *The Journal of the Acoustical Society of America*, vol. 45, no. 6, pp. 1417–1429, Jun. 1969, ISSN: 1520-8524. DOI: 10.1121/1.1911619.
- [80] T. Wriedt and U. Comberg, “Comparison of computational scattering methods,” *Journal of Quantitative Spectroscopy and Radiative Transfer*, vol. 60, no. 3, pp. 411–423, Sep. 1998, ISSN: 0022-4073. DOI: 10.1016/s0022-4073(98)00016-8.

Bibliography

- [81] D. W. Mackowski and M. I. Mishchenko, “A multiple sphere t-matrix fortran code for use on parallel computer clusters,” vol. 112, pp. 2182–2192, 2011, ISSN: 0022-4073. DOI: [10.1016/j.jqsrt.2011.02.019](https://doi.org/10.1016/j.jqsrt.2011.02.019).
- [82] D. W. Mackowski and M. I. Mishchenko, “Calculation of the t matrix and the scattering matrix for ensembles of spheres,” *Journal of the Optical Society of America A*, vol. 13, no. 11, p. 2266, Nov. 1996, ISSN: 1520-8532. DOI: [10.1364/josaa.13.002266](https://doi.org/10.1364/josaa.13.002266).
- [83] Y.-l. Xu, “Electromagnetic scattering by an aggregate of spheres,” *Applied Optics*, vol. 34, no. 21, p. 4573, Jul. 1995, ISSN: 1539-4522. DOI: [10.1364/ao.34.004573](https://doi.org/10.1364/ao.34.004573).
- [84] E. M. Purcell and C. R. Pennypacker, “Scattering and absorption of light by nonspherical dielectric grains,” *The Astrophysical Journal*, vol. 186, p. 705, Dec. 1973, ISSN: 1538-4357. DOI: [10.1086/152538](https://doi.org/10.1086/152538).
- [85] G. H. Goedecke and S. G. O’Brien, “Scattering by irregular inhomogeneous particles via the digitized green’s function algorithm,” *Applied Optics*, vol. 27, no. 12, p. 2431, Jun. 1988, ISSN: 1539-4522. DOI: [10.1364/ao.27.002431](https://doi.org/10.1364/ao.27.002431).
- [86] D. T. Gillespie and E. Seitaridou, “The fickian theory of diffusion,” in *Simple Brownian Diffusion*. Oxford University Press, Oct. 2012, pp. 1–17. DOI: [10.1093/acprof:oso/9780199664504.003.0001](https://doi.org/10.1093/acprof:oso/9780199664504.003.0001).
- [87] D. T. Gillespie and E. Seitaridou, “Einstein’s theory of diffusion,” in *Simple Brownian Diffusion*. Oxford University Press, Oct. 2012, pp. 38–53. DOI: [10.1093/acprof:oso/9780199664504.003.0003](https://doi.org/10.1093/acprof:oso/9780199664504.003.0003).
- [88] D. T. Gillespie and E. Seitaridou, “Implications and limitations of the einstein theory of diffusion,” in *Simple Brownian Diffusion*. Oxford University Press, Oct. 2012, pp. 57–73. DOI: [10.1093/acprof:oso/9780199664504.003.0004](https://doi.org/10.1093/acprof:oso/9780199664504.003.0004).
- [89] D. T. Gillespie and E. Seitaridou, “Langevin’s theory of diffusion,” in *Simple Brownian Diffusion*. Oxford University Press, Oct. 2012, pp. 174–190. DOI: [10.1093/acprof:oso/9780199664504.003.0008](https://doi.org/10.1093/acprof:oso/9780199664504.003.0008).

Bibliography

- [90] G. Volpe and G. Volpe, “Simulation of a brownian particle in an optical trap,” *American Journal of Physics*, vol. 81, no. 3, pp. 224–230, Feb. 2013, ISSN: 1943-2909. DOI: 10.1119/1.4772632.
- [91] K. Berg-Sørensen and H. Flyvbjerg, “Power spectrum analysis for optical tweezers,” vol. 75, pp. 594–612, 2004, ISSN: 0034-6748. DOI: 10.1063/1.1645654.
- [92] S. B. Smith, Y. Cui, and C. Bustamante, “[7] optical-trap force transducer that operates by direct measurement of light momentum,” in *Biophotonics, Part B*. Elsevier, 2003, pp. 134–162. DOI: 10.1016/s0076-6879(03)61009-8.
- [93] W. Vigilante, O. Lopez, and J. Fung, “Brownian dynamics simulations of sphere clusters in optical tweezers,” *Optics Express*, vol. 28, no. 24, p. 36 131, Nov. 2020, ISSN: 1094-4087. DOI: 10.1364/oe.409078.
- [94] K. B. Oldham, J. C. Myland, and J. Spanier, “Dawson’s integral daw(x),” in *An Atlas of Functions*. Springer US, 2008, pp. 427–433, ISBN: 9780387488073. DOI: 10.1007/978-0-387-48807-3_43.
- [95] Yogesha, S. Bhattacharya, and S. Ananthamurthy, “Characterizing the rotation of non symmetric objects in an optical tweezer,” *Optics Communications*, vol. 285, no. 10–11, pp. 2530–2535, May 2012, ISSN: 0030-4018. DOI: 10.1016/j.optcom.2012.01.055.
- [96] M. Li and J. Arlt, “Trapping multiple particles in single optical tweezers,” vol. 281, pp. 135–140, 2008, ISSN: 0030-4018. DOI: 10.1016/j.optcom.2007.09.032.
- [97] Yogesha, S. Bhattacharya, and S. Ananthamurthy, “Precise characterization of micro rotors in optical tweezers,” *arXiv: Soft Condensed Matter*, 2011. [Online]. Available: <https://api.semanticscholar.org/CorpusID:118262469>.
- [98] T. A. Nieminen, V. L. Y. Loke, A. B. Stilgoe, *et al.*, “Optical tweezers computational toolbox,” vol. 9, S196–S203, 2007, ISSN: 1464-4258. DOI: 10.1088/1464-4258/9/8/s12.

Bibliography

- [99] A. Nir and A. Acrivos, “On the creeping motion of two arbitrary-sized touching spheres in a linear shear field,” *Journal of Fluid Mechanics*, vol. 59, no. 2, pp. 209–223, Jun. 1973, ISSN: 1469-7645. DOI: 10.1017/S0022112073001527. [Online]. Available: <http://dx.doi.org/10.1017/S0022112073001527>.
- [100] A. Rohrbach and E. H. K. Stelzer, “Three-dimensional position detection of optically trapped dielectric particles,” *Journal of Applied Physics*, vol. 91, no. 8, pp. 5474–5488, Apr. 2002, ISSN: 1089-7550. DOI: 10.1063/1.1459748.
- [101] L. Friedrich and A. Rohrbach, “Tuning the detection sensitivity: A model for axial backfocal plane interferometric tracking,” *Opt. Lett.*, vol. 37, no. 11, pp. 2109–2111, Jun. 2012. DOI: 10.1364/OL.37.002109. [Online]. Available: <https://opg.optica.org/ol/abstract.cfm?URI=ol-37-11-2109>.
- [102] K. Saito and Y. Kimura, “Optically driven liquid crystal droplet rotator,” *Scientific Reports*, vol. 12, no. 1, Oct. 2022, ISSN: 2045-2322. DOI: 10.1038/s41598-022-21146-y.
- [103] J. G. J. R. G.-S. A. M. I. P. Castillo, “Optical tweezers - fromn calibration to applications: A tutorial,” *Optics*, 2020. DOI: <https://doi.org/10.48550/arXiv.2004.05246>. [Online]. Available: <https://arxiv.org/abs/2004.05246>.
- [104] H.-I. Kim, I.-J. Joo, S.-H. Song, *et al.*, “Dependence of the optical trapping efficiency on the ratio of the beam radius-to-the aperture radius,” *Journal of the Korean Physical Society*, vol. 43, no. 3, p. 348, 2003.
- [105] S. N. S. Reihani, M. A. Charsooghi, H. R. Khalesifard, *et al.*, “Efficient in-depth trapping with an oil-immersion objective lens,” vol. 31, p. 766, 2006, ISSN: 0146-9592. DOI: 10.1364/ol.31.000766.
- [106] G. M. Gibson, J. Leach, S. Keen, *et al.*, “Measuring the accuracy of particle position and force in optical tweezers using high-speed video microscopy,” *Optics Express*, vol. 16, no. 19, p. 14561, Sep. 2008, ISSN: 1094-4087. DOI: 10.1364/oe.16.014561.

Bibliography

- [107] D. Konopacka-Lyskawa, “Synthesis methods and favorable conditions for spherical vaterite precipitation: A review,” *Crystals*, vol. 9, no. 4, p. 223, Apr. 2019, ISSN: 2073-4352. DOI: 10.3390/cryst9040223.
- [108] G. Volpe, O. M. Maragò, H. Rubinsztein-Dunlop, *et al.*, “Roadmap for optical tweezers,” *Journal of Physics: Photonics*, vol. 5, no. 2, p. 022501, Apr. 2023, ISSN: 2515-7647. DOI: 10.1088/2515-7647/acb57b.
- [109] G. Knöner, S. Parkin, N. R. Heckenberg, *et al.*, “Characterization of optically driven fluid stress fields with optical tweezers,” *Physical Review E*, vol. 72, no. 3, p. 031507, Sep. 2005, ISSN: 1550-2376. DOI: 10.1103/physreve.72.031507.
- [110] T. Sugiyama, T. Adachi, and H. Masuhara, “Crystal growth of glycine controlled by a focused cw near-infrared laser beam,” *Chemistry Letters*, vol. 38, no. 5, pp. 482–483, Apr. 2009, ISSN: 1348-0715. DOI: 10.1246/cl.2009.482.
- [111] J. Flannigan, “Optical tweezer and particle control of nucleation and growth at the microscale,” Ph.D. dissertation, University of Strathclyde, 2023. [Online]. Available: <https://pureportal.strath.ac.uk/en/studentTheses/optical-tweezer-and-particle-control-of-nucleation-and-growth-at->.
- [112] T. Rungsimanon, K.-i. Yuyama, T. Sugiyama, *et al.*, “Crystallization in unsaturated glycine/ $\text{d}_{\text{j}}\text{sub}_2\text{j}/\text{sub}_2\text{o}$ solution achieved by irradiating a focused continuous wave near infrared laser,” vol. 10, pp. 4686–4688, 2010, ISSN: 1528-7483. DOI: 10.1021/cg100830x.
- [113] T. Sugiyama and S.-F. Wang, “Manipulation of nucleation and polymorphism by laser irradiation,” *Journal of Photochemistry and Photobiology C: Photochemistry Reviews*, vol. 52, p. 100530, Sep. 2022, ISSN: 1389-5567. DOI: 10.1016/j.jphotochemrev.2022.100530.
- [114] P. Patyar, K. Kaur, and G. Singh, “Viscometric and spectroscopic studies on interactions of glycine with aqueous buffer solutions,” *Journal of Molecular Liquids*, vol. 307, p. 112921, Jun. 2020, ISSN: 0167-7322. DOI: 10.1016/j.molliq.2020.112921.

Bibliography

- [115] U. G. Būtaité, G. M. Gibson, Y.-L. D. Ho, *et al.*, “Indirect optical trapping using light driven micro-rotors for reconfigurable hydrodynamic manipulation,” *Nature Communications*, vol. 10, no. 1, Mar. 2019, ISSN: 2041-1723. DOI: 10.1038/s41467-019-08968-7.
- [116] W. H. Orttung, “Polarizability and apparent radius of glycine from refractive index data,” *The Journal of Physical Chemistry*, vol. 67, no. 5, pp. 1102–1105, 1963, ISSN: 0022-3654. DOI: 10.1021/j100799a040.
- [117] E. J. Peterman, F. Gittes, and C. F. Schmidt, “Laser-induced heating in optical traps,” *Biophysical Journal*, vol. 84, no. 2, pp. 1308–1316, Feb. 2003, ISSN: 0006-3495. DOI: 10.1016/s0006-3495(03)74946-7.
- [118] S. Xu, Y. Li, and L. Lou, “Axial optical trapping forces on two particles trapped simultaneously by optical tweezers,” vol. 44, p. 2667, 2005, ISSN: 0003-6935. DOI: 10.1364/ao.44.002667.
- [119] P. Praveen, Yogesha, S. S. Iyengar, *et al.*, “Two particle tracking and detection in a single gaussian beam optical trap,” vol. 55, p. 585, 2016, ISSN: 0003-6935. DOI: 10.1364/ao.55.000585.
- [120] J. Loudet, B. M. Mihiretie, and B. Pouliquen, “Optically driven oscillations of ellipsoidal particles. part ii: Ray-optics calculations,” vol. 37, 2014, ISSN: 1292-8941. DOI: 10.1140/epje/i2014-14125-y.
- [121] X. Sheng-Hua, L. Yin-Mei, L. Li-Ren, *et al.*, “Computer simulation of the collision frequency of two particles in optical tweezers,” vol. 14, pp. 382–385, 2005, ISSN: 1009-1963. DOI: 10.1088/1009-1963/14/2/028.
- [122] C. D, P. P, N. B V, *et al.*, “Laser polarization driven micromanipulation and reorientation dynamics of an asymmetric shaped microscopic biomaterial using optical tweezers,” *Journal of Optics*, vol. 24, no. 9, p. 094007, Aug. 2022, ISSN: 2040-8986. DOI: 10.1088/2040-8986/ac868c.
- [123] V. Shahabadi and E. Madadi, “Effective multiple optical trapping of sub-micrometer particles with petal beams,” *Journal of the Optical Society of America B*, vol. 37, no. 12, p. 3665, Nov. 2020, ISSN: 1520-8540. DOI: 10.1364/josab.402944.

Bibliography

- [124] A. A. Bui, A. B. Stilgoe, I. C. Lenton, *et al.*, “Theory and practice of simulation of optical tweezers,” *Journal of Quantitative Spectroscopy and Radiative Transfer*, vol. 195, pp. 66–75, Jul. 2017, ISSN: 0022-4073. DOI: [10.1016/j.jqsrt.2016.12.026](https://doi.org/10.1016/j.jqsrt.2016.12.026).
- [125] D. B. Ruffner and D. G. Grier, “Optical forces and torques in nonuniform beams of light,” *Physical Review Letters*, vol. 108, no. 17, p. 173602, Apr. 2012, ISSN: 1079-7114. DOI: [10.1103/physrevlett.108.173602](https://doi.org/10.1103/physrevlett.108.173602).
- [126] A. Yevick, D. J. Evans, and D. G. Grier, “Photokinetic analysis of the forces and torques exerted by optical tweezers carrying angular momentum,” *Philosophical Transactions of the Royal Society A: Mathematical, Physical and Engineering Sciences*, vol. 375, no. 2087, p. 20150432, Feb. 2017, ISSN: 1471-2962. DOI: [10.1098/rsta.2015.0432](https://doi.org/10.1098/rsta.2015.0432).
- [127] Y. Zhao, J. S. Edgar, G. D. M. Jeffries, *et al.*, “Spin-to-orbital angular momentum conversion in a strongly focused optical beam,” *Physical Review Letters*, vol. 99, no. 7, p. 073901, Aug. 2007, ISSN: 1079-7114. DOI: [10.1103/physrevlett.99.073901](https://doi.org/10.1103/physrevlett.99.073901).
- [128] Y. Zhao, D. Shapiro, D. McGloin, *et al.*, “Direct observation of the transfer of orbital angular momentum to metal particles from a focused circularly polarized gaussian beam,” *Optics Express*, vol. 17, no. 25, p. 23316, Dec. 2009, ISSN: 1094-4087. DOI: [10.1364/oe.17.023316](https://doi.org/10.1364/oe.17.023316).
- [129] B. Silverman, *Density Estimation for Statistical and Data Analysis*. Chapman and Hall, 1986.
- [130] M. Rashid, M. Toroš, A. Setter, *et al.*, “Precession motion in levitated optomechanics,” *Physical Review Letters*, vol. 121, no. 25, p. 253601, Dec. 2018, ISSN: 1079-7114. DOI: [10.1103/physrevlett.121.253601](https://doi.org/10.1103/physrevlett.121.253601).
- [131] T. M. Hoang, Y. Ma, J. Ahn, *et al.*, “Torsional optomechanics of a levitated nonspherical nanoparticle,” *Physical Review Letters*, vol. 117, no. 12, p. 123604, Sep. 2016, ISSN: 1079-7114. DOI: [10.1103/physrevlett.117.123604](https://doi.org/10.1103/physrevlett.117.123604).

Bibliography

- [132] S. Kuhn, A. Kosloff, B. A. Stickler, *et al.*, “Full rotational control of levitated silicon nanorods,” 2016. doi: 10.48550/ARXIV.1608.07315.
- [133] R. Bar-Ziv, A. Meller, T. Tlusty, *et al.*, “Localized dynamic light scattering: Probing single particle dynamics at the nanoscale,” *Physical Review Letters*, vol. 78, no. 1, pp. 154–157, Jan. 1997, issn: 1079-7114. doi: 10.1103/physrevlett.78.154.
- [134] A. Meller, R. Bar-Ziv, T. Tlusty, *et al.*, “Localized dynamic light scattering: A new approach to dynamic measurements in optical microscopy,” *Biophysical Journal*, vol. 74, no. 3, pp. 1541–1548, Mar. 1998, issn: 0006-3495. doi: 10.1016/s0006-3495(98)77866-x.
- [135] D. W. Michael I.Mishchenko Larry D.Travis, “T-matrix computations of light scattering by nonspherical particles: A review,” *Light scattering by Non-Spherical Particles*, vol. 55, pp. 535–575, 1996.
- [136] G. C. Reyuthor, “Numerical methods for radiative heattransfer,” Doctoral Thesis, Universitat Politècnica de Catalunya, 2006.
- [137] F. Pedregosa, G. Varoquaux, A. Gramfort, *et al.*, “Scikit-learn: Machine learning in Python,” *Journal of Machine Learning Research*, vol. 12, pp. 2825–2830, 2011.